

**Combining Ab Initio Computation with Experiments
for Designing/Understanding High Energy Density
Electrode Materials for Advanced Lithium Batteries**

by

Ying Shirley Meng

B. Sc (Mat. Eng.) with First Class Honors
Nanyang Technological University of Singapore, 2000

Submitted to the Singapore-MIT Alliance Office
in Partial Fulfillment of the Requirements for the Degree of

**DOCTOR OF PHILOSOPHY
IN ADVANCED MATERIALS FOR MICRO- & NANO- SYSTEMS
(AMM&NS)**

**AT
THE SINGAPORE-MIT ALLIANCE**

2005

Signature of author: _____
Ms. Ying Shirley Meng
AMM&NS Programme
September 30, 2004

Certified by: _____
Prof. Li Yi
SMA Fellow, NUS
Thesis Advisor

Certified by: _____
Prof. Gerbrand Ceder
SMA Fellow, MIT
Thesis Advisor

Accepted by: _____
Prof. Choi Wee Kiong
Programme Co-Chair
AMM&NS Programme

Accepted by: _____
Prof. Carl Thompson
Programme Co-Chair
AMM&NS Programme

Combining Ab Initio Computation with Experiments for Designing/Understanding High Energy Density Electrode Materials for Advanced Lithium Batteries

by

Ying Shirley Meng

Submitted to the Singapore-MIT Alliance Office in Partial Fulfillment of the Requirements for the Degree of Doctor of Philosophy in Advanced Materials for Micro- & Nano- Systems (AMM&NS)

ABSTRACT

We have performed an initial search on $\text{LiNi}_{1/3}\text{TM1}_{1/3}\text{TM2}_{1/3}\text{O}_2$ ($\text{TM1} = \text{Co}^{3+}, \text{Al}^{3+}, \text{Fe}^{3+}$ etc. and $\text{TM2} = \text{Ti}^{4+}, \text{Zr}^{4+}, \text{Mn}^{4+}$ etc.) with first principles computation. Fe substitution is found to be advantageous, since among the compounds investigated $\text{LiNi}_{1/3}\text{Fe}_{1/3}\text{Mn}_{1/3}\text{O}_2$ shows the lowest voltage at the last stage of charge. Excess Fe doping will result in non-layered phase according to mixed enthalpy calculation, thus the structural and electronic changes of $\text{LiNi}_{1/3}\text{Fe}_{1/6}\text{Co}_{1/6}\text{Mn}_{1/3}\text{O}_2$ with various lithium concentrations were investigated by first principles method. Motivated by the computation results, $\text{LiNi}_{1/3}\text{Fe}_z\text{Co}_{1/3-z}\text{Mn}_{1/3}\text{O}_2$ ($0 \leq z \leq 1/3$) cathode materials were synthesized by a sol-gel method. Excessive Fe substitution ($z > 2/9$) leads to evolution of non-layered impurity phase, which can be clearly observed by powder XRD and SEM experiments. XPS investigation for $\text{LiNi}_{1/3}\text{Fe}_z\text{Co}_{1/3-z}\text{Mn}_{1/3}\text{O}_2$ revealed that the oxidation state of Ni, Mn, Fe and Co are 2+, 4+, 3+ and 3+, respectively, which is consistent with the first principles prediction. First principles electronic structure computations indicated that Ni and Fe are simultaneously oxidized in this material and Co will only be oxidized at the very end of charge which is confirmed both by XPS and in-situ XAS. The inductive effect is found to be the main reason for $\text{Ni}^{2+}/\text{Ni}^{4+}$ redox voltage shift in $\text{Li}(\text{Ni}, \text{TM1}, \text{TM2})\text{O}_2$ layered compounds.

The second part of the thesis focuses on the three dimensional crystal structure of $\text{LiNi}_x\text{Li}_{1/3-2x/3}\text{Mn}_{2/3-x/3}\text{O}_2$ ($0 \leq x \leq 1/2$), which is an exciting new system of cathode materials for lithium ion batteries. Single crystal electron diffraction experiment indicates that Li, Ni and Mn ions are ordered in the transition metal layer and form two sublattices with significantly different occupation. It is demonstrated that for $\text{LiNi}_{1/2}\text{Mn}_{1/2}\text{O}_2$ ($x = 1/2$) such ordering would be extremely difficult to detect experimentally, if not impossible, with powder diffraction of X-ray and neutron. Detailed diffraction study reveals an *alb2c1* stacking sequence of these ordered planes in $\text{LiNi}_{1/2}\text{Mn}_{1/2}\text{O}_2$ ($x = 1/2$) and $\text{LiNi}_{1/3}\text{Li}_{1/9}\text{Mn}_{5/9}\text{O}_2$ ($x = 1/3$), though stacking disorder is observed in $\text{LiNi}_{1/2}\text{Mn}_{1/2}\text{O}_2$. For Li_2MnO_3 ($x = 0$) the exact stacking sequence of the sample is found to depend on the synthesis conditions.

Key words: lithium battery; energy storage; ab initio; first principles; DFT; lithium nickel manganese oxides; charge ordering; stacking faults; polytypes; diffraction.

Thesis Advisors: Prof. Gerbrand Ceder
Prof. Li Yi

Acknowledgements

I would foremost like to thank my thesis advisors Prof. Gerbrand Ceder and Prof. Li Yi. Their expert guidance and constant encouragements are essential to make this thesis possible. I am truly grateful for their generosity in sharing their knowledge and insights with me.

I am lucky to have worked in both Prof. Ceder's and Prof. Li Yi's groups, where I had many useful and stimulating discussions. The post doctoral researchers and graduate students in Prof. Ceder's group: Elena Arroyo, Dany Carlier, Dane Morgan, Anton Van der Ven, Eric Wu, John Reed, Chris Marianetti, Ashley Predith, Byungchan Han, Kisuk Kang, Chris Fischer, Tim Mueller Matteo Cococcioni, Thomas Maxisch and Byungwoo Kang have helped me and inspired me in many ways, making my two-year stay at MIT an enjoyable and memorable experience. I am also grateful to the post doctoral researchers and graduate students in Prof. Li Yi's group: Tan Hao, Irene Lee, Kong Hui Zi, Wang Dong, Zhang Yong and Wang Cui Yang, it has been a pleasure to work with them.

I express special thanks to Prof. Hwang Bing Joe, a visiting professor who I met and worked with in MIT. He is a great mentor and at the same time, a great friend. It was also a pleasure to work with Wu Yin Wei, former student of Prof. Hwang, for our collaboration work.

I am grateful to Prof. Yang Shao-Horn whose generosity in sharing her knowledge and life experience at a critical stage of my research is greatly appreciated. I am especially thankful for the time she spent with me discussing about diffraction and crystal structures.

The Singapore – MIT Alliance and the Department of Materials Science and Engineering at MIT are gratefully acknowledged for financial support.

Many thanks to my parents, Meng Jizu and Yu Yiping, for their unselfish support and love through out my life. Their trust in me has made me a strong and confident person.

Most of all, I thank my husband, Richard Wee whose understanding, patience, humor and love are crucial to make this all possible.

Contents

List of Figures11
List of Tables18

Part I Combining Ab Initio Computation with Experiments for Designing New High Energy Density Electrode Materials: $\text{Li}[\text{Ni}_{1/3}\text{TM}_{1/3}\text{TM}'_{1/3}]\text{O}_2$ 20

Chapter 1 Lithium Ion Batteries & the Electrode Materials21
1.1 Lithium Ion Batteries21
1.2 Developments in Lithium Ion Battery Research23
1.3 Materials for the Positive Electrode25
1.3.1 Intercalation Compounds25
1.3.2 LiCoO_2 vs. LiNiO_226
1.3.3 LiMnO_228
1.3.3 Multi-Cation Systems29
1.4 Motivation & Objectives31
References33

Chapter 2 First Principles Computation36
2.1 Quantum Mechanics and First Principles Energies36
2.2 Density Functional Theory38
2.3 LDA and GGA39
2.4 VASP40
References41

Chapter 3	Pre-screening of Candidate Electrode Materials by First Principles Methods42
3.1	Computation Details42
3.2	Formation Energies43
3.3	Voltages45
3.4	Material of the Choice48
3.4.1	Intercalation Voltage50
3.4.2	Electronic Change during Charge-Discharge51
3.4.3	Lattice Parameters and Bond Lengths55
3-5	Conclusions61
	References62
Chapter 4	Synthesis, Characterization & Electrochemical Testing of Fe/Co Substituted Lithium Nickel Manganese Oxides64
4.1	Guided Synthesis64
4.2	Characterization of As-Synthesized Materials66
4.2.1	Powder X-ray Diffraction66
4.2.2	Scanning Electron Microscopy69
4.2.3	Rietveld Refinement of Powder XRD Data72
4.2.4	X-ray Photoelectron Spectroscopy73
4.2.5	⁵⁷ Fe Mössbauer Spectroscopy76
4.3	Electrochemical Properties81
4.4	Characterization of Partially Charged Materials87
4.4.1	XPS and Change in Electronic Structures87

4.4.2	Ex-situ XRD and Lattice Parameter88
4.4.3	XAS and TM-O Bond Lengths91
	4.4.3.1 XANES93
	4.4.3.2 EXAFS96
4-5	First Principles Analysis of Fe Stability in Layered Oxides99
4-6	Conclusions100
	References102

Chapter 5 Understanding the Effects of Cationic Substitution on Redox

	Potential in Layered Compounds103
5.1	Ni Redox Potentials in Different Compounds103
5.2	Computation Details105
5.3	Electronic Structure of Transition Metal Ion105
5.4	Tuning the Voltage by the Inductive Effect107
5.5	Calculated Projected Density of States109
5.6	Experimental Evidence113
5.7	Conclusions116
	References118

Part II Understanding the Crystal Structure and Cationic Ordering in Lithium

	Manganese Oxides: $\text{Li}[\text{Ni}_x\text{Li}_{1/3-2x/3}\text{Mn}_{2/3-x/3}]\text{O}_2$ ($0 \leq x \leq 1/2$)119
--	------------------------------------------------------------------------------------------------------------------------------------------------	-----------------

Chapter 6 Review on the $\text{Li}[\text{Ni}_x\text{Li}_{1/3-2x/3}\text{Mn}_{2/3-x/3}]\text{O}_2$ system

6.1	Synthesis, Structure and Electrochemical Performance121
-----	------------------------------------------------------	----------

6.2	Anomalous Capacity when $0 \leq x < 1/2$124
6.3	Other Observations for $\text{LiNi}_{1/2}\text{Mn}_{1/2}\text{O}_2$125
6.4	First Principles and Monte Carlo study in the System127
6.5	Motivation and Objectives129
	References130

Chapter 7 Kinematics of Diffraction – TEM, XRD and ND132

7.1	Different Sources of Radiation and Their Interaction with Matter133
7.2	Simple Diffraction Physics136
7.2.1	The Bragg's Law and Laue Condition136
7.2.2	Real and Reciprocal Space137
7.2.3	Ewald Sphere Construction138
7.2.4	Perfect and Defective Crystal139
7.2.5	Kinematical Approximation and Dynamic Diffraction140
7.3	Powder Diffraction vs. Single Crystal Diffraction141
7.4	The Structure Determination Process141
7.5	Selected Area Electron Diffraction143
7.5.1	Indexing of Electron Diffraction Pattern146
7.5.2	Simulation of Electron Diffraction147
	References149

**Chapter 8 Understanding the Structure of $\text{LiNi}_x\text{Li}_{1/3-2x/3}\text{Mn}_{2/3-x/3}\text{O}_2$ by
Electron Diffraction Experiment and Powder Diffraction**

	Simulation150
8.1	Synthesis and XRD Characterization151

8.2	Long-Range Cation Ordering in $\text{LiNi}_x\text{Li}_{1/3-2x/3}\text{Mn}_{2/3-x/3}\text{O}_2$	155
8.2.1	Electron Diffraction Analysis on $\text{LiNi}_{1/2}\text{Mn}_{1/2}\text{O}_2$	155
8.2.2	Proposed Structure Model	158
8.2.3	X-ray and Neutron Powder Diffraction Simulation of $\text{LiNi}_{1/2}\text{Mn}_{1/2}\text{O}_2$	162
8.2.4	Electron Diffraction Analysis on $\text{LiNi}_{1/3}\text{Li}_{1/9}\text{Mn}_{5/9}\text{O}_2$ and Li_2MnO_3	165
8.3	Disorder in $\text{LiNi}_x\text{Li}_{1/3-2x/3}\text{Mn}_{2/3-x/3}\text{O}_2$ ($0 \leq x \leq 1/2$)	170
8.3.1	In-plane Disorder in $\text{LiNi}_{1/2}\text{Mn}_{1/2}\text{O}_2$	171
8.3.2	Stacking Disorder of the Ordered Planes	173
8.4	Conclusions	175
	References	176

Chapter 9 Stacking Disorder and Polytypism

	in $\text{LiNi}_x\text{Li}_{1/3-2x/3}\text{Mn}_{2/3-x/3}\text{O}_2$ ($0 \leq x \leq 1/2$)	178
9.1	Review on Li_2MO_3 System	178
9.2	First Principles Investigation	181
9.3	Polytypism and Stacking Faults in $\text{LiNi}_x\text{Li}_{1/3-2x/3}\text{Mn}_{2/3-x/3}\text{O}_2$	182
9.3.1	Stacking Disorder and Diffraction XRD Simulation	182
9.3.2	Polytypes and Electron Diffraction	184
9.4	Significance of Polytypism in Intercalation Compounds	187
9.5	Conclusions	188
	References	189

Chapter 10	Conclusions191
Appendix A		
Summary of Literature Review on Li_2MO_3 System	195

List of Figures

Figure 1-1 Principles of lithium ion battery - the cell is in discharge state.22
Figure 1-2 Comparison of the different battery technologies in terms of volumetric and gravimetric energy density.22
Figure 1-3 The O3 layered crystal structure, which is commonly observed in lithium transition metal oxides.26
Figure 1-4 The spinel structure. Notice that a set of tetrahedral sites that are available for lithium ions.26
Figure 1-5 Schematic illustration of the three layered structures O3, O1 and H1-3. The vertices of each octahedral are oxygen ions.27
Figure 1-6 Charge and discharge curves of a lithium cell with a) $\text{Li}[\text{Li}_{0.1}\text{Mn}_{1.9}]\text{O}_4$, b) LiCoO_2 , c) $\text{LiCo}_{1/2}\text{Ni}_{1/2}\text{O}_2$ and d) $\text{LiNi}_{1/2}\text{Mn}_{1/2}\text{O}_2$ as cathode, operated in voltage range 2.5-4.5V at $0.17\text{mA}/\text{cm}^2$ at room temperature.30
Figure 3-1 Ni, TM1 and TM2 ordering in the supercell of $\text{LiNi}_{1/3}\text{TM1}_{1/3}\text{TM2}_{1/3}\text{O}_2$42
Figure 3-2 Relative formation energy (E_{RF}) of $\text{Li}_x\text{Ni}_{1/3}\text{Fe}_{1/3}\text{Mn}_{1/3}\text{O}_2$ calculated with antiferromagnetic coupling in a supercell of six formula units.45
Figure 3-3 Calculated voltage curves for $\text{LiNi}_{1/3}\text{TM1}_{1/3}\text{TM2}_{1/3}\text{O}_2$ where $\text{TM1} = \text{Al}^{3+}$, Co^{3+} or Fe^{3+} and $\text{TM2} = \text{Mn}^{4+}$, Ti^{4+} or Zr^{4+}48
Figure 3-4 Ni, Fe, Co Mn ordering in the supercell of $\text{Li}(\text{Ni}_{1/3}\text{Fe}_{1/6}\text{Co}_{1/6}\text{Mn}_{1/3})\text{O}_2$50
Figure 3-5 Comparison of calculated average voltage curves of $\text{Li}_x\text{Ni}_{1/3}\text{Co}_{1/3}\text{Mn}_{1/3}\text{O}_2$ and $\text{Li}_x\text{Ni}_{1/3}\text{Fe}_{1/6}\text{Co}_{1/6}\text{Mn}_{1/3}\text{O}_2$51

Figure 3-6 Calculated density of states of $\text{Li}_x\text{Ni}_{1/3}\text{Fe}_{1/6}\text{Co}_{1/6}\text{Mn}_{1/3}\text{O}_2$ at a) $x = 1$, b) $x = 2/3$, c) $x = 1/3$, and d) $x = 0$54
Figure 3-7 Calculated lattice parameter a & c and volume at various lithium concentrations.55
Figure 3-8 Calculated transition metal - oxygen bond lengths (TM-O distances) of $\text{Li}_x\text{Ni}_{1/3}\text{Fe}_{1/6}\text{Co}_{1/6}\text{Mn}_{1/3}\text{O}_2$ ($0 \leq x \leq 1$)59
Figure 4-1 Process flow of heat treatment66
Figure 4-2 XRD spectra for $\text{LiNi}_{1/3}\text{Fe}_z\text{Co}_{1/3-z}\text{Mn}_{1/3}\text{O}_2$ at $z = 0$, $z = 1/6$, $z = 2/9$, $z = 5/18$, $z = 1/3$, all synthesized at 850°C67
Figure 4-3 XRD spectra of $\text{LiNi}_{1/3}\text{Co}_{1/6}\text{Fe}_{1/6}\text{Mn}_{1/3}\text{O}_2$ synthesized at 750°C , 800°C and 850°C68
Figure 4-4 SEM images of as-prepared $\text{LiNi}_{1/3}\text{Fe}_z\text{Co}_{1/3-z}\text{Mn}_{1/3}\text{O}_2$ at (a) $z = 1/6$, (b) $z = 2/9$, (c) $z = 1/3$, all synthesized at 850°C70
Figure 4-5 SEM images of as-prepared $\text{LiNi}_{1/3}\text{Co}_{1/6}\text{Fe}_{1/6}\text{Mn}_{1/3}\text{O}_2$ materials synthesized at (a) 750°C (b) 800°C and (c) 850°C71
Figure 4-6 XPS spectra of Fe edge (uncorrected) in $\text{LiNi}_{1/3}\text{Fe}_z\text{Co}_{1/3-z}\text{Mn}_{1/3}\text{O}_2$ a) $z = 1/6$, b) $z = 2/9$ and c) $z = 1/3$, all synthesized at 850°C75
Figure 4-7 Experimental and calculated Mössbauer spectra obtained at 293 K for $\text{LiNi}_{1/3}\text{Fe}_z\text{Co}_{1/3-z}\text{Mn}_{1/3}\text{O}_2$ with (a) $z = 1/6$ and (b) $z = 1/9$. (The dots are experimental values and the lines are calculated values)78
Figure 4-8 Crystal structure of ground state LiFeO_2 , with space group $I4_1/amd$79
Figure 4-9 Experimental and calculated Mössbauer spectra obtained at 4.2 K for $\text{LiNi}_{1/3}\text{Fe}_x\text{Co}_{1/3-x}\text{Mn}_{1/3}\text{O}_2$ with (a) $x = 1/6$ and (b) $x = 1/9$80

Figure 4-10 Variation of the cell potential on first charging then discharging the cells at C/10 for $\text{LiNi}_{1/3}\text{Fe}_{1/6}\text{Co}_{1/6}\text{Mn}_{1/3}\text{O}_2$ prepared at 750°C, 800°C and 850°C82
Figure 4-11 Comparison of experimental potential curve (sample synthesized at 750°C) with the predicted potential curve by first principles calculation.83
Figure 4-12 Charge and discharge capacity vs. cycle number curves of the $\text{LiNi}_{1/3}\text{Fe}_{1/6}\text{Co}_{1/6}\text{Mn}_{1/3}\text{O}_2$ materials synthesized at 750, 800, and 850°C for 16 h.84
Figure 4-13 Comparison of first cycle potential curve of $\text{LiNi}_{1/3}\text{Fe}_{1/6}\text{Co}_{1/6}\text{Mn}_{1/3}\text{O}_2$ with (a) and without (b) heat treatment of the electrode in the glove box85
Figure 4-14 First charge discharge curve comparison of $\text{LiNi}_{1/3}\text{Fe}_{1/6}\text{Co}_{1/6}\text{Mn}_{1/3}\text{O}_2$ and $\text{LiNi}_{1/3}\text{Fe}_{2/9}\text{Co}_{1/9}\text{Mn}_{1/3}\text{O}_2$86
Figure 4-15 Powder XRD spectra of charged $\text{LiNi}_{1/3}\text{Fe}_{1/6}\text{Co}_{1/6}\text{Mn}_{1/3}\text{O}_2$ (a) $x = 0.36$ and (b) $x = 0.77$90
Figure 4-16 Schematic representation of back-scattered photo-electron at the absorbing atom92
Figure 4-17 XANES spectra of a) Ni edge b) Fe edge c) Co edge and d) Mn edge of $\text{LiNi}_{1/3}\text{Fe}_{1/6}\text{Co}_{1/6}\text{Mn}_{1/3}\text{O}_2$95
Figure 4-18 EXAFS spectra of a) Ni edge b) Fe edge c) Co edge and d) Mn edge of $\text{LiNi}_{1/3}\text{Fe}_{1/6}\text{Co}_{1/6}\text{Mn}_{1/3}\text{O}_2$98
Figure 4-19 Energies of LAY: layered undefected structure; TRI: Fe defect in shared face between transition metal layer octahedron and Li layer tetrahedron; TET: Fe defect in Li layer tetrahedron100
Figure 5-1 Ni, $\text{TM}1^{3+}$, $\text{TM}2^{4+}$ ordering in the supercells of $\text{Li}(\text{Ni}_{1/3}\text{TM}1_{1/3}\text{TM}2_{1/3})\text{O}_2$ and $\text{Li}(\text{Ni}_{1/2}\text{TM}2_{1/2})\text{O}_2$105

Figure 5-2 Schematic illustration of the bonding and anti-bonding levels that arise for a transition metal ion octahedrally coordinated by oxygen ions. The splitting is due to the hybridization between the valence electronic states of the transition metal ion with those of the oxygen ions.106
Figure 5-3 Electronic configuration of octahedrally coordinated Ni ²⁺110
Figure 5-4 Projected density of states on Ni and O ions, notice that the energy is extended to low value in order to show the oxygen s-level, which is believed unchanged regardless of cation substitution. Fermi level is outlined by red line, by which it clearly shows that Ni redox potential is shifted to more negative value when Mn is substituted with Ti111
Figure 5-5 Projected density of states on Ni and O ions, notice that the energy is extended to low value in order to show the oxygen s-level, which is believed unchanged regardless of cation substitution. Fermi level is outlined by red line, by which it clearly shows that Ni redox potential is shifted to more positive value when Mn is substituted with Co112
Figure 5-6 Experimental charge-discharge curves of (a) LiNi _{1/2} Mn _{1/2} O ₂ and (b) Li _{0.9} Ni _{0.45} Ti _{0.55} O ₂ cut-off voltage: 4.8V113
Figure 5-7 Experimental voltage curve of LiNi _{1/3} Co _{1/3} Mn _{1/3} O ₂ with cut-off voltage 4.6V by Ohzuku & Makimura114
Figure 5-8 First-cycle charge and discharge curves of Li[Ni _{1/2} Mn _{1/2}]O ₂ and Li[Ni _{1/3} Co _{1/3} Mn _{1/3}]O ₂114
Figure 5-9 First-cycle charge and discharge curves of Li[Ni _{1/3} Co _{1/3} Mn _{1/3}]O ₂ and Li[Ni _{1/3} Fe _{1/6} Co _{1/6} Mn _{1/3}]O ₂115
Figure 5-10 First-cycle charge and discharge curves of Li[Ni _{1/3} Co _{1/3} Mn _{1/3}]O ₂ and Li[Ni _{1/3} Al _{1/6} Co _{1/6} Mn _{1/3}]O ₂115
Figure 5-11 First-cycle charge and discharge curves of Li[Ni _{1/2} Mn _{1/2}]O ₂ , Li[Ni _{0.475} Al _{0.05} Mn _{0.475}]O ₂ , and Li[Ni _{0.5} Mn _{0.45} Ti _{0.05}]O ₂116

Figure 6-1 a) Crystal structure of Li_2MnO_3 b) $(001)_{\text{hex}}$ projection of $\text{Li}_{1/3}\text{Mn}_{2/3}$ layer.	122
Figure 6-2 First charge discharge curve of cells at different temperatures for Li_2MnO_3 prepared at a) 500 °C and b) 800 °C	125
Figure 6-3 Zig-zag in-plane ordering of Ni and Mn in $\text{LiNi}_{1/2}\text{Mn}_{1/2}\text{O}_2$	127
Figure 6-4 Flower in-plane ordering of Ni and Mn in $\text{Li}_{1/12}\text{Ni}_{5/12}\text{Mn}_{1/2}$ layer of $\text{LiNi}_{1/2}\text{Mn}_{1/2}\text{O}_2$	128
Figure 7-1 Schematics of X-ray diffraction by planes of atoms	136
Figure 7-2 Relationship between $\Delta\mathbf{k}$ and θ for elastic scattering	137
Figure 7-3 Ewald sphere construction	139
Figure 7-4 The structure determination process	143
Figure 7-5 Selected Area Electron Diffraction (SAED) mode – tracing the rays to confirm that the intermediate aperture provides a sampling of the transmitted and all diffracted rays	145
Figure 7-6 The electron beam can be diffracted more than once – a phenomenon called dynamical scattering	146
Figure 8-1 Ternary phase diagram of LiNiO_2 - LiMnO_2 - Li_2MnO_3 . The solid line inside the triangle represents the solid solution $\text{LiNi}_x\text{Li}_{1/3-2x/3}\text{Mn}_{2/3-x/3}\text{O}_2$ ($0 \leq x \leq 1/2$)	151
Figure 8-2 X-ray powder diffraction spectra of a) $\text{LiNi}_{1/2}\text{Mn}_{1/2}\text{O}_2$ and b) $\text{LiNi}_{1/3}\text{Li}_{1/9}\text{Mn}_{5/9}\text{O}_2$, notice that the superstructure peaks become stronger when Ni content decreases.	152
Figure 8-3 a) Simulated and b) Experimental X-ray powder diffraction spectra of Li_2MnO_3	154

Figure 8-4 (a) $[1-1-1]_{\text{hex}}$. (b) $[-411]_{\text{hex}}$. (c) $[-25-1]_{\text{hex}}$. electron diffraction patterns of $\text{LiNi}_{1/2}\text{Mn}_{1/2}\text{O}_2$, which shows the superstructure reflections consistent with $\sqrt{3}a_{\text{hex}} \times \sqrt{3}a_{\text{hex}} \times c_{\text{hex}}$. superstructure with space group $P3_112$157
Figure 8-5 a-b plane on a) hexagonal setting and b) monoclinic setting of $\sqrt{3} \times \sqrt{3}$ superstructure cell on triangular lattices and their relations with parent hexagonal/monoclinic cell159
Figure 8-6 a) Proposed structure of $\text{LiNi}_{1/2}\text{Mn}_{1/2}\text{O}_2$ with $P3_112$ space group. b) $[001]_{\text{hex}}$. projection of three successive transition metal layers160
Figure 8-7 a) Crystal structure of Li_2MnO_3 with $C2/m$ space group, b) $[001]_{\text{hex}}$. projection of three successive transition metal layers and c) projection of the cell along $[010]_{\text{hex}}$. showing the relation between c_{mon} . and c_{hex}160
Figure 8-8 Calculated powder XRD spectrum of $\text{LiNi}_{1/2}\text{Mn}_{1/2}\text{O}_2$ with the proposed structure ($\lambda = 1.5406\text{\AA}$). Note that the superstructure peak intensities in the range of $20-30^\circ$ (see insert) are less than 1% of the maximum fundamental reflection peak intensity $(003)_{\text{hex}}$163
Figure 8-9 Calculated powder neutron diffraction spectra of proposed superstructures ($\lambda = 1.3230\text{\AA}$) with (a) $\alpha[0.27\text{Li}; 0.73\text{Ni}]$ and $\beta [0.75\text{Mn}; 0.25\text{Ni}]$; (b) $\alpha [0.27\text{Li}; 0.61\text{Ni}; 0.12\text{Mn}]$ and $\beta [0.69\text{Mn}; 0.31\text{Ni}]$165
Figure 8-10 a) $[001]_{\text{hex}}$. b) $[21-2]_{\text{hex}}$. electron diffraction patterns of $\text{LiNi}_{1/3}\text{Li}_{1/9}\text{Mn}_{5/9}\text{O}_2$, which shows the superstructure reflections consistent with $\sqrt{3}a_{\text{hex}} \times \sqrt{3}a_{\text{hex}} \times c_{\text{hex}}$. superstructure with space group $P3_112$167
Figure 8-11 a) $[-111]_{\text{hex}}$. b) $[001]_{\text{hex}}$. electron diffraction patterns of Li_2MnO_3 . Notices in b) there are extra reflections (indicated by arrows) that cannot be indexed with superstructure $P3_112$169
Figure 8-12 a) $[1-10]_{\text{hex}}$. electron diffraction pattern of $\text{LiNi}_{1/2}\text{Mn}_{1/2}\text{O}_2$, streaking perpendicular to c^* suggests in-plane ordering is not perfect. b) Simulated $[-110]_{\text{hex}}$. electron diffraction pattern of parent $R-3m$ cell171

Figure 8-13 a) Flower ordering $2\sqrt{3}a_{\text{hex}} \times 2\sqrt{3}a_{\text{hex}}$ superstructure, notice that the composition in flower ordering is $\text{Li}_{1/9}\text{Ni}_{1/3}\text{Mn}_{5/9}$. b) Typical $\sqrt{3}a_{\text{hex}} \times \sqrt{3}a_{\text{hex}}$ superstructure172
Figure 8-14 Simulated electron diffraction pattern with the flower-type ordering is compared with the $[1-10]_{\text{hex}}$. electron diffraction pattern of $\text{LiNi}_{1/2}\text{Mn}_{1/2}\text{O}_2$172
Figure 8-15 Two possible ways of stacking of $\sqrt{3}a_{\text{hex}} \times \sqrt{3}a_{\text{hex}}$ ordered planes, notice that only α sites are shown, and the superstructures are outlined by dashed lines173
Figure 9-1 Stacking sequence of C2/c structure: a) $[-110]$ projection b)[001] projection of the $\text{Li}_{1/3}\text{M}_{2/3}$ planes for Li_2MO_3179
Figure 9-2 Stacking sequences of a) P3_112 structure; b) C2/m structure for Li_2MO_3180
Figure 9-3 Relationship between the ionic radii of transition metals (M^{4+}) and lattice symmetry of Li_2MnO_3 . Rhombohedral and monoclinic lattice symmetries are represented by circle and solid ball, respectively.180
Figure 9-4 Comparison of experimental and Diffrac simulated powder XRD spectra183
Figure 9-5 Summary of experimentally observed electron diffraction zone axes for $\text{LiNi}_{1/2}\text{Mn}_{1/2}\text{O}_2$ and $\text{LiNi}_{1/3}\text{Li}_{1/9}\text{Mn}_{5/9}\text{O}_2$184
Figure 9-6 Simulated electron diffraction pattern from equivalent zone axis of a) C2/m b) C2/c and c) P3_112 , which well fit the experimentally obtained $[1-10]_{\text{hex}}$. zone axis electron diffraction pattern of $\text{LiNi}_{1/2}\text{Mn}_{1/2}\text{O}_2$186
Figure 9-7 $[1-10]_{\text{hex}}$. zone axis electron diffraction pattern of $\text{LiNi}_{1/2}\text{Mn}_{1/2}\text{O}_2$187

List of Tables

Table 3-I Calculated lattice parameters and transition metal –oxygen bond distances of $\text{Li}_x\text{Ni}_{1/3}\text{Co}_{1/6}\text{Fe}_{1/6}\text{Mn}_{1/3}\text{O}_2$60
Table 4-I Refined lattice parameters of as-prepared materials72
Table 4-II Rietveld refinement parameters for $\text{LiNi}_{1/3}\text{Fe}_{1/9}\text{Co}_{2/9}\text{Mn}_{1/3}\text{O}_2$ and $\text{LiNi}_{1/3}\text{Fe}_{1/6}\text{Co}_{1/6}\text{Mn}_{1/3}\text{O}_2$73
Table 4-III XPS binding energy for as-prepared materials76
Table 4-IV Mössbauer parameters obtained at 293 K78
Table 4-V Mössbauer parameters obtained at 4.2 K81
Table 4-VI XPS binding energy for as-prepared and partially-charged materials88
Table 4-VII Comparison of experimental and calculated lattice parameters at various lithium concentrations89
Table 5-I Calculated voltages of $\text{LiNi}_{1/3}\text{TM}_{1/3}\text{TM}_{2/3}\text{O}_2$ or $\text{LiNi}_{1/2}\text{TM}_{2/2}\text{O}_2$ systems104
Table 5-II Redox potential of transition metal cation in the O3 layered structure LiTMO_2108
Table 5-III Ionic radii, electronic configuration and electronegativity of various transition metal cations109

Table 8-I Site occupancies in $\text{LiNi}_x\text{Li}_{1/3-2x/3}\text{Mn}_{2/3-x/3}\text{O}_2$ ($0 \leq x \leq 1/2$)170
Table 9-I VASP calculated (GGA) total energies of different polytypes in Li_2MO_3 (M = Mn, Sn & Ti)181

Part I

Combining Ab Initio Computation with Experiments for Designing New High Energy Density Electrode

Materials: $\text{Li}[\text{Ni}_{1/3}\text{TM1}_{1/3}\text{TM2}_{1/3}]\text{O}_2$

CHAPTER 1

LITHIUM ION BATTERIES & THE ELECTRODE MATERIALS

Lithium ion batteries offer high energy density, flexible and light weight design and longer cycle life than other battery systems. [1] The share of worldwide sales for Li-ion portable batteries is 63%, much higher than those of Ni–Cd (23%) and Ni–MeH (14%) [2], which explains why this area receives most attention at both fundamental and applied levels. Lithium transition metal oxides are important positive electrode materials and are the focus of this thesis. In this chapter, we give a brief description of the electrochemistry in the lithium ion batteries and overview of the lithium intercalation compounds.

1.1 Lithium Ion Batteries

A battery is an energy storage and conversion device. It consists of several electrochemical cells that are connected in parallel and/or in series to provide the required capacity and voltage, respectively. Each cell has a negative (the anode in electrochemical cell) and a positive electrode (the cathode), as the sources of chemical reactions, separated by the non-aqueous electrolyte. The electrolyte contains dissociated salts, which provides an ion transport path between the two electrodes. The electrolyte takes no part in the reaction except for conveying the electroactive lithium ions during discharge from a high (chemical) energy state in the negative electrode to a low (chemical) energy state in the positive electrode while the electrons pass through the external circuit with a release of (electric)

energy. If such process is reversible, in another word, the chemical energy can be re-stored by supplying electric power; the device which undertakes this process is called a rechargeable battery, see Figure 1-1. Lithium ion battery is one of the dominant rechargeable battery technologies including nickel metal hydride battery (Ni-MH) because of its higher energy density and design flexibility, as shown in Figure 1-2.

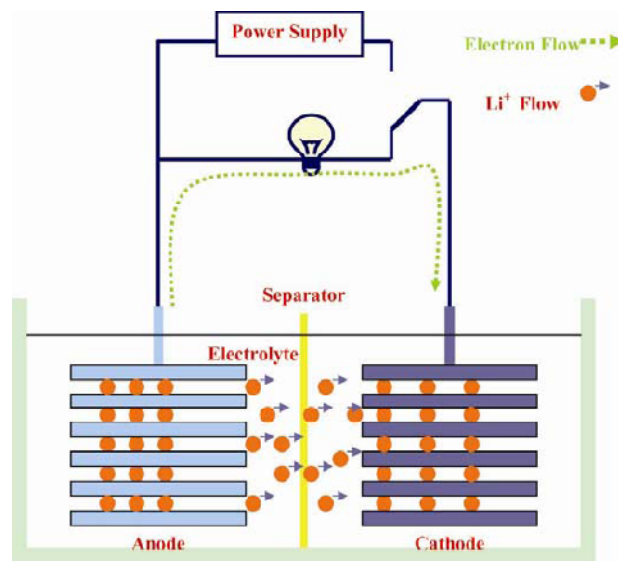


Figure 1-1 Principles of lithium ion battery - the cell is in discharge state.

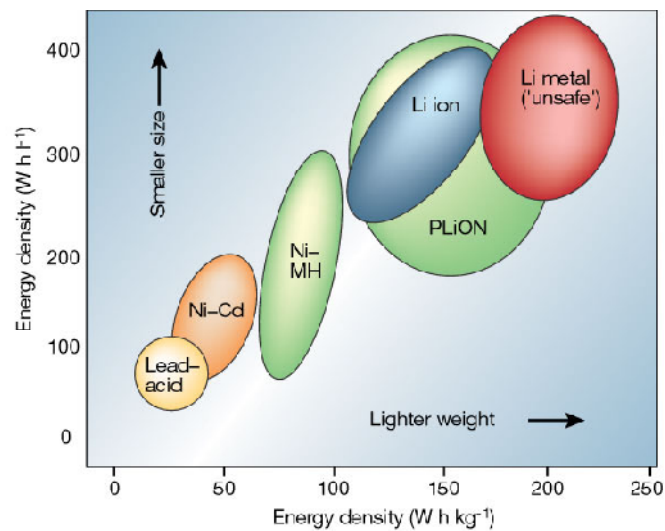


Figure 1-2 Comparison of the different battery technologies in terms of volumetric and gravimetric energy density [1].

The key parameters for electrode materials are:

- i) Gravimetric specific capacity in Ah/g or energy in Wh/g
- ii) Volumetric capacity in Ah/cm³
- iii) Rate capability (power density)
- iv) Cycleability (stability)
- v) Self-discharge (lifetime)
- vi) Cost
- vii) Toxicity (safety)

Considering any battery technology, measures of its performance (cell potential, capacity or energy density) are related to the intrinsic property of the materials that form the positive and negative electrodes. The cycle-life and lifetime are dependent on the nature of the electrode materials and electrode/electrolyte interfaces, whereas safety is a function of the stability of the electrode materials and interfaces.

1.2 Developments in Lithium Ion Battery Research

The first commercial lithium ion rechargeable battery was introduced by Sony Japan in 1989 [3]. Over the past three decades, Li rechargeable battery technology research has undergone three main stages in its research:

- In the 1970s, the discovery of intercalation compounds was crucial in the development of high-energy rechargeable lithium batteries [4]. In 1972, Exxon introduced a Li-metal/liquid electrolyte/TiS₂ battery [5]. However, uneven dendritic Li growth as the metal was re-plated during subsequent charge-discharge cycle caused explosion hazards. Substituting Li metal with alloys solved the dendrite

problem [6], but alloy electrodes survived only a limited number of cycles due to large volume changes during the charge-discharge operation.

- In the 1980s, the discoveries of more low-dimensional intercalation compounds and the use of carbon materials as the anodic lithium insertion material led to the Li-ion battery technology or the so-called rocking chair technology. Sony commercialized the rocking-chair cell with a potential exceeding 3.6V and gravimetric energy density as high as 120-150 Wh/Kg⁻¹ [3].
- The most recent development is the Li hybrid polymer electrolyte (Li-HPE) battery. ‘Hybrid’ means that the electrolyte consists three components: a polymer matrix swollen with liquid solvent and a salt. Bellcore researchers developed the first reliable and practical rechargeable Li-ion HPE battery [7], named plastic Li ion (PliON), which has been commercially developed since 1999.

The demands for energy storage in the future are unpredictable with more advanced portable electronic devices and more environment-friendly transportation. The state-of-the-art lithium ion batteries use carbon materials as the anode and LiCoO₂ as the cathode, whose capacity will hardly be able to meet the ever-increasing demand for larger, more stable capacity. The current commercial lithium ion batteries also have serious safety problem due to instability of the overcharged Li_xCoO₂ in the electrolyte; several explosions have been reported in year 2004 alone.

1.3 Materials for the Positive Electrode

1.3.1 Intercalation Compounds

The rechargeability of the battery depends on the reversibility of the reactions on the electrodes. Intercalation compounds are considered as ideal materials since they can accommodate guest species such as lithium over large concentration ranges. The guest species can enter and leave the crystal structure of intercalation compounds without causing any significant change in the host lattice. An important category of such compounds are transition metal oxides, which consist of close-packed planes of oxygen ions with transition metal ions occupying octahedral and/or tetrahedral interstitial sites.

A typical layered structure of transitional metal oxides is shown in Figure 1-3. It consists of closed – packed oxygen planes, stacked in ABCABC sequence. The lithium and transition metal ions are octahedrally coordinated with oxygen ions and form alternate layers. A two-dimensional (sheet) channel for lithium ion transportation is available. This structure belongs to the R-3m space group and is often referred as the O3 form (α -NaFeO₂ iso-structure) [8]. LiCoO₂ adopts such crystal structure and is used as the current cathode material for commercial lithium ion battery. Other layered structures with different oxygen stacking sequences are observed, such as ABABAB in the deintercalated CoO₂ [9].

In addition, if the transition metal and lithium ions are distributed in such a way that $\frac{3}{4}$ of the transition metal ions occupy octahedral sites in alternating layers in the O3 oxygen frame while the remaining $\frac{1}{4}$ reside in the other alternating layers, such form is called the spinel crystal structure [10]. As shown in Figure 1-4, a subset of

tetrahedral interstitial sites is available for lithium. Notice that this structure also has the ABCABC oxygen stacking sequence.

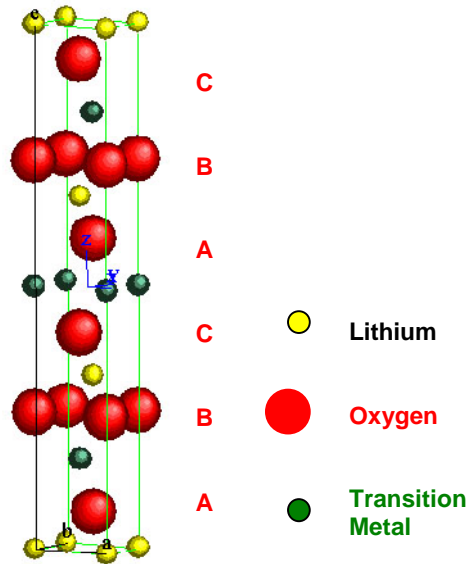


Figure 1-3 The O3 layered crystal structure, which is commonly observed in lithium transition metal oxides.

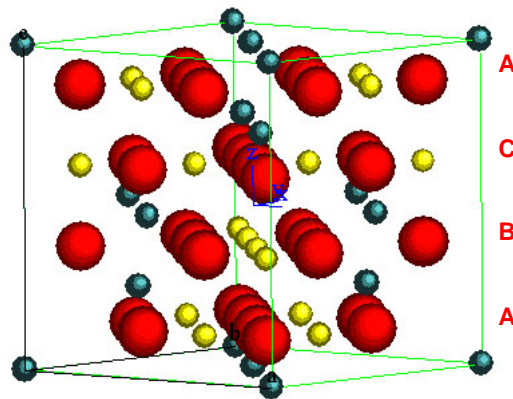


Figure 1-4 The spinel structure. Notice that a set of tetrahedral sites that are available for lithium ions.

1.3.2 LiCoO₂ vs. LiNiO₂

O3 layered LiCoO₂ has been studied thoroughly with experiments as well as first-principles computation [11-16]. It can be easily synthesized and enables a fast and reversible lithium intercalation over a large lithium concentration interval. In

practice delithiation is limited to the value $x = 0.5$ for safety reason though it is feasible to reversibly cycle LiCoO_2 beyond 0.5Li . [17] In agreement with experiment, first principles calculations predict that O3 is stable at intermediate to high lithium concentration and that O1 is stable when the compound is fully delithiated. [18] Calculations also predict that H1-3 is stable at low lithium concentration. H1-3 is a hybrid between the O3 and O1 structures, as shown below in Figure 1-5 [19].

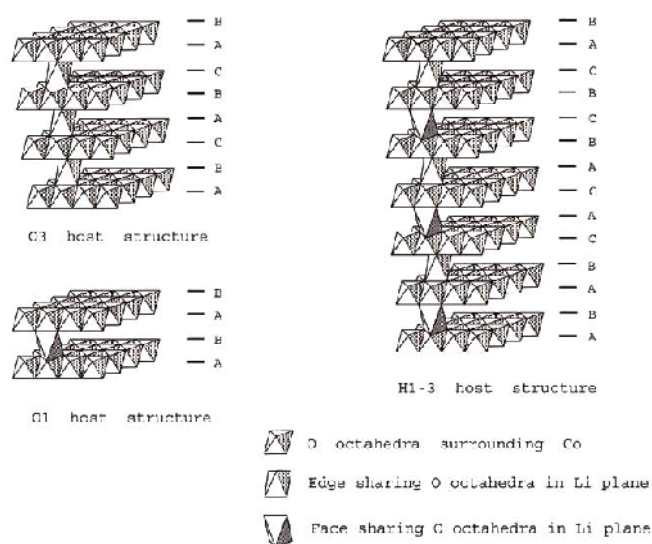


Figure 1-5 Schematic illustration of the three layered structures O3, O1 and H1-3. The vertices of each octahedral are oxygen ions.

Due to the high cost and toxicity associated with LiCoO_2 , the use of layered LiNiO_2 was considered as it also has favorable specific capacity compared with LiCoO_2 . However, expectations were dismissed for safety reasons as exothermic oxidation occurs between the organic electrolyte and the collapsing delithiated Li_xNiO_2 structure [20-23]. Both experimental and computational investigations show that a monoclinic distortion occurs upon delithiation. The coupling between the Li-vacancy ordering and the Jahn-Teller activity of Ni^{3+} ions is the origin of the

monoclinic distortion [24]. In addition, high quality LiNiO_2 samples are very difficult to synthesize, owing to the fact that Ni^{3+} and Li^+ have similar ionic radii and are easily mixed in the layered structure.

Delithiated Li_xCoO_2 was found to be more thermally stable than its Li_xNiO_2 counterpart. Thus, substitution of Co for Ni in $\text{LiNi}_{1-x}\text{Co}_x\text{O}_2$ was adopted to provide a partial solution to the safety concerns [25, 26]. Furthermore, with electrochemically inert cationic substitute for Ni or Co with Al, Mg or Ti, practical capacities beyond 180mAh/g can be obtained [27].

1.3.3 LiMnO_2

Lithium manganese oxide in the O3 layered structure has been regarded as a promising positive electrode material for rechargeable lithium batteries [17] [28]. It exhibits a smoother voltage profile and has higher lithium content than other lithium manganese oxide structures such as the spinel (LiMn_2O_4). Unfortunately, the thermodynamically stable phase of LiMnO_2 does not have the $\alpha\text{-NaFeO}_2$ structure, and all pure or lightly doped layered forms of layered- LiMnO_2 have been found to transform to a defective spinel-like structure upon cycling in a battery with significant change in voltage profile [29-31]. The stability of the compound has hindered its application in practice. The similar LiCoO_2 compound does not readily transform from layered to spinel even though such a transformation is thermodynamically favored in both Li_xMnO_2 and Li_xCoO_2 . [32] Computational studies by Reed & Ceder demonstrate that these two materials differ in performance due to kinetic rather than thermodynamic factors [33].

In the first stage of layer-to-spinel transformation, a significant fraction of the Mn and Li ions rapidly occupy tetrahedral sites, forming a metastable intermediate. The second stage of layer-to-spinel transformation involves a more difficult coordinated rearrangement of Mn and Li ions to form spinel. The susceptibility of Mn migration into the Li layer is found to be controlled by its oxidation state. The Jahn-Teller active Mn^{3+} ions likely charge disproportionate to Mn^{2+} and Mn^{4+} upon delithiation and Mn^{2+} favors a tetrahedral coordination with oxygen which leads to the layer-to-spinel transformation. The mechanism of the transformation and strategies to inhibit such transformation is well explained based on the ligand field theory. [33, 34]

1.3.4 Multi-Cation Systems

Recently, layered di- and tri- transition metal oxides have become the trend in cathode materials research. Among these intercalation compounds, nickel manganese based oxide and their derivatives are considered to be one of the most promising candidates for future lithium ion batteries [35-40]. The general formula for this system is $\text{Li}[\text{Ni}_x\text{Li}_{1/3-2x/3}\text{Mn}_{2/3-x/3}]\text{O}_2$ ($0 \leq x \leq 1/2$), among which $\text{LiNi}_{1/2}\text{Mn}_{1/2}\text{O}_2$ has gained significant amount of attention. It is confirmed both by experiments and first-principles calculations that in the as-prepared $\text{LiNi}_{1/2}\text{Mn}_{1/2}\text{O}_2$, only Ni^{2+} and Mn^{4+} ions are present.[39, 41, 42] Therefore nickel can exchange two electrons and be oxidized to Ni^{4+} which manganese remains at a 4+ oxidation state during the charge-discharge cycle without any loss of theoretical capacity, and without the instabilities associated with more reduced states of Mn. Detailed experimental studies show that though this phase has a O3 layered structure; some (about 9%) Ni^{2+} was found in lithium sites, by XRD Rietveld refinement [35, 36]. ^6Li MAS NMR confirmed the presence of Li^+ in the transition metal layer [43, 44].

Theoretically, this material has a high capacity of 280 Ah/Kg assuming all Ni^{2+} are oxidized to Ni^{4+} ; experimentally the material exhibits different capacity and cycling performance with different preparation methods and synthesis conditions. Y. Makimura et al. obtained a reversible capacity of 200 Ah/Kg in the potential window 2.5-4.5V and a good cycling efficiency up to 30 cycles [40]. Z.Lu et al. reported a stable capacity of 140 Ah/Kg between 3 to 4.4V and 200Ah/Kg between 2.5V to 4.8V.[36] A comparison of the electrochemical performance among LiCoO_2 , LiMn_2O_4 and $\text{LiCo}_{1/2}\text{Ni}_{1/2}\text{O}_2$ with $\text{LiNi}_{1/2}\text{Mn}_{1/2}\text{O}_2$ is illustrated in Figure 1-6 [45].

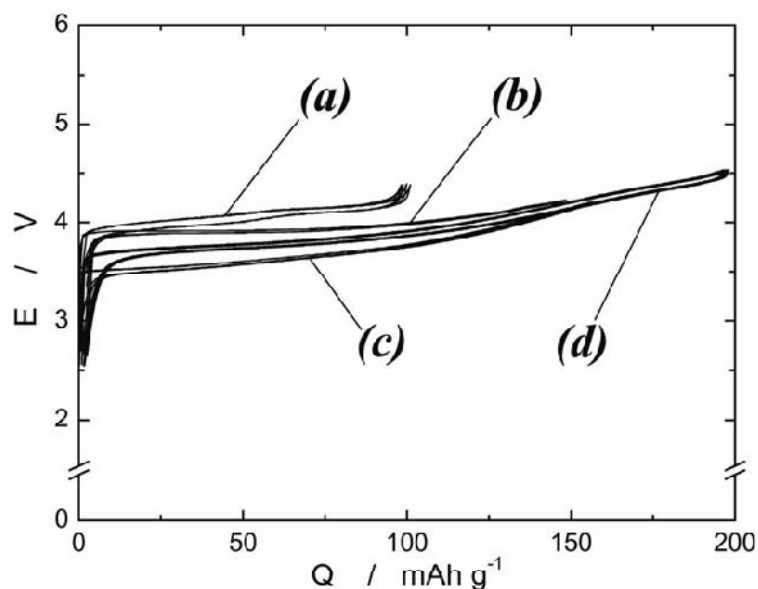


Figure 1-6 Charge and discharge curves [45] of a lithium cell with a) $\text{Li}[\text{Li}_{0.1}\text{Mn}_{1.9}]\text{O}_4$, b) LiCoO_2 , c) $\text{LiCo}_{1/2}\text{Ni}_{1/2}\text{O}_2$ and d) $\text{LiNi}_{1/2}\text{Mn}_{1/2}\text{O}_2$ as cathode, operated in voltage range 2.5-4.5V at $0.17\text{mA}/\text{cm}^2$ at room temperature.

$\text{LiNi}_{1/3}\text{Co}_{1/3}\text{Mn}_{1/3}\text{O}_2$ was also found to have very good electrochemical properties [46-49]. It is an attractive candidate for cathode material due to its ease of synthesis and excellent capacity retention. Ohzuku et al. reported that this compound has 200

mAh/g in the voltage range of 3.5-5V with negligible capacity loss up to 30 cycles [46]. Hwang et al. obtained reversible capacity of 188 mAh/g in the potential window of 3 to 4.5V [49]. Shaju et al. inferred from cyclic voltammetry results that the redox processes at 3.8V and 4.6V correspond to the $\text{Ni}^{2+}/\text{Ni}^{4+}$ and $\text{Co}^{3+}/\text{Co}^{4+}$ couples, respectively, though the capacity contributed by the latter redox pair is very small in this potential window [47]. First principles calculation confirmed that Co^{3+} is only oxidized to Co^{4+} at rather high voltage in this material [49, 50].

1.4 Motivation & Objectives

$\text{LiNi}_{1/2}\text{Mn}_{1/2}\text{O}_2$ and $\text{LiNi}_{1/3}\text{Co}_{1/3}\text{Mn}_{1/3}\text{O}_2$ illustrates the recent trend towards multi-component transition metal oxides, which creates a large number of possible compositional choices. The materials development including synthesis, processing, characterization and optimization, can be more efficient and cost effective if we have the ability to do accurate property predication and optimization during the materials design stage and prior to synthesis.

While first principles methods are not accurate enough to exactly predict voltages, it can act as a powerful pre-screening tool. It can predict the trend in voltages for different redox couples satisfactorily. Moreover, computational modeling can help to gain in-depth understanding of the experimental data. In this research, our goal is to show how first principles methods can be combined with various experimental tools to shorten the development cycle of a new material. The specific objectives are:

- Identify the best potential candidates cathode materials in the multi- cationic system with O3 layered structure (TM = Ni, Co, Mn, Fe, Mo, Ti, Zr, etc.) based on their lithium intercalation potentials and electronic structures.
- Synthesize and characterize the candidate materials, and optimize their electrochemical properties.
- Understand the crystal structure and electronic structure of the candidate materials at various lithium concentration

It is hoped that such direct integration of first principles methods with experimental research will aid the discovery of new electrode materials and shorten the development cycle of such materials.

References

1. J.-M. Tarascon and M. Armand, *Issues and challenges facing rechargeable lithium batteries*. Nature, 2001. **414**: p. 359.
2. H. Takeshita, *Proc. Conf. Power*. 2000. San Diego.
3. *Handbook of Battery Materials*, ed. J.O. Besenhard. 1999, Weinheim, Germany: Wiley-VCH.
4. B.C.H. Steele, *Fast Ion Transport in Solids*, ed. W. Van Gool. 1973, Amsterdam: North-Holland. p.103-109.
5. M.S. Whittingham, *Electrical Energy Storage and Intercalation Chemistry*. Science, 1976. **192**: p. 1126-1127.
6. B.M.L. Rao, Francis, R.W. and Christopher, H.A., Journal of the Electrochemical Society, 1977. **124**: p. 1490-1492.
7. J.M. Tarascon, et al., *Performance of Bellcore's plastic rechargeable Li-ion batteries*. Journal of Power Sources, 1996. **86-88**: p. 49-54.
8. C. Delmas, C. Fouassier, and P. Hagenmuller, *Structural classification and properties of the layered oxides*. Physica, 1980. **99B**: p. 81.
9. G.G. Amatucci, J.M. Tarascon, and L.C. Klein, *CoO₂, the end member of the Li_xCoO₂ solid solution*. J. Electrochem. Soc., 1996. **143**(3): p. 1114-1123.
10. W.D. Kingery, Bowen, H.K. and Uhlmann, D.R., *Introduction to Ceramics*. 1960, New York: John Wiley and Sons.
11. K. Mizushima, et al., *Li_xCoO₂ (0<x<=1) : a new cathode material for batteries of high energy density*. Materials Research Bulletin, 1980. **15**: p. 783-789.
12. H.J. Orman and P.J. Wiseman, *Cobalt (III) lithium oxide, LiCoO₂ : structure refinement by powder neutron diffraction*. Acta Cryst., 1984. **C(40)**: p. 12-14.
13. A. Van der Ven, et al., *First-principles investigation of phase stability in Li_xCoO₂*. Physical Review B, 1998. **58**(6): p. 2975-2987.
14. G. Ceder and A. Vandervan, *Phase diagrams of lithium transition metal oxides: investigations from first principles*. Electrochimica Acta, 1999. **45**(1-2): p. 131-150.
15. J.N. Reimers and J.R. Dahn, *Electrochemical and In Situ X-Ray Diffraction Studies of Lithium Intercalation in Li_xCoO₂*. J. Electrochem. Soc., 1992. **139**(8): p. 2091-2097.
16. T. Ohzuku and A. Ueda, *Solid-state redox reactions of LiCoO₂ (R-3m) for 4 volt secondary lithium cells*. J. Electrochem. Soc., 1994. **141**(11): p. 2972-2977.
17. A.R. Armstrong, et al., *The layered intercalation compounds Li(Mn_{1-y}Co_y)O₂: Positive electrode materials for lithium-ion batteries*. Journal of Solid State Chemistry, 1999. **145**(2): p. 549-556.
18. A. Van der Ven, M.K. Aydinol, and G. Ceder, *First-principles evidence for stage ordering in Li_xCoO₂*. J. Electrochem. Soc., 1998. **145**(6): p. 2149-2155.
19. A. Van der Ven, *First Principles Investigation of the Thermodynamic and Kinetic Properties of Lithium Transition Metal Oxides*, in *Department of Materials Science and Engineering*. 2000, Massachusetts Institute of Technology: Cambridge. p. 164.
20. J.R. Dahn, et al., *Rechargeable LiNiO₂/Carbon cells*. J. Electrochem. Soc., 1991. **138**(8): p. 2207-2211.

21. T. Ohzuku, A. Ueda, and M. Nagayama, *Electrochemistry and structural chemistry of $\text{LiNiO}_2(\text{R}3\text{m})$ for 4 volt secondary lithium cells*. J. Electrochem. Soc., 1993. **140**(7): p. 1862-1870.
22. A. Rougier, P. Gravereau, and C. Delmas, *Optimization of the composition of the $\text{Li}_{1-z}\text{Ni}_{1+z}\text{O}_2$ electrode materials: structural, magnetic, and electrochemical studies*. Journal of the Electrochemical Society, 1996. **143**(4): p. 1168-1174.
23. M.E. Arroyo de Dompablo, A. Van der Ven, and G. Ceder, *First-principles calculations of lithium ordering and phase stability on Li_xNiO_2* . Physical Review B, 2002. **66**(6): p. 064112.
24. M.E. Arroyo y de Dompablo, A. Van der Ven, and G. Ceder, *On the origin of the monoclinic distortion in Li_xNiO_2* . Chemistry of Materials, 2003. **15**(1): p. 63-67.
25. C. Delmas and I. Saadoune, *Electrochemical and physical properties of the $\text{Li}_x\text{Ni}_{1-y}\text{Co}_y\text{O}_2$ phases*. Solid State Ionics, 1992. **53-56**: p. 370.
26. C. Delmas, et al., *An overview of the $\text{Li}(\text{Ni},\text{M})\text{O}_2$ systems : syntheses, structures and properties*. Electrochimica Acta, 1999. **45**: p. 243-253.
27. G. Yuan, M.V. Yakovleva, and W. Ebner, *Novel $\text{LiNi}_{1-x}\text{Ti}_{x/2}\text{Mg}_{x/2}\text{O}_2$ compounds as cathode materials for safer lithium ion batteries*. Electrochemical and Solid State Letters, 1998. **1**(117-119).
28. B. Ammundsen, et al., *Formation and structural properties of layered LiMnO_2 cathode materials*. Journal of the Electrochemical Society, 2000. **147**(11): p. 4078-4082.
29. G. Vitins and K. West, *Lithium Intercalation into Layered LiMnO_2* . Journal of the Electrochemical Society, 1997. **144**(8): p. 2587-2592.
30. A. Blyr, et al., *Self-discharge of $\text{LiMn}_2\text{O}_4/\text{C}$ Li-ion cells in their discharged state - Understanding by means of three-electrode measurements*. Journal of the Electrochemical Society, 1998. **145**(1): p. 194-209.
31. Y. Shao-Horn, et al., *Structural characterization of layered LiMnO_2 electrodes by electron diffraction and lattice imaging*. Journal of the Electrochemical Society, 1999. **146**(7): p. 2404-2412.
32. A. Van der Ven and G. Ceder, *Electrochemical properties of spinel Li_xCoO_2 : A first-principles investigation*. Physical Review B - Condensed Matter, 1999. **59**(2): p. 742-749.
33. J. Reed, G. Ceder, and A. Van Der Ven, *Layered-to-spinel phase transition in Li_xMnO_2* . Electrochemical and Solid-State Letters, 2001. **4**(6): p. A78.
34. J. Reed, *Ab Initio Study of Cathode Materials for Lithium Batteries*, in *Department of Materials Science and Engineering*. 2003, Massachusetts Institute of Technology: Cambridge, MA. p. 311.
35. Z.H. Lu, et al., *Synthesis, structure, and electrochemical behavior of $\text{LiNi}_x\text{Li}_{1/3-2x/3}\text{Mn}_{2/3-x/3}\text{O}_2$* . Journal of the Electrochemical Society, 2002. **149**(6): p. A778-A791.
36. Z.H. Lu and J.R. Dahn, *Understanding the anomalous capacity of $\text{Li}/\text{LiNi}_x\text{Li}_{(1/3-2x/3)}\text{Mn}_{(2/3-x/3)}\text{O}_2$ cells using in situ X-ray diffraction and electrochemical studies*. Journal of the Electrochemical Society, 2002. **149**(7): p. A815-A822.
37. Z.H. Lu, Z.H. Chen, and J.R. Dahn, *Lack of cation clustering in $\text{LiNi}_x\text{Li}_{1/3-2x/3}\text{Mn}_{2/3-x/3}\text{O}_2$ ($0 < x \leq 1/2$) and $\text{LiCr}_x\text{Li}_{(1-x)/3}\text{Mn}_{(2-2x)/3}\text{O}_2$ ($0 < x < 1$)*. Chemistry of Materials, 2003. **15**(16): p. 3214-3220.

38. Y. Makimura, and T. Ohzuku, *Lithium insertion material of $\text{LiNi}_{1/2}\text{Mn}_{1/2}\text{O}_2$ for advanced lithium-ion batteries*. Journal of Power Sources, 2003. **119**: p. 156-160.
39. J. Reed and G. Ceder, *Charge, potential, and phase stability of layered $\text{Li}(\text{Ni}_{0.5}\text{Mn}_{0.5})\text{O}_2$* . Electrochemical and Solid State Letters, 2002. **5**(7): p. A145-A148.
40. T. Ohzuku and Y. Makimura, *Layered lithium insertion material of $\text{LiNi}_{1/2}\text{Mn}_{1/2}\text{O}_2$: A possible alternative to LiCoO_2 for advanced lithium-ion batteries*. Chemistry Letters, 2001(8): p. 744-745.
41. H. Kobayashi, et al., *Structural determination of $\text{Li}_{1-y}\text{Ni}_{0.5}\text{Mn}_{0.5}\text{O}_2$ ($y=0.5$) using a combination of Rietveld analysis and the maximum entropy method*. Journal of Materials Chemistry, 2004. **14**(1): p. 40-42.
42. W.S. Yoon, et al., *In situ X-ray absorption spectroscopic study on $\text{LiNi}_{0.5}\text{Mn}_{0.5}\text{O}_2$ cathode material during electrochemical cycling*. Chemistry of Materials, 2003. **15**(16): p. 3161-3169.
43. C.P. Grey, and Y.J. Lee, *Lithium MAS NMR studies of cathode materials for lithium-ion batteries*. Solid State Sciences, 2003. **5**(6): p. 883-894.
44. W.S. Yoon, et al., *Local structure and cation ordering in O3 lithium nickel manganese oxides with stoichiometry $\text{LiNi}_x\text{Mn}_{(2-x)/3}\text{Li}_{(1-2x)/3}\text{O}_2$ - NMR studies and first principles calculations*. Electrochemical and Solid State Letters, 2004. **7**(7): p. A167-A171.
45. Y. Makimura, N. Nakayama, and T. Ohzuku. *Structural Chemistry and Electrochemistry of $\text{LiNi}_{1/2}\text{Mn}_{1/2}\text{O}_2$ for Advanced Lithium Batteries*. in *The Electrochemical Society Meeting*. 2003. Paris France.
46. T. Ohzuku and Y. Makimura, *Layered lithium insertion material of $\text{LiCo}_{1/3}\text{Ni}_{1/3}\text{Mn}_{1/3}\text{O}_2$ for lithium-ion batteries*. Chemistry Letters, 2001(7): p. 642-643.
47. K.M. Shaju, G.V.S. Rao, and B.V.R. Chowdari, *Performance of layered $\text{Li}(\text{Ni}_{1/3}\text{Co}_{1/3}\text{Mn}_{1/3})\text{O}_2$ as cathode for Li-ion batteries*. Electrochimica Acta, 2002. **48**(2): p. 145-151.
48. I. Belharouak, et al., *$\text{Li}(\text{Ni}_{1/3}\text{Co}_{1/3}\text{Mn}_{1/3})\text{O}_2$ as a suitable cathode for high power applications*. Journal of Power Sources, 2003. **123**(2): p. 247-252.
49. B.J. Hwang, et al., *A combined computational/experimental study on $\text{LiNi}_{1/3}\text{Co}_{1/3}\text{Mn}_{1/3}\text{O}_2$* . Chemistry of Materials, 2003. **15**(19): p. 3676-3682.
50. Koyama, Y., et al., *Crystal and electronic structures of superstructural $\text{Li}_{1-x}\text{Co}_{1/3}\text{Ni}_{1/3}\text{Mn}_{1/3}\text{O}_2$ ($0 \leq x \leq 1$)*. Journal of Power Sources, 2003. **119**: p. 644-648.

CHAPTER 2

FIRST PRINCIPLES COMPUTATION

First principles methods are distinguished from empirical methods since they require only nuclear charges and number of electrons as inputs, without any adjustable experimental parameters. Through the application of quantum mechanics, the structure and properties of a substance can be calculated. Over the past few years, first principles methods have been proven as excellent complementary tools to laboratory experiments in the research of cathode materials for lithium ion battery [1-3]. In some case, the first principles methods even led the experiments to the discovery of new phases in these systems [4]. We believe that direct integration of the first principles computation with various experiments will significantly shorten the development cycle of new electrode material. In this chapter, we will discuss briefly the method applied in this work and what approximations are assumed in calculations of the physical quantities.

2.1 Quantum Mechanics and First Principles Energies

First principles methods can control and manipulate a modeled system at atomic scale; therefore characteristics of such a system can be more precisely calculated provided that this modeled system reflects the real system. Lithium transition metal oxides are complex solids, for such many bodied systems, a number of approximations must be made in order to obtain a solution for the many-body wave function ψ .

The first approximation is the Born-Oppenheimer approximation where the electrons are assumed to move so much faster than the nuclei that the nuclei can be treated as stationary. This approximation allows a separate wave function ψ that contains information about electrons only to be determined, thus the Schrödinger equation can be expressed as

$$H\psi = E\psi \quad \text{Eq. 2 -1}$$

Where H is the Hamiltonian operator for the solid, E is the total energy of the solid and ψ is the wave function describing N electrons. The electronic wave functions that satisfy the Schrödinger equation must be anti-symmetric to obey the Pauli Exclusion Principle. The coordinates of nuclei act only as parameters in the Schrödinger equation, and the interaction between the electrons and the nuclei of the solid is represented as the Ewald energy arising from the coulombic interactions. The Hamiltonian operator can be written in atomic units as

$$H = T + V_{ee} + \sum_j v(\vec{r}_j) + \sum_n \sum_{m < n} \frac{Z_m Z_n}{|\vec{R}_m - \vec{R}_n|} \quad \text{Eq. 2 -2}$$

T describes the electronic kinetic energy, V_{ee} is the coulomb interactions between the different electrons and $v(\vec{r})$ is the coulomb potential due to the nuclei of the solid.

For many bodied system, solving the above many body Schrödinger equation is intractable. Variational approximation says that for any square integrable function φ , an upper bound for the ground state energy E_0 of the system governed by the Hamiltonian H is provided by [5]

$$E[\varphi] = \frac{\langle \varphi | H | \varphi \rangle}{\langle \varphi | \varphi \rangle} \geq E_0 \quad \text{Eq. 2 -3}$$

φ is solved for $\partial E(\varphi) = 0$ but a trial function has to be determined to start with the variational minimization of energy.

One type of trial function is a Slater determinant of single electron orbitals, such a method is called the Hartree-Fock method [6]. However in this thesis, we focus on the first principles method based on the Density Functional Theory.

2.2 Density Functional Theory

DFT has some advantages over the Hartree-Fock method in terms of accuracy and simplicity. As proven by Hohenberg and Kohn [7], the ground-state properties of a crystal are uniquely determined by the electron density $\rho(\vec{r})$

$$\rho(\vec{r}) = \langle \psi | \sum_j \delta(\vec{r} - \vec{r}_j) | \psi \rangle \quad \text{Eq. 2-4}$$

The fundamental theorems of DFT state that the ground state energy $E[\rho(\vec{r})]$ of a solid is a function of the electron density [7]

$$E[\rho(\vec{r})] = F[\rho(\vec{r})] + \int \rho(\vec{r}) v(\vec{r}) d\vec{r} \quad \text{Eq. 2-5}$$

where $F[\rho(\vec{r})] = \langle \psi | T + V_{ee} | \psi \rangle$ is a universal function. ψ is the electronic wave function that minimizes $\langle \psi | T + V_{ee} | \psi \rangle$ with the constraint that ψ produces the electron density $\rho(\vec{r})$. $F[\rho(\vec{r})]$ is independent of the nuclear arrangement and charge, according to DFT if it is known then the ground state energy can be uniquely determined. [6, 7]

Kohn and Sham introduced a separation of $F[\rho(\vec{r})]$ by writing it as [8]

$$F[\rho] = T[\rho] + J[\rho] + E_{xc}[\rho] \quad \text{Eq. 2-6}$$

where $T[\rho]$ is the kinetic energy of a system of non-interacting electrons. $J[\rho]$ is the classical Coulomb energy, often referred as the Hartree term, and $E_{xc}[\rho]$ is called the exchange-correlation energy. $E_{xc}[\rho]$ includes the difference between the kinetic energy of a system of independent electrons and the kinetic energy of the actual interacting system with the same density.

2.3 LDA and GGA

The most common (and simplest) approximation to E_{xc} is the local density approximation (LDA) proposed by Kohn and Sham [8]. In LDA, the exchange correlation energy per electron at \vec{r} is set equal to the exchange correlation energy per electron of a homogeneous electron gas with the same density. Therefore, the local density approximation is a good approximation for system with a slowly varying electron density. For solids in which the electronic states are highly localized in space, we can expect LDA to break down since it cannot capture the strong correlations between the localized electrons.

The generalized gradient approximation (GGA) is developed by Perdew and Yue [6] in order to address the major source of error in LDA. GGA attempts to capture some of the deviation of the exchange-correlation energy from the uniform electron gas result [9]. It has been well-accepted that GGA is more suitable in systems where the electronic states are highly localized in space, such as the lithium transition metal oxides.

Many numerical techniques exist for solving the Kohn-Sham equations. For oxides, one of the most reliable methods is called the pseudopotential method [10-12], which is applied in this work. In the pseudopotential method, the effects of the core electrons around the ions that do not participate in bonding are replaced by pseudopotential. The pseudopotential approximation is valid as long as the core electrons do not participate in the bonding of the solid. Their wave functions and energy levels are negligible when the atom is placed in different environments. For most of the solids, this approximation is valid.

2.4 VASP

The first principles method used in this work is called “Vienna Ab Initio Software Package” or VASP [13, 14]. VASP solves the Kohn-Sham equations iteratively for valence orbitals using ultra-soft pseudopotentials determined from first principles. The exchange-correlation energy functional is spin-polarized GGA. This is due to the fact that for lithium manganese oxides spin polarized GGA correctly calculated ground states that were not obtained by the LDA method [15].

References:

1. G. Ceder, et al., *Identification of cathode materials for lithium batteries guided by first-principles calculations*. Nature, 1998. **392**: p. 694-666.
2. G. Ceder, *Predicting properties from scratch*. Science, 1998. **280**: p. 1099-1104.
3. G. Ceder, et al., *Computational modeling and simulation for rechargeable batteries*. Mrs Bulletin, 2002. **27**(8): p. 619-623.
4. G. Ceder and A. Van der ven, *Phase diagrams of lithium transition metal oxides: investigations from first principles*. Electrochimica Acta, 1999. **45**(1-2): p. 131-150.
5. B.H. Bransden and C.J. Joachin, *Introduction to Quantum Mechanics*. 1989: Longman Group UK Limited.
6. R.G. Parr and W. Yang, *Density-Functional Theory of Atoms and Molecules*. 1989, Oxford England: Clarendon Press.
7. P. Hohenberg and W. Kohn, *Inhomogeneous electron gas*. Physical Review, 1964. **136**(3B): p. 864.
8. W. Kohn and L.J. Sham, *Self-consistent equation including exchange and correlation effects*. Physical Review, 1965. **140**(4A): p. 1133.
9. K. Ohno, K. Esfarjani, and Y. Kawazoe, *Computational Materials Science: from ab initio to Monte Carlo Methods*. 1999, Berlin: Springer.
10. A.F. Kohan and G. Ceder, *Calculation of total energies in multicomponent oxides*. Computational Materials Science, 1997. **8**(1-2): p. 142-152.
11. M.C. Payne, et al., *Iterative Minimization Techniques for Abinitio Total-Energy Calculations - Molecular-Dynamics and Conjugate Gradients*. Reviews of Modern Physics, 1992. **64**(4): p. 1045-1097.
12. A.F. Kohan, *Total-Energy Models for Phase-Stability Studies in Multicomponent Oxides*, in *Department of Materials Science and Engineering*. 1997, Massachusetts Institute of Technology: Cambridge.
13. G. Kresse and J. Furthmuller, *Comp. Mat. Sci.*, 1996. **6**: p. 15.
14. G. Kresse and J. Furthmuller, *Physical Review B*, 1996. **54**: p. 11169.
15. S.K. Mishra and G. Ceder, *Structural stability of lithium manganese oxides*. Physical Review B - Condensed Matter, 1999. **59**(9): p. 6120-6130.

CHAPTER 3

PRESCREENING OF CANDIDATE ELECTRODE MATERIALS BY FIRST PRINCIPLES METHODS

An initial search on $\text{LiNi}_{1/3}\text{TM1}_{1/3}\text{TM2}_{1/3}\text{O}_2$ where TM1 is a 3+ transition metal (Co^{3+} , Al^{3+} , Fe^{3+} etc) and TM2 is a 4+ transition metal (Ti^{4+} , Zr^{4+} , Mn^{4+} etc.) was carried out. It has been amply demonstrated that reasonable lithium intercalation potentials and geometrical information can be obtained with first principles methods [1, 2]. The relative stability of phase can also be predicted with total energy calculation. In this chapter, we will discuss the computational details of the work, demonstrating how the first principles method can act as a prescreening tool to identify potential cathode materials.

3.1 Computation Details

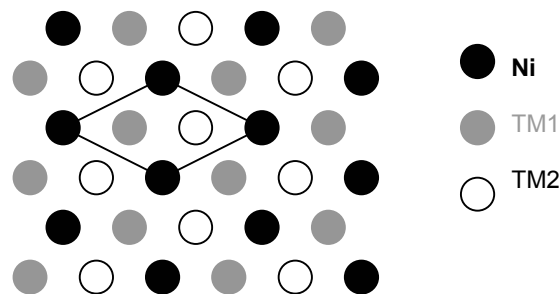


Figure 3-1 Ni, TM1 and TM2 ordering in the supercell of $\text{LiNi}_{1/3}\text{TM1}_{1/3}\text{TM2}_{1/3}\text{O}_2$

To describe the $\text{Li}_x\text{Ni}_{1/3}\text{TM1}_{1/3}\text{TM2}_{1/3}\text{O}_2$ system, supercells with three formula units were used. As most of the computation methods do, this computation approach

requires the use of periodic boundaries; Ni, TM1 and TM2 are long-range ordered on a triangular lattice of transition metal sites as shown in Figure 3-1. Partial states of de-lithiation were investigated at $x = 2/3$ and $1/3$. The number of possible arrangements for Li and vacancy sites in the supercell were 1, 3, 3 and 1 for $x=1$, $2/3$, $1/3$ and 0, respectively. All possible arrangements have been calculated.

All energies, intercalation potentials, geometries and electronic structure of materials in this work were obtained using first-principles quantum mechanics in the Generalized Gradient Approximation (GGA) to Density Functional Theory (DFT), as implemented in the Vienna Ab Initio Simulation Package (VASP). Ultra-soft pseudo-potentials are applied to represent the nuclei and core electrons and all structures are fully relaxed with respect to internal and external cell parameters. The wave functions are expanded in plane waves with energy below 405eV. Brillouin zone integration of the band structure is performed with a $6 \times 3 \times 4$ mesh. All calculations are performed with spin polarization, previously demonstrated to be crucial in manganese oxides [3]. Both ferromagnetic and anti-ferromagnetic spin polarization was taken into consideration, no qualitative difference was found in the voltage and relative formation energies calculation. Since experimentally, the materials are mostly found paramagnetic, we will not discuss the effect of magnetic configuration here.

3.2 Formation Energies

According to general alloy theory [4], a measure of the effective Ni-TM1-TM2 interactions can be obtained by comparing the energy of $\text{LiNi}_{1/3}\text{TM1}_{1/3}\text{TM2}_{1/3}\text{O}_2$ to the average energy of LiNiO_2 , LiTM1O_2 and LiTM2O_2 .

$$\Delta E_{mix}^{x=1} = E_{LiNi_{1/3}TM_{1/3}TM_{2/3}O_2} - \frac{1}{3}(E_{LiNiO_2} + E_{LiTM_1O_2} + E_{LiTM_2O_2}) \quad \text{Eq. 3-1}$$

If ΔE_{mix} is negative, Ni, TM1 and TM2 have an attractive interaction on average and the system will be either randomly mixed or ordered, depending on the synthesis temperature. If ΔE_{mix} is positive, it is energetically more favorable to phase separate into Ni, TM1 and TM2 rich regions, though random mixing can be achieved if the synthesis temperature is high enough. By calculating the relevant energies values in the above formula, it was found that all ΔE_{mix} (meV per Li) for the compounds: $LiNi_{1/3}TM_{1/3}Mn_{1/3}O_2$ (TM1 = Co, Al, Fe) and $LiNi_{1/3}Co_{1/3}TM_{2/3}O_2$ (TM2 = Mn, Ti, Zr) are negative. It implies that the synthesis of these materials is thermodynamically favorable.

For fully delithiated $Li_xNi_{1/3}TM_{1/3}TM_{2/3}O_2$, ΔE_{mix} computed by

$$\Delta E_{mix}^{x=0} = E_{Ni_{1/3}TM_{1/3}TM_{2/3}O_2} - \frac{1}{3}(E_{NiO_2} + E_{TM_1O_2} + E_{TM_2O_2}) \quad \text{Eq. 3-2}$$

is usually positive. For example, ΔE_{mix} of $Li_xNi_{1/3}Fe_{1/3}Mn_{1/3}O_2$ ($x = 0$), is calculated to be +34meV per formula unit. To remove the last one-third of lithium, one not only has to supply the binding energy of the lithium ion and electron, but also the strong energy raise in the system due to the unfavorable $Ni^{VI} - Fe^{VI} - Mn^{VI}$ interaction.

The relative formation energy E_{RF} for a given lithium-vacancy arrangement with lithium concentration in $Li_xNi_{1/3}TM_{1/3}TM_{2/3}O_2$, is defined as

$$\Delta E_{RF} = E_{Li_xNi_{1/3}Fe_{1/3}Mn_{1/3}O_2} - xE_{LiNi_{1/3}Fe_{1/3}Mn_{1/3}O_2} - (1-x)E_{Ni_{1/3}Fe_{1/3}Mn_{1/3}O_2} \quad \text{Eq. 3-3}$$

Relative formation energy more conveniently displays relative stability between different phases. The relative formation energies for $\text{Li}_x\text{Ni}_{1/3}\text{Fe}_{1/3}\text{Mn}_{1/3}\text{O}_2$ are negative, as shown in Figure 3-2. It can be seen that at $x = 1/2$, the Li-vacancy arrangement lies on the convex hull, which indicates $\text{Li}_{1/2}\text{Ni}_{1/3}\text{Fe}_{1/3}\text{Mn}_{1/3}\text{O}_2$ will not phase separate into a two-phase mixture of $\text{LiNi}_{1/3}\text{Fe}_{1/3}\text{Mn}_{1/3}\text{O}_2$ and $\text{Ni}_{1/3}\text{Fe}_{1/3}\text{Mn}_{1/3}\text{O}_2$.

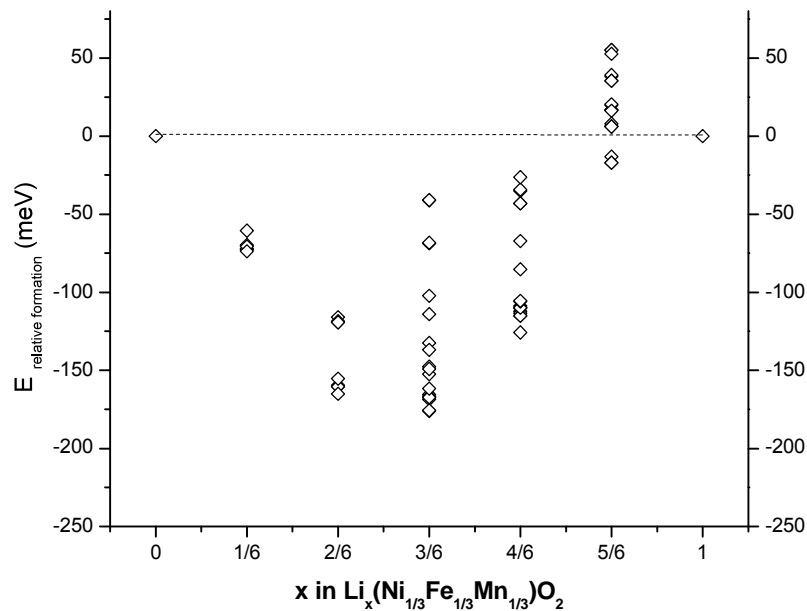


Figure 3-2 Relative formation energy (E_{RF}) of $\text{Li}_x\text{Ni}_{1/3}\text{Fe}_{1/3}\text{Mn}_{1/3}\text{O}_2$ calculated with antiferromagnetic coupling in a supercell of six formula units.

3.3 Voltages

Measuring the cell voltage at equilibrium versus charge passed between the electrodes is equivalent to measuring the chemical potential as a function of x in the lithium intercalation compound. This simple fact derived from the Nernst equation [5] can be written as

$$V(x) = -\frac{(\mu_{Li}^{cathode} - \mu_{Li}^{anode})}{ze} \quad \text{Eq. 3 - 4}$$

where μ_{Li}^{anode} is constant if metallic lithium is used as anode;

According to the thermodynamics of intercalation compounds, the Gibbs free energy G changes with the concentration x of intercalated Li. The chemical potential is simply the slope of G_f with respect to x ,

$$\mu_{Li}^{cathode} = \left(\frac{\partial G_f}{\partial x} \right)_{T,P,N_{host}} \quad \text{Eq. 3 - 5}$$

In this work, G_f is approximated by E (total energy) because electronic, vibrational and configurationally excitations are not considered.

Figure 3-3 shows the potential of some of the possible compounds as average voltages over intervals of 1/3 Li composition. The stepwise nature of the curves is therefore artificial and due to the averaging of the potential over the specific composition interval. The effect of disorder, present in a real system, would likely smooth the voltage curve from what is achieved computationally.

Previously in section 1.3.4, we have mentioned that a multi-cation compound $\text{LiNi}_{1/3}\text{Co}_{1/3}\text{Mn}_{1/3}\text{O}_2$ is a promising cathode material. Nevertheless first principles calculation and experimental studies [6, 7] reveal that Co^{3+} is only oxidized to Co^{4+} at rather high voltage (about 5V), where normal electrolyte tends to break down. in this material. If we can find an intercalation compound, by substituting Mn^{4+} with other 4+ transition metal ions; or by replacing $\text{Co}^{3+}/\text{Co}^{4+}$ redox couple by another

redox couple which will be active in the operation voltage window 3.0-4.5V, we can achieve higher specific capacity (mAh/g) in the fixed voltage range.

As it can be clearly seen in Figure 3-3, if the calculated voltage of $\text{LiNi}_{1/3}\text{Co}_{1/3}\text{Mn}_{1/3}\text{O}_2$ is regarded as the reference point, substitution of Mn by either Ti or Zr clearly increases the average potential. It needs to be point out that the GGA calculations tend to under-predict the voltages in layered transition metal oxides, which as been amply demonstrated [8]. The potential difference between the calculated and experimental voltages is suggested to be about 0.7-0.8V.[9] The self-interaction in GGA tends to delocalize electrons too much, and as such the first principles methods are unable to capture precisely the Coulomb correlation effects in correlated electron systems like transition metal oxides. The problem has recently been highlighted and fixed by Zhou et al. [10, 11] with the implantation of GGA+U method.

In agreement with previous work on Al-doping [2], substitution of Co by Al increases the potential. As it can not be easily oxidized beyond 3+, Al doping is expected to reduce the capacity at the end of charge. Of all the compositional modifications investigated, Fe substitution of Co seems to be advantageous since it lowers the voltage profile at the last stage of the charge, compared to $\text{LiNi}_{1/3}\text{Co}_{1/3}\text{Mn}_{1/3}\text{O}_2$, whose capacity in the voltage range 3.0 – 4.5V is limited by higher voltage of $\text{Co}^{3+}/\text{Co}^{4+}$ redox couple. Hence, the specific capacity of $\text{LiNi}_{1/3}\text{Fe}_{1/3}\text{Mn}_{1/3}\text{O}_2$ could be higher in the potential window of 3.0-4.5V.

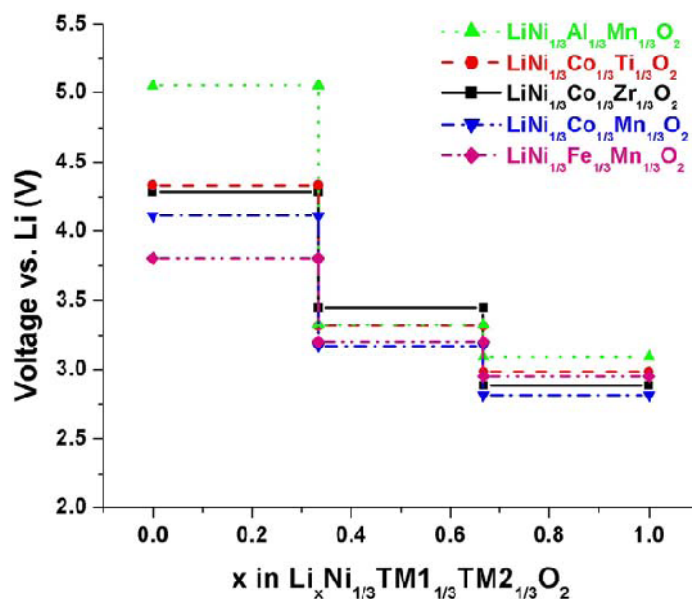


Figure 3-3 Calculated voltage curves for $\text{LiNi}_{1/3}\text{TM1}_{1/3}\text{TM2}_{1/3}\text{O}_2$ where $\text{TM1} = \text{Al}^{3+}, \text{Co}^{3+}$ or Fe^{3+} and $\text{TM2} = \text{Mn}^{4+}, \text{Ti}^{4+}$ or Zr^{4+}

Here we have demonstrated that with the first principles computation as a prescreening tool, we identified the Fe substituted nickel manganese oxide could deliver higher specific capacity in the practical voltage range compared with other compounds in $\text{LiNi}_{1/3}\text{TM1}_{1/3}\text{Mn}_{1/3}$ system, therefore could be a potential candidate for cathode material in lithium ion battery. The detailed analysis of the effect of cation substitution on Li intercalation voltages will be presented in chapter 5.

3.4 Material of the Choice

Concerning iron substitution, numerous works have been carried out in lithium nickel-iron oxides [12-14]. In those work the presence of iron ions does not suppress the disordering in the structure and degrades the cell capacity compared to LiNiO_2 . According to a review by Delmas [15], the small difference in size between lithium

ions and the substituting atom leads to its preferential occupancy on the lithium site in a layered structure. The size of Fe^{3+} (0.65 Å) ion is comparable to those of Ni^{2+} (0.69 Å) and Li^+ (0.70 Å), though in all previous works, Ni ions shall be in the oxidation state of Ni^{3+} for perfect stoichiometric compound, though small amount of Ni^{2+} is always found in the pristine material. It is well known that due to the similar ion size of Fe^{3+} and Li^+ , the Fe can partially occupy the Li-layer [12-14]. In addition, unlike LiCoO_2 and LiNiO_2 , the LiFeO_2 ground-state structure is not layered, but a structure with symmetry $I4_1/amd$ [15]. According to our preliminary mixing enthalpy calculations using the equation below, the relative formation energy of $\text{LiNi}_{1/3}\text{Fe}_{1/3}\text{Mn}_{1/3}\text{O}_2$ with respect to $\text{LiNi}_{1/2}\text{Mn}_{1/2}\text{O}_2$ and LiFeO_2 is approximately zero, indicating that only a weak entropic driving force for mixing might exist in a compound where Co is fully substituted by Fe.

$$\Delta E_{mix} = E_{\text{LiNi}_{1/3}\text{Fe}_{1/3}\text{Co}_{1/3-z}\text{Mn}_{1/3}\text{O}_2} - \left[\frac{2}{3} E_{\text{LiNi}_{1/2}\text{Mn}_{1/2}\text{O}_2} + z E_{\text{LiFeO}_2} + \left(\frac{1}{3} - z \right) E_{\text{LiCoO}_2} \right] \quad \text{Eq. 3 - 6}$$

Therefore, in first principles computation we chose to substitute Co only partially by Fe and targeted the nominal composition $\text{LiNi}_{1/3}\text{Fe}_{1/6}\text{Co}_{1/6}\text{Mn}_{1/3}\text{O}_2$ in order to have reasonable supercell size.

To describe the $\text{Li}_x\text{Ni}_{1/3}\text{Fe}_{1/6}\text{Co}_{1/6}\text{Mn}_{1/3}\text{O}_2$ system, supercells with six formula units were used. As it is typical in solid state computations periodic boundaries are used, so that one effectively models a system with Ni, Fe Co and Mn long-range ordered (Figure 4). Partial states of delithiation were investigated at $x = 5/6, 2/3, 1/2, 1/3$ and $1/6$. The number of possible arrangements for Li and vacancy sites in the supercell were 1, 6, 15, 20, 15, 6 and 1 for $x = 1, 5/6, 2/3, 1/2, 1/3, 1/6$ and 0, respectively. All possible arrangements have been calculated.

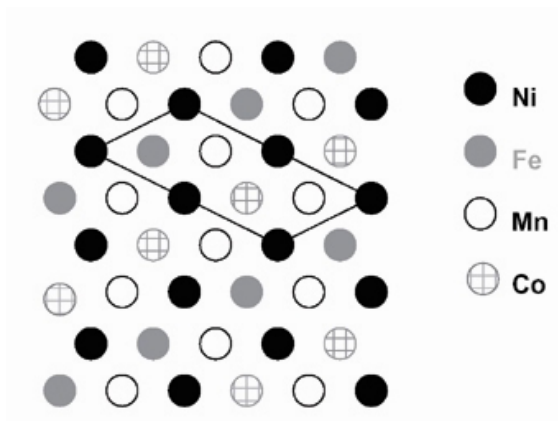


Figure 3-4. Ni, Fe, Co Mn ordering in the supercell of $\text{Li}(\text{Ni}_{1/3}\text{Fe}_{1/6}\text{Co}_{1/6}\text{Mn}_{1/3})\text{O}_2$.

3.4.1 Intercalation Voltage

Average voltage profiles for $\text{Li}_x\text{Ni}_{1/3}\text{Fe}_{1/6}\text{Co}_{1/6}\text{Mn}_{1/3}\text{O}_2$ ($0 \leq x \leq 1$) were computed from the lowest energy lithium-vacancy arrangements in the six-formula supercell as function of lithium compositions. The calculated potentials are typically lower than experimental values, as is usually the case in standard first principles energy methods [8, 9]. The calculated intercalation voltage of $\text{Li}_x\text{Ni}_{1/3}\text{Fe}_{1/6}\text{Co}_{1/6}\text{Mn}_{1/3}\text{O}_2$ is compared to that of $\text{Li}_x\text{Ni}_{1/3}\text{Co}_{1/3}\text{Mn}_{1/3}\text{O}_2$ in Figure 3-5. In the range $1/3 \leq x \leq 1$, a calculated average voltage of 3.0-3.1V is obtained for $\text{Li}_x\text{Ni}_{1/3}\text{Fe}_{1/6}\text{Co}_{1/6}\text{Mn}_{1/3}\text{O}_2$. The potential increases significantly to 3.8-3.9V in the range $0 \leq x \leq 1/3$. Compared to $\text{Li}_x\text{Ni}_{1/3}\text{Co}_{1/3}\text{Mn}_{1/3}\text{O}_2$ [7], (shown by the solid line in Figure 3-5) the substitution of Fe with Co increases the average voltage slightly for $1/2 \leq x \leq 1$. Most importantly, in the Fe substituted compound, the calculated voltage at the end of charge ($0 \leq x \leq 1/3$) is much lower than that of $\text{Li}_x\text{Ni}_{1/3}\text{Co}_{1/3}\text{Mn}_{1/3}\text{O}_2$. These results indicate that Fe substitution of Co in $\text{LiNi}_{1/3}\text{Fe}_z\text{Co}_{1/3-z}\text{Mn}_{1/3}\text{O}_2$ may flatten the voltage curve and increase the experimentally attainable capacity by lowering the potential near the end of charge.

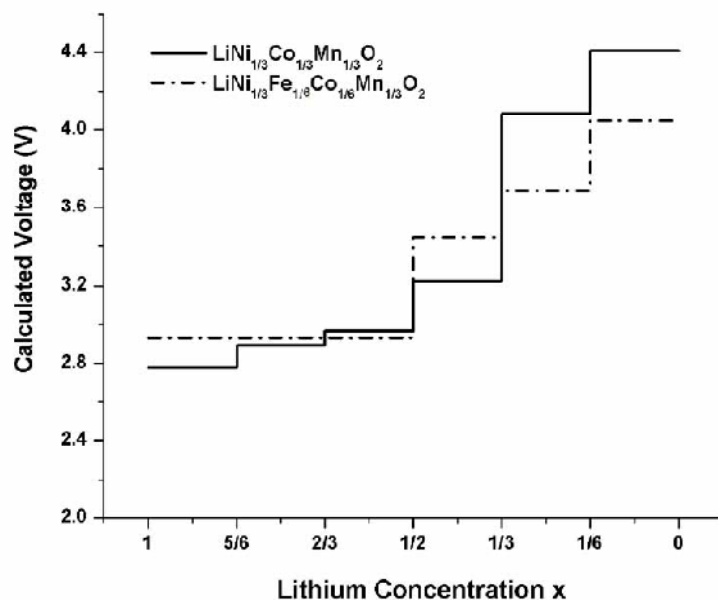


Figure 3-5. Comparison of calculated average voltage curves of $\text{Li}_x\text{Ni}_{1/3}\text{Co}_{1/3}\text{Mn}_{1/3}\text{O}_2$ and $\text{Li}_x\text{Ni}_{1/3}\text{Fe}_{1/6}\text{Co}_{1/6}\text{Mn}_{1/3}\text{O}_2$.

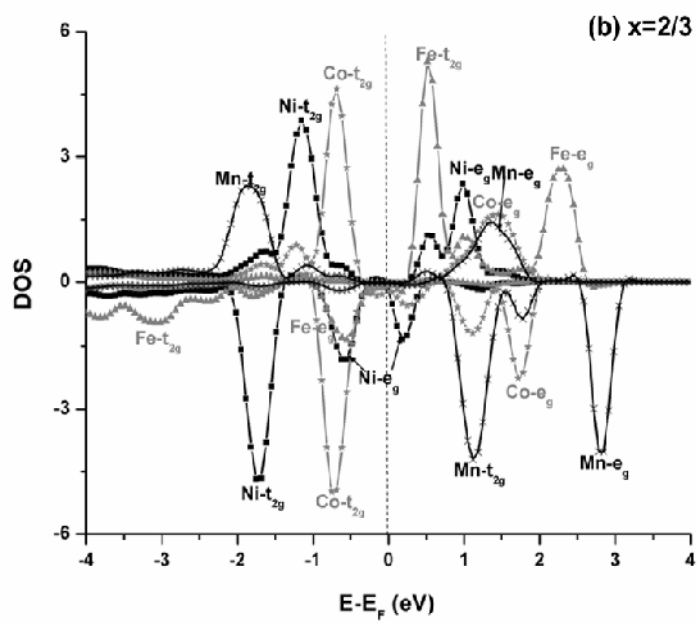
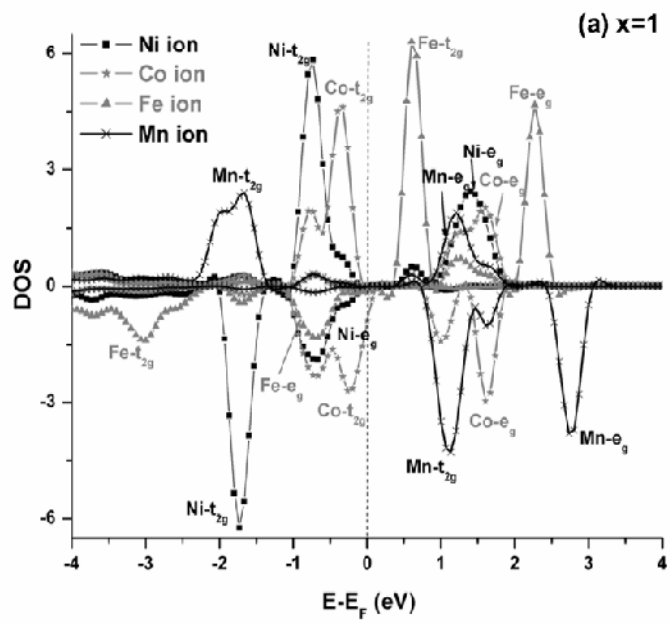
3.4.2 Electronic Change during Charge-Discharge

To understand the electronic changes in $\text{LiNi}_{1/3}\text{Fe}_{1/6}\text{Co}_{1/6}\text{Mn}_{1/3}\text{O}_2$ when lithium is removed, the spin polarized density of states (DOS) at different lithium concentrations is shown in Figure 3-6. Since the transition metal ions occupy the octahedral sites in the sublattices of oxygen ions, $3d$ bands of transition metal ions split into t_{2g} and e_g bands. The calculated DOS, projected onto the orbitals of each transition metal are shown in Figure 3-6.

For all lithium compositions, the Mn- t_{2g} and Mn- e_g bands are respectively, half filled and empty in $\text{Li}_x\text{Ni}_{1/3}\text{Fe}_{1/6}\text{Co}_{1/6}\text{Mn}_{1/3}\text{O}_2$ ($0 \leq x \leq 1$), which is consistent with a Mn^{4+} valence state. For fully lithiated $\text{LiNi}_{1/3}\text{Fe}_{1/6}\text{Co}_{1/6}\text{Mn}_{1/3}\text{O}_2$ ($x = 1$ in Figure 3-6a), Ni- t_{2g} states are fully occupied and only one spin direction for the Ni- e_g states is

occupied. For Fe- t_{2g} and Fe- e_g only the majority spin states are occupied indicating high-spin Fe^{3+} . The Co- t_{2g} states are fully occupied and Co- e_g states are empty, indicative of Co^{3+} . The Fermi level, E_F is located between the top of occupied Co- t_{2g} bands and unoccupied Fe- t_{2g} states. There is an energy gap of about 0.3 eV between the unoccupied and occupied states. Although it is well known that the calculated energy gaps in GGA are typically smaller than the experimental values, the comparison with the calculated energy gap for $LiNi_{1/3}Co_{1/3}Mn_{1/3}O_2$ (0.7V) [7] indicates that the electronic conductivity of $LiNi_{1/3}Fe_{1/6}Co_{1/6}Mn_{1/3}O_2$ may be as good, if not better, as $LiNi_{1/3}Co_{1/3}Mn_{1/3}O_2$.

As we applied a supercell with six-formula units in this study, both Ni^{2+}/Ni^{3+} and Ni^{2+}/Ni^{4+} are possible redox reactions. Figure 3-6a) & b) show that for a partially delithiated state ($2/3 \leq x \leq 1$), only the Ni^{2+}/Ni^{3+} redox reaction is observed, which is consistent with the previous studies on $LiNi_{1/2}Mn_{1/2}O_2$ and $LiNi_{1/3}Co_{1/3}Mn_{1/3}O_2$. [7, 8, 16] At $x = 2/3$ (Figure 3-6b)), there is an overlap between filled Ni- e_g and Fe- e_g states, indicating very similar redox potentials for Ni and Fe ions. Electrons are simultaneously removed from the Ni- e_g and Fe- e_g bands upon further delithiation as shown in Figure 3-6c). It clearly indicates that the Ni^{3+}/Ni^{4+} and Fe^{3+}/Fe^{4+} redox reactions take place simultaneously. Such simultaneous redox reactions of Fe and Ni have been reported in the $Li(Ni,Fe)O_2$ system by ^{57}Fe Mossbauer and EXAFS investigations. [17, 18] Furthermore, upon delithiation ($1/3 \leq x \leq 2/3$), the Fe- e_g states become empty and all four valence electrons partially fill Fe- t_{2g} states indicating low-spin for Fe^{4+} . At $x = 0$, an electron is also pulled from the Co- t_{2g} band (Figure 3-6d)), which demonstrates that the redox couple Co^{3+}/Co^{4+} is activated at the end of charge.



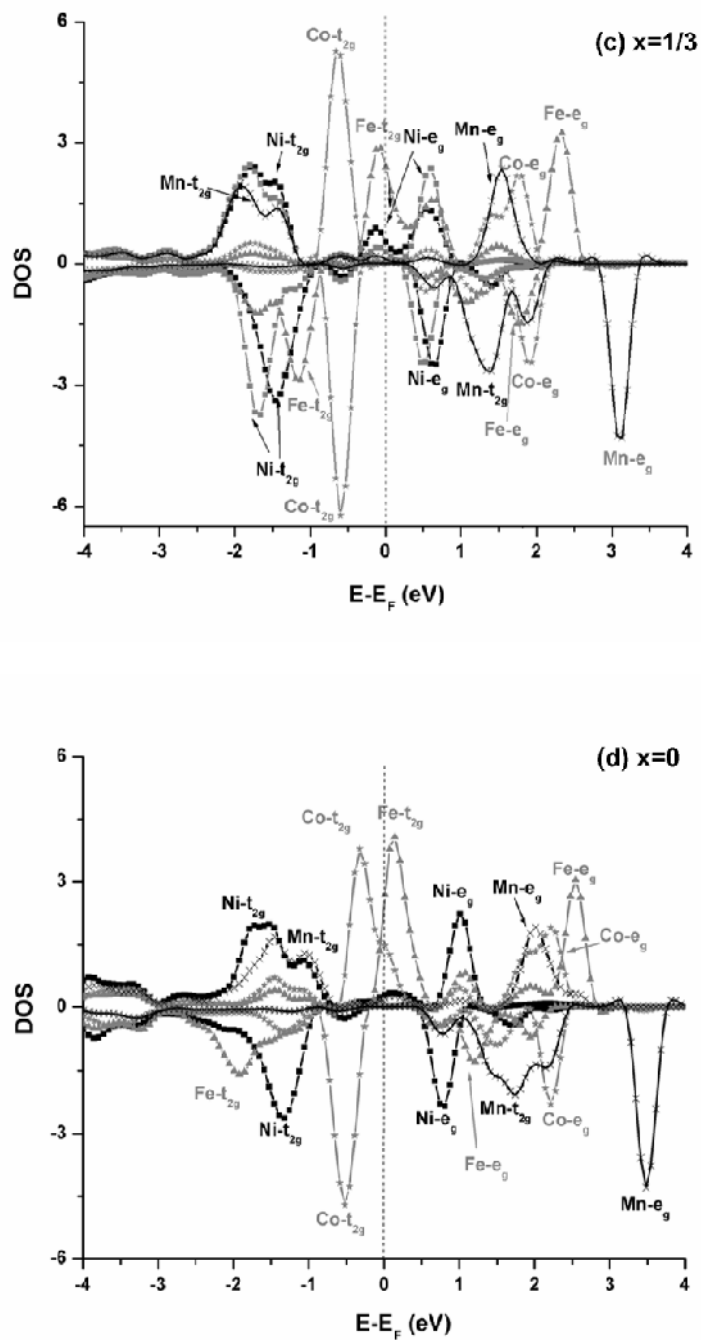


Figure 3-6 Calculated density of states of $\text{Li}_x\text{Ni}_{1/3}\text{Fe}_{1/6}\text{Co}_{1/6}\text{Mn}_{1/3}\text{O}_2$ at a) $x=1$, b) $x=2/3$, c) $x=1/3$, and d) $x=0$.

3.4.3 Lattice Parameters and Bond Lengths

Table 3-I show the calculated lattice parameters and bond distances of $\text{Li}_x\text{Ni}_{1/3}\text{Co}_{1/3}\text{Fe}_{1/6}\text{Mn}_{1/3}\text{O}_2$ at various lithium concentrations. The structural parameters of the most stable states were selected. There is no significant difference in the structural parameters among different Li-vacancy configurations at the same composition.

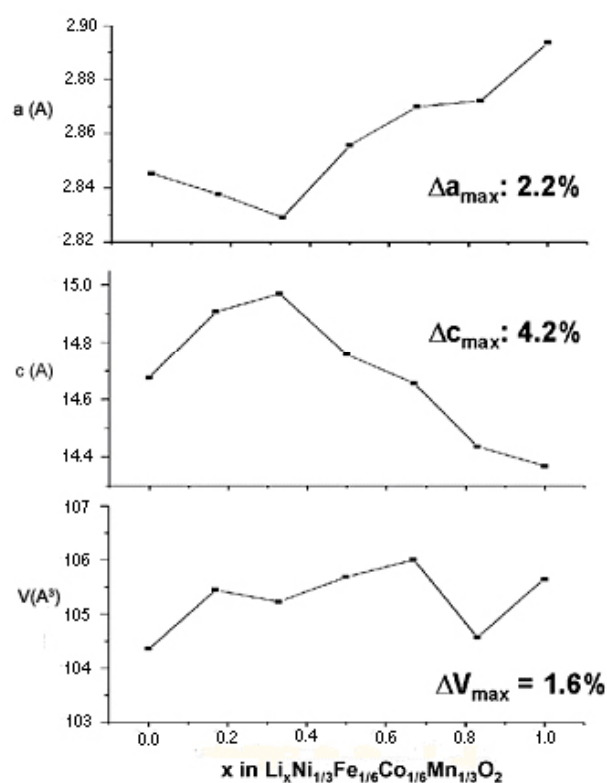


Figure 3-7 Calculated lattice parameter a & c and volume at various lithium concentrations.

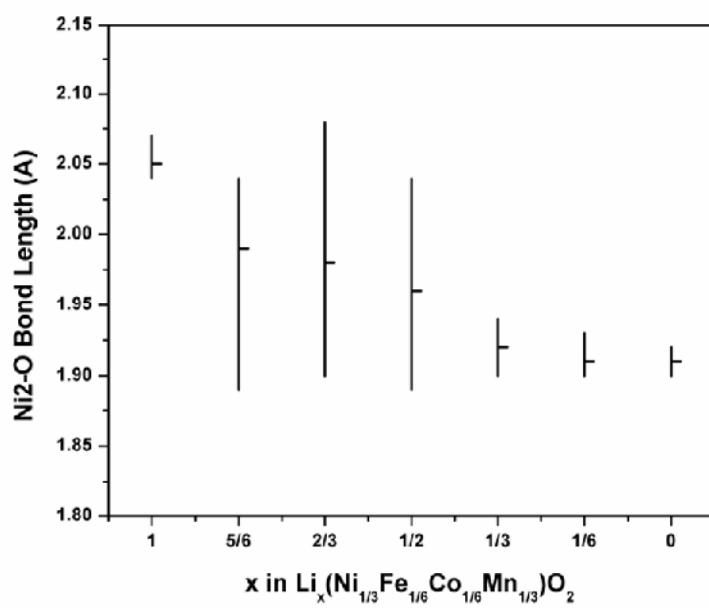
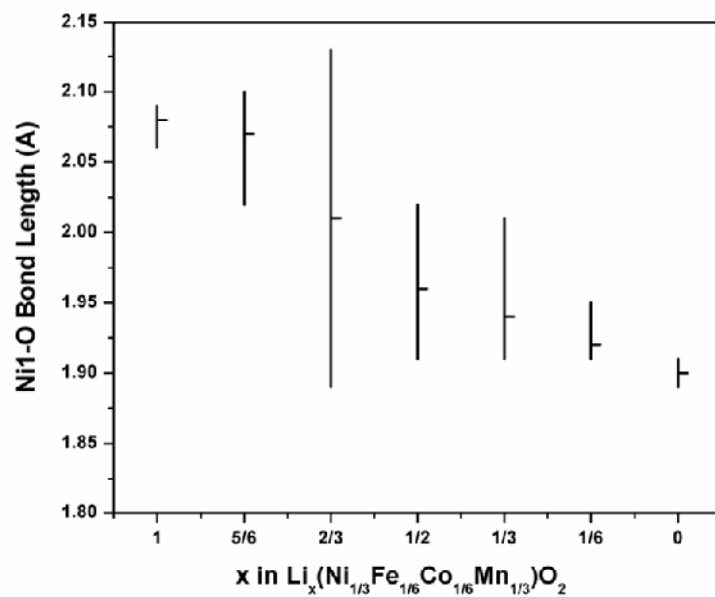
The calculated lattice parameters a & c of $\text{Li}_x\text{Ni}_{1/3}\text{Co}_{1/6}\text{Fe}_{1/6}\text{Mn}_{1/3}\text{O}_2$ at various lithium concentrations are depicted in Figure 3-7. The calculated a lattice parameter decreases in the range of $1/3 \leq x \leq 1$ by approximately 2.2% and increases slightly in

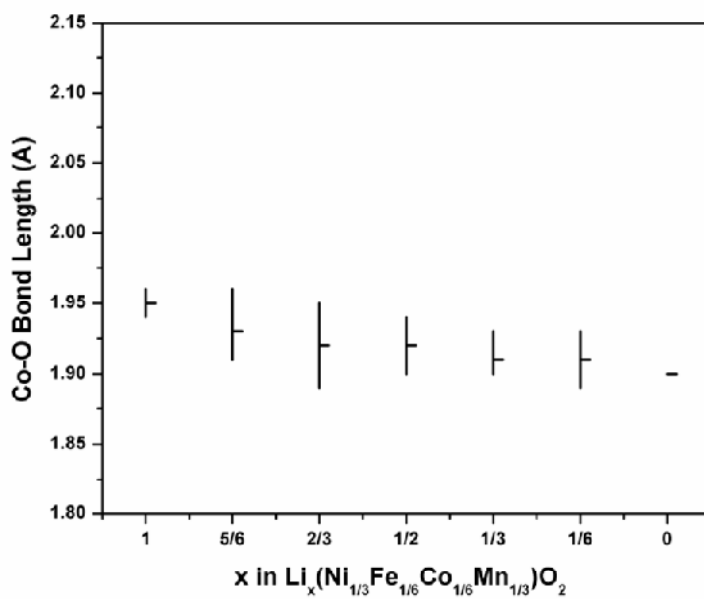
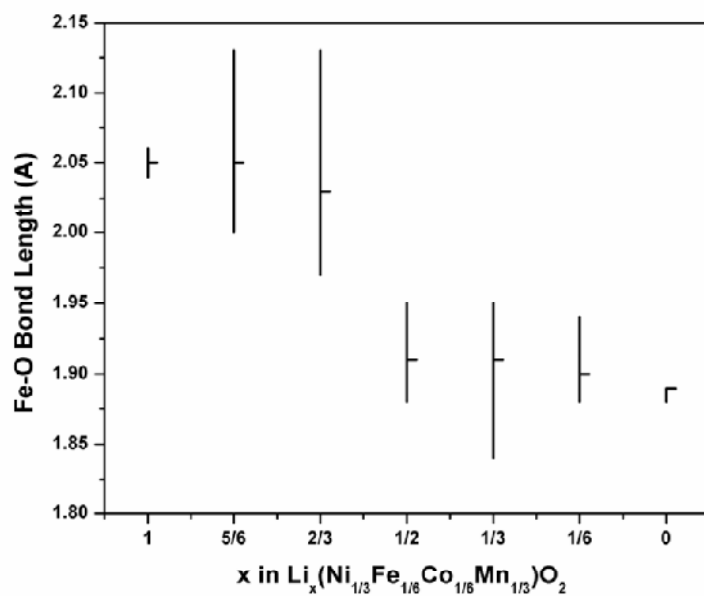
the range of $0 \leq x \leq 1/3$. The lattice parameter c increases by about 4.2% in the range of $1/3 \leq x \leq 1$ and decreases for $0 \leq x \leq 1/3$. The maximum change in cell volume is only 1.6%, which implies that effect of stress and strain in the material during the lithiation – delithiation cycle will be very small; in comparison the volume change of LiCoO_2 is about 3 to 4 percent [19].

The bond distances between the transition metal ions and oxygen ions at different lithium contents are also shown in Table 3-I. The average bond distances between the transition metal ions and oxygen ions at different lithium contents are plotted in Figure 3-8. The bond distances of Ni-O and Mn-O in fully-lithiated $\text{Li}_x\text{Ni}_{1/3}\text{Fe}_{1/6}\text{Co}_{1/6}\text{Mn}_{1/3}\text{O}_2$ material ($x = 1$) are $[2 \times 2.04 \ 2.05 \ 2 \times 2.06 \ 2.07] \text{ \AA}$, $[2.06 \ 2.07 \ 2.08 \ 3 \times 2.09] \text{ \AA}$ and $[1.93 \ 4 \times 1.94 \ 1.95] \text{ \AA}$, $[3 \times 1.93 \ 1.94 \ 2 \times 1.95] \text{ \AA}$, respectively. The bond distance of Ni-O is much longer than that of Mn-O, indicating Ni has oxidation state of 2+ in this material. Fe-O has similar bond distances as Ni-O $[2.04 \ 4 \times 2.05 \ 2.06] \text{ \AA}$, which can be explained by the similar size of Fe^{3+} and Ni^{2+} [Shannon radius] [20]. Co-O has the typical bond distance of Co^{3+} in the layered compound [21].

As lithium is removed, in the range of $2/3 \leq x \leq 1$, Ni^{2+} is oxidized and the bond distances of Ni-O become shorter. The large spread of bond lengths for Ni-O in this range is due to Jahn-Teller distortion of $\text{Ni}^{\text{III}}\text{O}_6$ octahedron. Note that this also affects the Fe-O and Mn-O bond lengths. Such distortion disappears upon further lithium removal: in the range of $1/3 \leq x \leq 2/3$, the Fe-O (Figure 3-8c)) and Ni-O (Figure 3-8a) & b)) bond distances reduce simultaneously, which is in good

agreement with the DOS observations in Figure 3-6. In addition, in this range ($1/3 \leq x \leq 2/3$) the decrease in Fe-O bonds distance changes the crystal field splitting between the e_g and t_{2g} bands [22], which leads to low-spin of Fe^{4+} , as mentioned previously.





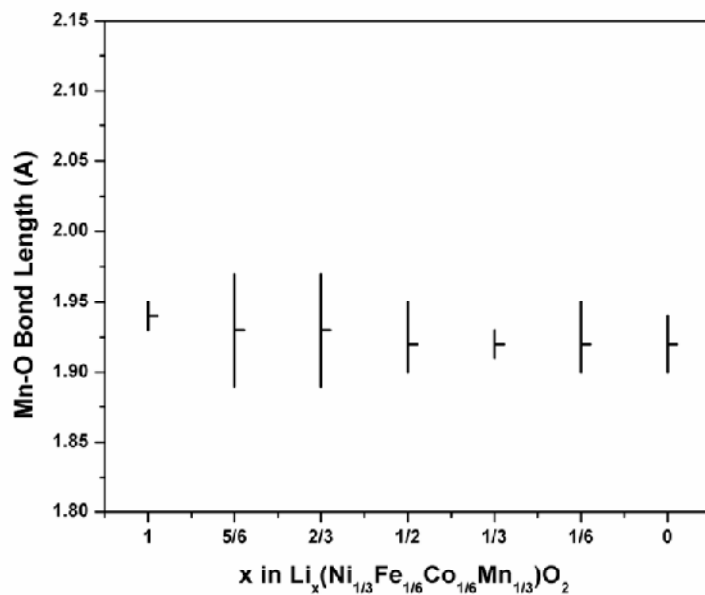


Figure 3-8. Calculated transition metal - oxygen bond lengths (TM-O distances) of $\text{Li}_x\text{Ni}_{1/3}\text{Fe}_{1/6}\text{Co}_{1/6}\text{Mn}_{1/3}\text{O}_2$ ($0 \leq x \leq 1$)

Table 3-1 Calculated lattice parameters and transition metal –oxygen bond distances of $\text{Li}_x\text{Ni}_{1/3}\text{Co}_{1/6}\text{Fe}_{1/6}\text{Mn}_{1/3}\text{O}_2$

$\text{Li}_x\text{Ni}_{1/3}\text{Co}_{1/6}\text{Fe}_{1/6}\text{Mn}_{1/3}\text{O}_2$	1	5/6	2/3	1/2	1/3	1/6	0
a (Å)	2.9138	2.8922	2.8901	2.8758	2.8490	2.8578	2.8653
c (Å)	14.3690	14.4359	14.6552	14.7569	14.9709	14.9086	14.6775
Ni-O (Å)	2×2.04 2.05 2×2.06 2.07	2.02 2×2.06 2.09 2×2.10	1.90 1.91 1.96 1.97 2.07 2.08	1.91 1.93 1.95 1.96 2.01 2.02	2×1.91 1.92 1.93 1.97 2.01	5×1.91 1.95	2×1.89 4×1.91
Co-O (Å)	2.06 2.07 2.08 3×2.09	1.89 1.91 2.02 2.03 2×2.04	1.89 1.91 1.99 2.03 2.08 2.13	1.89 1.91 2×1.94 2.03 2.04	2×1.90 1.91 1.93 2×1.94	2×1.90 1.91 2×1.92 1.93	4×1.90 2×1.92
Fe-O (Å)	2×1.94 3×1.95 1.96	1.91 2×1.92 1.94 1.95 1.96	1.89 1.90 3×1.93 1.95	2×1.90 1.91 1.92 1.93 1.94	3×1.90 1.91 1.92 1.93	2×1.89 1.90 2×1.91 1.93	6×1.90
Mn-O (Å)	2.04 4×2.05 2.06	2×2.00 2.03 2.04 2.09 2.13	1.97 1.98 2.03 2.04 2.05 2.14	1.88 1.89 2×1.91 1.92 1.95	1.84 1.89 1.91 1.93 2×1.95	1.88 3×1.89 1.90 1.94	1.88 5×1.89
	1.93 4×1.94 1.95	1.89 1.90 1.92 1.95 1.96 1.97	1.89 1.91 1.93 2×1.95 1.97	1.91 1.92 3×1.93 1.95	1.91 2×1.92 3×1.93 1.95	2×1.90 2×1.92 1.94 1.95	2×1.90 2×1.91 1.93 1.94
	3×1.95 1.94 2×1.95	2×1.89 2×1.94 2×1.96	1.86 1.91 1.92 1.95 2×1.96	2×1.90 2×1.92 1.93 1.95	1.90 2×1.92 1.93 2×1.94	1.89 1.91 2×1.92 1.93 1.94	2×1.90 2×1.92 2×1.93

3.5 Conclusions

Prescreening with Density Functional Theory to sort through potential cathode materials based on their Li intercalation potentials and electronic structures was carried on $\text{LiNi}_{1/3}\text{TM1}_{1/3}\text{TM2}_{1/3}\text{O}_2$ systems, where TM1 is a 3+ transition metal (Co^{3+} , Al^{3+} , Fe^{3+} etc.) and TM2 is a 4+ transition metal (Ti^{4+} , Zr^{4+} , Mn^{4+} etc.). Fe substitution is found to be advantageous because among the compounds investigated it shows the lowest voltage at the last stage of the charge. The structural and electronic changes of $\text{LiNi}_{1/3}\text{Fe}_{1/6}\text{Co}_{1/6}\text{Mn}_{1/3}\text{O}_2$ with various lithium concentrations were investigated by first principles methods. Fe/Co substituted lithium nickel manganese oxides can be considered as potential cathode materials and their synthesis and characterization will be presented in the next chapter.

References:

1. C. Wolverton and A. Zunger, *Prediction of Li intercalation and battery voltages in layered vs. Cubic Li_xCoO_2* . J. Electrochem. Soc., 1998. **145**(7): p. 2424-2431.
2. G. Ceder, et al., *Identification of cathode materials for lithium batteries guided by first-principles calculations*. Nature, 1998. **392**: p. 694-666.
3. S.K. Mishra and G. Ceder, *Structural stability of lithium manganese oxides*. Physical Review B - Condensed Matter, 1999. **59**(9): p. 6120-6130.
4. D. deFontaine, in *Solid State Physics*, E.H.T. D., Editor. 1994, Academic Press: New York.
5. A.J. Bard and L.R. Faulkner, *Electrochemical Methods: Fundamentals and Applications*. 2001, New York: John Wiley & Sons, Inc.
6. K.M. Shaju, G.V.S. Rao, and B.V.R. Chowdari, *Performance of layered $\text{Li}(\text{Ni}_{1/3}\text{Co}_{1/3}\text{Mn}_{1/3})\text{O}_2$ as cathode for Li-ion batteries*. Electrochimica Acta, 2002. **48**(2): p. 145-151.
7. Hwang, B.J., et al., *A combined computational/experimental study on $\text{LiNi}_{1/3}\text{Co}_{1/3}\text{Mn}_{1/3}\text{O}_2$* . Chemistry of Materials, 2003. **15**(19): p. 3676-3682.
8. J. Reed and G. Ceder, *Charge, potential, and phase stability of layered $\text{Li}(\text{Ni}_{0.5}\text{Mn}_{0.5})\text{O}_2$* . Electrochemical and Solid State Letters, 2002. **5**(7): p. A145-A148.
9. M.K. Aydinol, et al., *Ab initio study of lithium intercalation in metal oxides and metal dichalcogenides*. Physical Review B, 1997. **56**(3): p. 1354-1365.
10. F. Zhou, et al., *Phase separation in Li_xFePO_4 induced by correlation effects*. Physical Review B, 2004. **69**(20).
11. F. Zhou, et al., *The electronic structure and band gap of LiFePO_4 and LiMnPO_4* . Solid State Communications, 2004. **132**: p. 181-186.
12. J.N. Reimers, et al., *Structure and electrochemistry of $\text{Li}_x\text{Fe}_y\text{Ni}_{1-y}\text{O}_2$* . Solid State Ionics, 1993. **61**: p. 335-344.
13. R. Kanno, et al., *Synthesis and electrochemical properties of lithium iron oxides with layer-related structures*. Journal of Power Sources, 1997. **68**(1): p. 145-152.
14. G. Prado, et al., *Electrochemical behaviour of iron substituted lithium nickelate*. J. Electrochem. Soc., 2000. **147**(8): p. 2880.
15. C. Delmas, et al., *An overview of the $\text{Li}(\text{Ni},\text{M})\text{O}_2$ systems : syntheses, structures and properties*. Electrochimica Acta, 1999. **45**: p. 243-253.
16. Arachi, Y., et al., *Structural change of $\text{Li}_{1-x}\text{Ni}_{0.5}\text{Mn}_{0.5}\text{O}_2$ cathode materials for lithium-ion batteries by synchrotron radiation*. Chemistry Letters, 2003. **32**(1): p. 60-61.
17. A. Demourgues, *(Fe,Co,Ni) K-edge EXAFS study of $\text{Li}_x(\text{Ni}_{1-y}\text{M}_y)\text{O}_2$ ($M = \text{Fe}, \text{Co}$) phases : effect of the lithium content and the cation substitution on the Ni(III) Jahn-Teller distortion*. in *Lithium Batterie Discussion*. 2001. Arcachon.
18. G. Prado, L. Fournès, and C. Delmas, *On the $\text{Li}_x\text{Ni}_{0.70}\text{Fe}_{0.15}\text{Co}_{0.15}\text{O}_2$ cathode material*. Journal of Solid State Chemistry, 2001. **159**: p. 103.
19. T. Ohzuku and A. Ueda, *Solid-state redox reactions of LiCoO_2 (R-3m) for 4 volt secondary lithium cells*. J. Electrochem. Soc., 1994. **141**(11): p. 2972-2977.
20. R.D. Shannon and C.T. Prewitt, *Revised Effective Ionic Radii in Halides and Chalcogenides*, Acta Crystallographica, 1969. **B25**: p. 925.

21. Y. Koyama, et al., *Crystal and electronic structures of superstructural $Li_{1-x}Co_{1/3}Ni_{1/3}Mn_{1/3}O_2$ ($0 \leq x \leq 1$)*. *Journal of Power Sources*, 2003. **119**: p. 644-648.
22. B.N. Figgis and M.A. Hitchman, *Ligand Field Theory and Its Applications*. 2000, New York: Wiley-VCH.

CHAPTER 4

SYNTHESIS, CHARACTERIZATION & ELECTROCHEMICAL TESTING OF FE/CO SUBSTITUTED LITHIUM NICKEL MANGANESE OXIDES

As demonstrated in the previous chapter, Fe substitution in the $\text{LiNi}_{1/3}\text{TMI}_{1/3}\text{Mn}_{1/3}\text{O}_2$ system ($\text{TMI} = \text{Co}^{3+}, \text{Fe}^{3+}, \text{Al}^{3+}$ etc) is found to be advantageous because it has a relatively low voltage according to the first principles study, which means possibly higher accessible capacity in the practical voltage range. Motivated by the first principles computation based on Density Functional Theory, experimental studies of the system $\text{LiNi}_{1/3}\text{Fe}_z\text{Co}_{1/3-z}\text{Mn}_{1/3}\text{O}_2$ were carried out. In this chapter, we will show how these potential cathode materials were synthesized, characterized and optimized with the guidance of first principles method. Experimental results on their Li intercalation voltages, crystal structures and electronic structures will be compared with the computationally predicted values. We hope to demonstrate that the direct integration of first principles computation with various experimental techniques helps to shorten the development cycle of the cathode material in lithium ion batteries.

4.1 Guided Synthesis

It is well-known that due to the similar ion size of Fe^{3+} and Li^+ , the Fe can partially occupy Li sites in the Li layer [1, 2]. In addition, unlike LiCoO_2 and LiNiO_2 , the

LiFeO₂ ground state structure is a rocksalt structure with space group I4₁/amd [3]. According to the preliminary mixing enthalpy calculations using the equation below, the relative formation energy of LiNi_{1/3}Fe_{1/3}Mn_{1/3}O₂ with respect to LiNi_{1/2}Mn_{1/2}O₂ and LiFeO₂ is approximately zero, indicating that only a weak entropic driving force for mixing might exist in a compound where Co is fully substituted by Fe.

$$\Delta E_{mix} = E_{LiNi_{1/3}Fe_zCo_{1/3-z}Mn_{1/3}O_2} - \left[\frac{2}{3} E_{LiNi_{1/2}Mn_{1/2}O_2} + zE_{LiFeO_2} + \left(\frac{1}{3} - z \right) E_{LiCoO_2} \right] \quad \text{Eq. 4-1}$$

Therefore, we chose to substitute Co only partially by Fe and targeted the nominal composition range LiNi_{1/3}Fe_zCo_{1/3-z}Mn_{1/3}O₂ (0 ≤ z ≤ 1/3) in order to obtain the composition limit by which a pure single-phase layered material.

LiNi_{1/3}Fe_zCo_{1/3-z}Mn_{1/3}O₂ (0 ≤ z ≤ 1/3) cathode materials were synthesized by the sol-gel method. Four particular compositions were chosen LiNi_{1/3}Fe_{1/9}Co_{2/9}Mn_{1/3}O₂ (z = 1/9), LiNi_{1/3}Fe_{1/6}Co_{1/6}Mn_{1/3}O₂ (z = 1/6) and LiNi_{1/3}Fe_{2/9}Co_{1/9}Mn_{1/3}O₂ (z = 2/9) and LiNi_{1/3}Fe_{1/3}Mn_{1/3}O₂ (z = 1/3). The sol-gel method has been largely used for producing materials with high purity and high homogeneity while employing low synthesis temperatures. It has been widely applied in synthesis of the multi cation cathode materials. In the process, atomic level mixing among the precursors can be achieved, thus sol-gel method is chosen for this work in order to obtain pure single phase layered compound.

LiNi_{1/3}Fe_zCo_{1/3-z}Mn_{1/3}O₂ (0 ≤ z ≤ 1/3) powders were synthesized by the sol-gel method using citric acid as a chelating agent. A stoichiometric amount of lithium acetate (Li(CH₃COO)•2H₂O), nickel acetate (Ni(CH₃COO)₂•4H₂O), cobalt nitrate (Co(NO₃)₂•6H₂O), iron nitrate (Fe(NO₃)₃•9H₂O) and manganese acetate

($\text{Mn}(\text{CH}_3\text{COO})_2 \cdot 4\text{H}_2\text{O}$) were dissolved in distilled water and well mixed with an aqueous solution of citric acid. The solution was stirred at 60-70°C for 5-6 hours to obtain a clear viscous gel. The gel was dried in a vacuum oven at 120°C for 24 hours. All the $\text{LiNi}_{1/3}\text{Fe}_z\text{Co}_{1/3-z}\text{Mn}_{1/3}\text{O}_2$ compounds were precalcined in two stages: at 350°C for 5 hours and 450°C for 4 hours and ground before they were calcined at high temperatures (650-950°C) at a heating rate of about 2°C/min. The powders were slowly cooled to room temperature in oxygen. The overall flow of the synthesis process is illustrated in Figure 4-1.

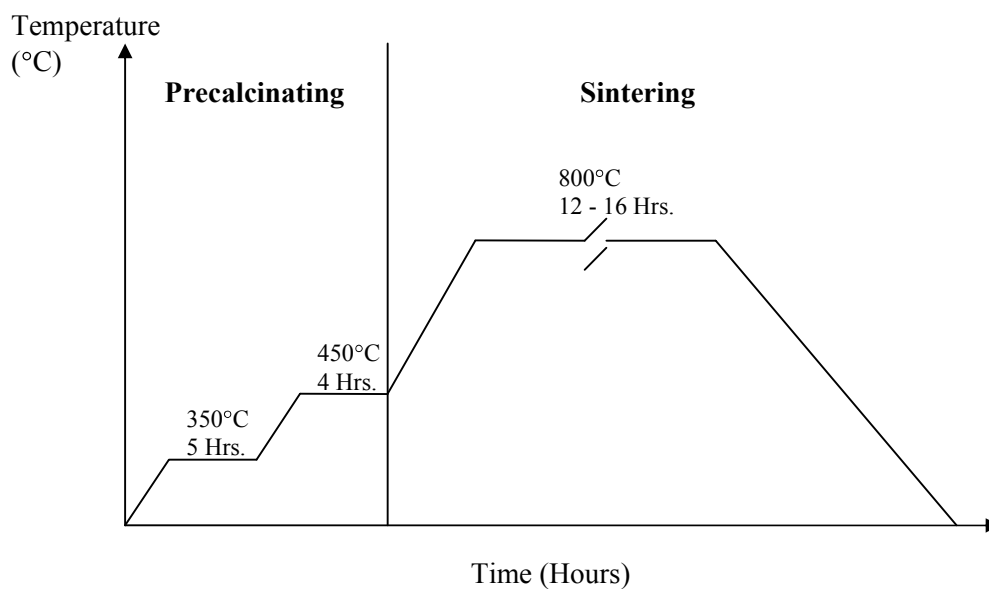


Figure 4-1 Process flow of heat treatment

4.2 Characterization of As-Synthesized Materials

4.2.1 Powder X-ray Diffraction

Powder X-ray diffraction data were collected on a Rigaku diffractometer with Cu $K\alpha 1$ radiation ($\lambda = 1.5406 \text{ \AA}$), operating at 300kV and 60mA. To minimize the

preferred orientation effect, typical in layered lithium intercalation compound, Vaseline is mixed with sample powders to randomize the particles.

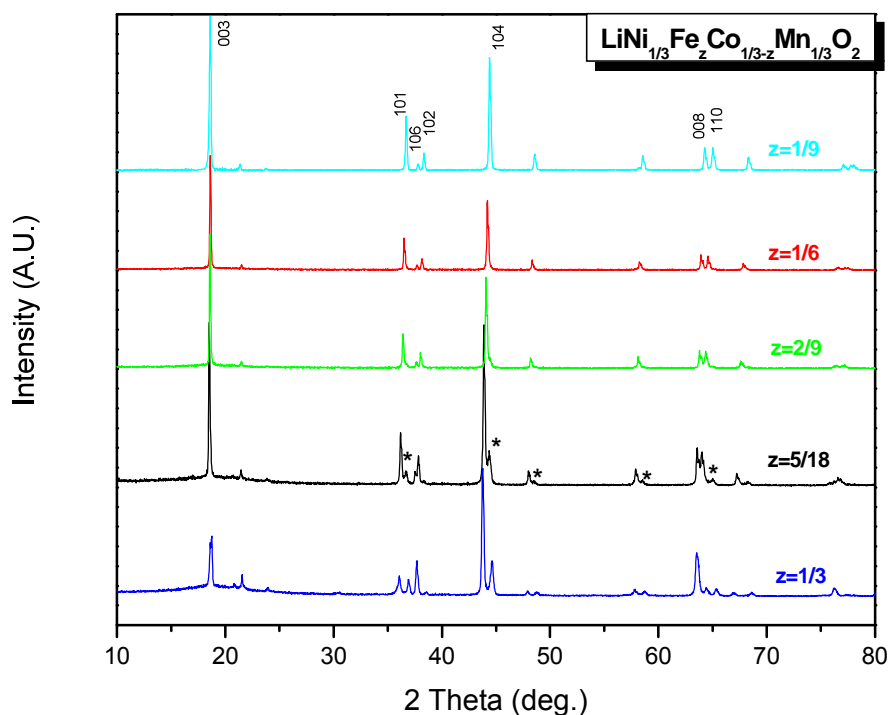


Figure 4-2 XRD spectra for $\text{LiNi}_{1/3}\text{Fe}_z\text{Co}_{1/3-z}\text{Mn}_{1/3}\text{O}_2$ at $z = 1/9$, $z = 1/6$, $z = 2/9$, $z = 5/18$, $z = 1/3$, all synthesized at 850°C .

XRD spectra of $\text{LiNi}_{1/3}\text{Fe}_z\text{Co}_{1/3-z}\text{Mn}_{1/3}\text{O}_2$ for $z = 0$, $z = 1/6$, $z = 2/9$, $z = 5/18$, $z = 1/3$, all synthesized at 850°C are shown in Figure 4-2. X-ray diffraction study shows that when $z \leq 2/9$, a typical layered structure with R-3m space group is obtained; when $z = 5/18$ and $z = 1/3$, another non-layered impurity phase is present contributing to the peaks with *.

Figure 4-3 shows the XRD spectra of $\text{LiNi}_{1/3}\text{Fe}_{1/6}\text{Co}_{1/6}\text{Mn}_{1/3}\text{O}_2$ synthesized at 750°C , 800°C and 850°C . Due to instrument limitation, which requires sample powders to

be pressed in the vertical sample holder, even with Vaseline blending; we cannot evaluate the layered property of the compounds by comparing the peak ratio of I_{003}/I_{104} due to the preferential orientation associated with the pressing. Instead, the clear peak splitting of (108) and (110) can be used to confirm that good layered structures have been obtained. (Rietveld refinement of the powder XRD data was done in another instrument, which will be discussed in detail later) (104) peak for the three compounds is closely examined, as shown in Figure 4-3b), when the synthesis temperature goes up to 850°C, another phase is evolving, evident by an obvious hump right beside the main peak. For samples synthesized below 700°C, poorly crystallized powders were obtained.

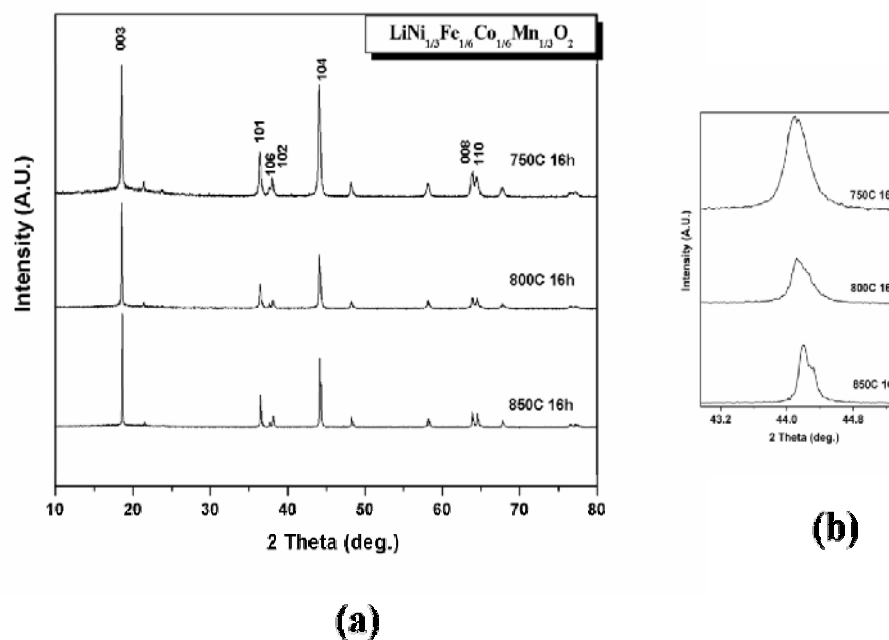


Figure 4-3 XRD spectra of $\text{LiNi}_{1/3}\text{Co}_{1/6}\text{Fe}_{1/6}\text{Mn}_{1/3}\text{O}_2$ synthesized at 750°C, 800°C and 850°C

The optimum synthesis temperature and time for $\text{LiNi}_{1/3}\text{Co}_{1/3}\text{Mn}_{1/3}\text{O}_2$ is about 900°C and 12 hours, respectively [4]. Such synthesis condition is commonly applied in lithium nickel manganese oxides, such as $\text{LiNi}_{1/2}\text{Mn}_{1/2}\text{O}_2$. However, in

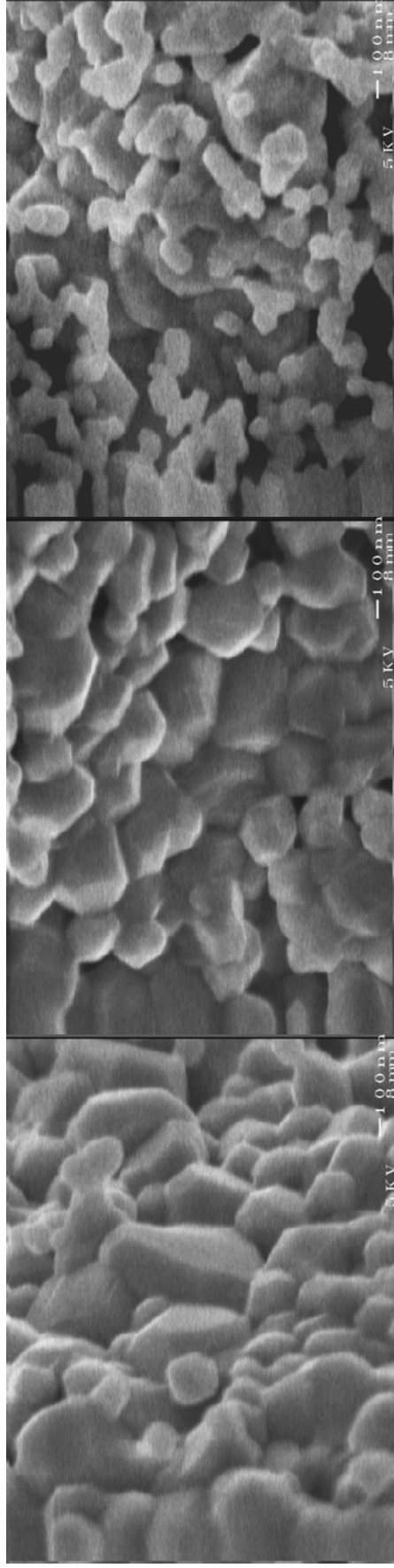
order to obtain pure layered structure in Fe substituted compounds, the synthesis temperature has to be lowered. This fact will be further discussed in terms of the electrochemical properties of the compound synthesized at different temperatures.

4.2.2 Scanning Electron Microscopy

Grain morphology and particle size of $\text{LiNi}_{1/3}\text{Fe}_z\text{Co}_{1/3-z}\text{Mn}_{1/3}\text{O}_2$ compounds were examined by scanning electron microscopy using a JEOL FEG - 6320. The effects of Fe substitution of Co, as well as the sintering temperatures on the grain morphology and size have been carefully studied.

Scanning electron micrographs of $\text{LiNi}_{1/3}\text{Fe}_z\text{Co}_{1/3-z}\text{Mn}_{1/3}\text{O}_2$ $z = 1/6$, $z = 2/9$, $z = 1/3$ all synthesized at 850°C for 16 hours were collected and shown in Figure 4-4. Uniform grain size and faceted grain morphology are observed for $\text{LiNi}_{1/3}\text{Fe}_{1/6}\text{Co}_{1/6}\text{Mn}_{1/3}\text{O}_2$ and $\text{LiNi}_{1/3}\text{Fe}_{2/9}\text{Co}_{1/9}\text{Mn}_{1/3}\text{O}_2$ compounds, where a single layered structure is present, according to the XRD spectra in Figure 4-2. In the Co-free sample $\text{LiNi}_{1/3}\text{Fe}_{1/3}\text{Co}_{1/3}\text{O}_2$ ($z = 1/3$) Figure 4-4c), many small non-faceted particles are surrounding the large faceted crystals. The presence of two distinct powder morphologies is a strong indication of two different phases present in the material.

A comparison of SEM micrographs obtained for $\text{LiNi}_{1/3}\text{Fe}_{1/6}\text{Co}_{1/6}\text{Mn}_{1/3}\text{O}_2$ synthesized at 750°C , 800°C and 850°C is shown in Figure 4-5. The grain size increases from 40-50 nm to 400-500nm as the synthesis temperature raises from 750°C to and 850°C . All samples have a uniform grain size and faceted grain morphology.

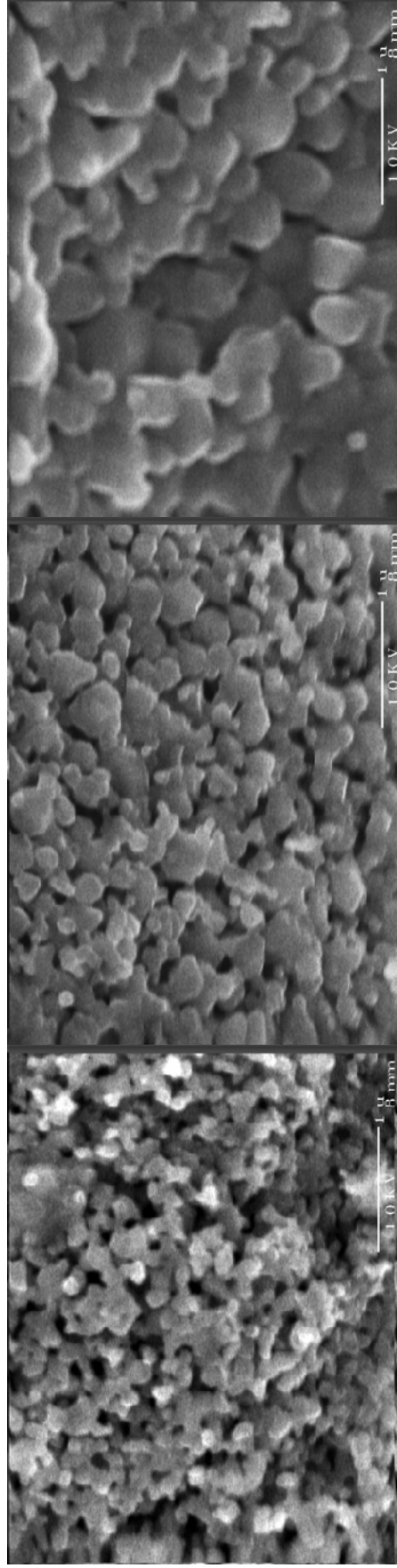


(a)

(b)

(c)

Figure 4-4 SEM images of as-prepared $\text{LiNi}_{1/3}\text{Fe}_z\text{Co}_{1/3-z}\text{Mn}_{1/3}\text{O}_2$ at (a) $z=1/6$, (b) $z=2/9$, (c) $z=1/3$, all synthesized at 850°C .



(a)

(b)

(c)

Figure 4-5. SEM images of as-prepared $\text{LiNi}_{1/3}\text{Co}_{1/6}\text{Fe}_{1/6}\text{Mn}_{1/3}\text{O}_2$ materials synthesized at (a) 750°C (b) 800°C and (c) 850°C

4.2.3 Rietveld Refinement of Powder XRD Data

Rietveld refinement is a method for analyzing XRD patterns by means of a curve-fitting procedure. The least-squares procedure includes the refinement of conventional parameters, such as scale factor, atomic coordinates and temperature factors, and additional parameters such as the lattice parameters, zero-point error for the detector etc. The Rietveld method is a powerful tool, but it is limited by the drawback that affects powder methods in general: the loss of information that arises from the compression of the three-dimensional diffraction pattern into a single dimension. It is important to realize the fact that the Rietveld method is a technique for refining structures and does not, by itself, constitute a method for structure determination. It requires a good starting structure model for successful convergence. In $\text{LiNi}_{1/3}\text{Fe}_z\text{Co}_{1/3-z}\text{Mn}_{1/3}\text{O}_2$ compounds, R-3m – typical structure for O3 type layered transition metal oxide is applied in all refinement procedures. It is assumed there is no cation ordering in the transition metal layer.

Table 4-I. Refined lattice parameters of as-prepared materials

	a_{exp}	c_{exp}	a_{cal}	c_{cal}
$\text{LiNi}_{1/3}\text{Fe}_{1/9}\text{Co}_{2/9}\text{Mn}_{1/3}\text{O}_2$	2.8788	14.3002		
$\text{LiNi}_{1/3}\text{Fe}_{1/6}\text{Co}_{1/6}\text{Mn}_{1/3}\text{O}_2$	2.8859	14.3222	2.9138	14.3690
$\text{LiNi}_{1/3}\text{Fe}_{2/9}\text{Co}_{1/9}\text{Mn}_{1/3}\text{O}_2$	2.8933	14.3470		-

The powder XRD data for the Rietveld refinement were collected by a SIEMENS D5000 diffractometer with Cu $K\alpha 1$ radiation ($\lambda = 1.5406 \text{ \AA}$), operating at 40kV and 40mA. The diffractometer has a sample holder with horizontal orientation. Special care was taken in sample preparation to minimize the preferred orientation effect.

Data for 2theta range of 5-120° was collected with step time 40 seconds and step size 0.02, the 64-hour data collection procedure ensured the high quality (resolution) data for the Rietveld refinement.

The Rietveld refinement data for samples where $x = 1/9$ and $x=1/6$ is summarized in Table 4-II.

Table 4-II. Rietveld refinement parameters for $\text{LiNi}_{1/3}\text{Fe}_{1/9}\text{Co}_{2/9}\text{Mn}_{1/3}\text{O}_2$ and $\text{LiNi}_{1/3}\text{Fe}_{1/6}\text{Co}_{1/6}\text{Mn}_{1/3}\text{O}_2$

	Li/M	a_{hex.}	c_{hex.}	z_{ox.}	k	R_B	Rwp
	n.r.	(Å)	(Å)			(%)	(%)
$\text{LiNi}_{1/3}\text{Fe}_{1/9}\text{Co}_{2/9}\text{Mn}_{1/3}\text{O}_2$	1.02	2.8788	14.3002	0.2579	0.051	3.9	13.3
$\text{LiNi}_{1/3}\text{Fe}_{1/6}\text{Co}_{1/6}\text{Mn}_{1/3}\text{O}_2$	1.02	2.8859	14.3222	0.2580	0.064	4.2	12.1

4.2.4 X-ray Photoelectron spectroscopy

Information of nickel, cobalt, iron and manganese oxidation states in three as-synthesized samples ($z = 0$, $z = 1/6$ and $z = 2/9$) were obtained from X-ray photoelectron spectroscopy (XPS) on the pristine powders. Binding energies were charge-corrected using the C_{1s} peak (285 eV).

XPS is based on the photoelectric effect where the concept of the photon was used to describe the ejection of electrons from a surface when photons impinge upon it. For XPS, Al $\text{K}\alpha$ (1486.6eV) or Mg $\text{K}\alpha$ (1253.6eV) is often the photon energies of choice. In this work, an Al source was used. The XPS technique is highly surface

specific due to the short range of the photoelectrons that are excited from the solid. The penetration depth in solid samples is about 10-100 Å. The energy of the photoelectrons leaving the sample are determined using a *Concentric Hemispherical Analyzer* (CHA) and this gives a spectrum with a series of photoelectron peaks. The binding energies of the peaks are characteristics of each element. The peak areas can be used (with appropriate sensitivity factors) to determine the composition of the materials surface. The shape of each peak and the binding energy can be slightly altered by the chemical state of the emitting atom. Hence XPS can provide chemical bonding information as well. XPS is not sensitive to hydrogen or helium, but can detect all other elements. XPS must be carried out in ultra-high vacuum (UHV) conditions.

X-ray Photoelectron Spectroscopy XPS (Al source) results for $\text{LiNi}_{1/3}\text{Fe}_z\text{Co}_{1/3-z}\text{Mn}_{1/3}\text{O}_2$ cathode materials revealed that the oxidation state of Ni, Mn, Fe and Co in the as-synthesized samples are 2+, 4+, 3+ and 3+, respectively, which is consistent with the first-principle computation results. The binding energies of those cations in the as-prepared compounds are tabulated in Table 4-III.

Shift in binding energy with respect to elemental Fe (the binding energies of Fe $2p_{3/2}$ is about 706 ~708eV [5], 707eV is taken as the reference point for comparison) is decided by the valence state of the Fe; while the chemical environment of the Fe, in this case, the Fe-O polyhedron, determines the peak shape. The binding energies of cations in $\text{LiNi}_{1/3}\text{Fe}_z\text{Co}_{1-z}\text{Mn}_{1/3}\text{O}_2$ for $z = 1/6, 2/9$ and $1/3$ are similar, although there is detectable peak-shape difference in Fe-edge spectra in $\text{LiNi}_{1/3}\text{Fe}_{1/3}\text{Mn}_{1/3}\text{O}_2$ ($z = 1/3$) compared with the other two ($z = 1/6$ & $2/9$), as shown in Figure 4-6. Notice in

Figure 4-6c), there is a small hump in between the Fe2p_{3/2} and Fe2p_{1/2} peaks in LiNi_{1/3}Fe_{1/3}Mn_{1/3}O₂. And this hump starts to evolve in LiNi_{1/3}Fe_{2/9}Co_{1/9}Mn_{1/3}O₂, though it is not obvious. It is an indication of different Fe local environments in those compounds.

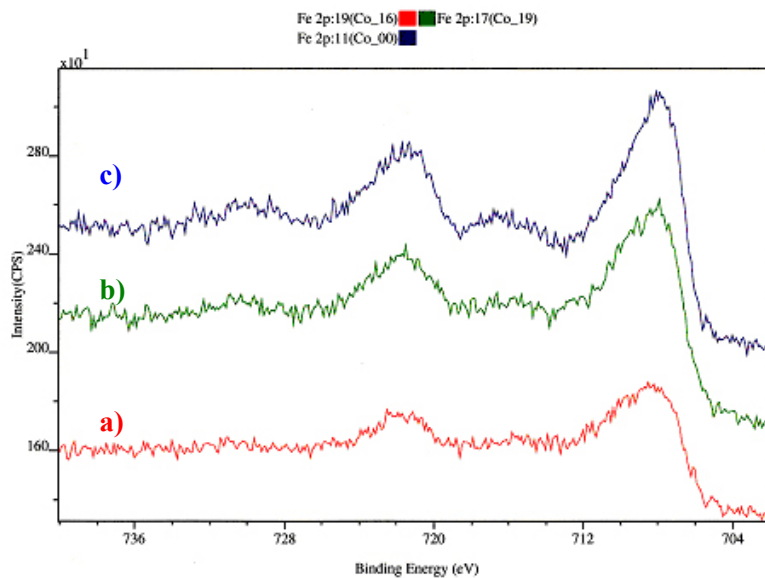


Figure 4-6 XPS spectra of Fe-edge (uncorrected) in LiNi_{1/3}Fe_zCo_{1/3-z}Mn_{1/3}O₂ a) z = 1/6, b) z = 2/9 and c) z = 1/3, all synthesized at 850°C

Table 4-III XPS binding energy for as-prepared materials

	Ni 2p _{3/2} /eV	Fe 2p _{3/2} /eV	Co 2p _{3/2} /eV	Mn 2p _{3/2} /eV
LiNi _{1/3} Fe _{1/6} Co _{1/6} Mn _{1/3} O ₂	854.7 (1.7)	710.9 (3.9)	780.4(1.6)	842.3 (3.3)
LiNi _{1/3} Fe _{2/9} Co _{1/9} Mn _{1/3} O ₂	854.9 (1.9)	711.0 (4.0)	780.4(1.6)	842.4 (3.4)
LiNi _{1/3} Fe _{1/3} Mn _{1/3} O ₂	854.8 (1.9)	710.8 (3.8)	-	842.3 (3.3)

The binding energies for elemental Fe are 719-720eV for 2p_{1/2} and 706-708eV for 2p_{3/2} [5]

4.2.5 ⁵⁷Fe Mössbauer Spectroscopy

Mössbauer spectroscopy can give precise information about the chemical, structural, magnetic and time-dependent properties of a material. Nuclei in atoms undergo a variety of energy level transitions, often associated with the emission or absorption of a gamma ray. These energy levels are influenced by their surrounding environment, both electronic and magnetic, which can change or split these energy levels. Isomer Shift, Quadrupole Splitting and Magnetic Splitting are the primary characteristics of Mössbauer spectra.

Isomer shift arises due to the non-zero volume of the nucleus and the electron charge density due to s-electrons within it. This leads to a monopole (Coulomb) interaction, altering the nuclear energy levels. The isomer shift is for determining valence states, ligand bonding states and electron shielding.

Quadrupole splitting describes the electrical interactions. In the presence of an asymmetrical electric field (present due to an asymmetric charge distribution or ligand arrangement), the nuclear energy levels will be split. In the case of an isotope

with an excited state $I=3/2$ ($I = 1/2$ is the ground state), such as ^{57}Fe , the excited state is split into $m_I = \pm 1/2$ and $m_I = \pm 3/2$, giving a doublet spectrum.

Magnetic splitting arises by the internal field experienced by the nucleus. In the presence of a magnetic field the nuclear spin moment experiences a dipolar interaction with the magnetic field, that is, Zeeman splitting. For ^{57}Fe , six possible transitions between the excited state and ground state can occur.

The two samples: $\text{LiNi}_{1/3}\text{Fe}_{1/9}\text{Co}_{2/9}\text{Mn}_{1/3}\text{O}_2$ and $\text{LiNi}_{1/3}\text{Fe}_{1/9}\text{Co}_{2/9}\text{Mn}_{1/3}\text{O}_2$ (800°C) have been studied using a HALDER type spectrometer with a constant acceleration and a ^{57}Co source (in a Rhodium matrix). The powders were grounded and the samples contained about 10 mg of Fe per cm^2 . The spectra were recorded at 293 K and 4.2 K by using a cryostat with liquid helium. The refinement of these spectra has been performed following the Hesse and Rubartsch method [6].

Figure 4-7 is the Fe Mossbauer spectra obtained at room temperature. A calculation taking into account a distribution of doublets was shown to give the good reliability factors and minimisation of the difference $A_{\text{obs.}} - A_{\text{calc.}}$, and the refinement parameters are shown in Table 4-IV.

The position of the line is associated to the isomer shift δ , $\alpha\text{-Fe}$ being the standard at room temperature. The isomer shift reflects the electronic density present at the nucleus. For Fe, it increases with the ionicity of the Fe-O bonds. δ values were obtained by a first refinement of the spectra using a distribution of Lorentzian lines.

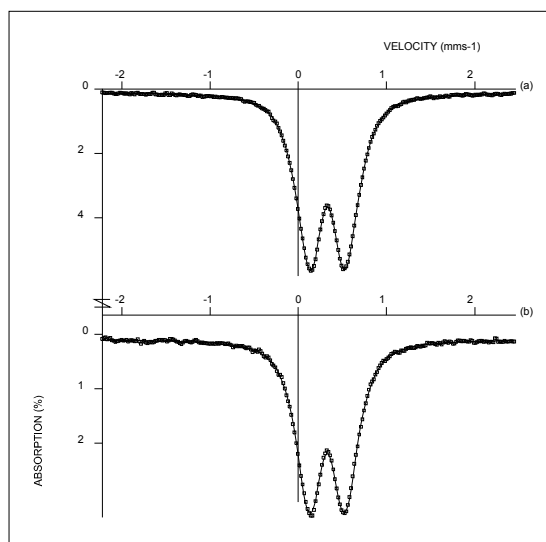


Figure 4-7 Experimental and calculated Mössbauer spectra obtained at 293 K for $\text{LiNi}_{1/3}\text{Fe}_z\text{Co}_{1/3-z}\text{Mn}_{1/3}\text{O}_2$ with (a) $z = 1/6$ and (b) $z = 1/9$. (The dots are experimental values and the lines are calculated values)

Table 4-IV Mössbauer parameters obtained at 293 K

$z = 1/6$	DIS	δ (mm.s^{-1})	Δ (mm.s^{-1}) [*]	Γ (mm.s^{-1})	% [*]	site
	1		0.39	0.45	0.25	49.8
	2		0.44	0.25	50.2	Fe^{3+}
$z = 1/9$	DIS	δ (mm.s^{-1})	Δ (mm.s^{-1}) [*]	Γ (mm.s^{-1})	% [*]	site
	1		0.39	0.44	0.25	47.4
	2		0.43	0.25	52.6	Fe^{3+}

(*) refined parameters

Γ : line width at half height, fixed at 0.25 mm/s, value expected for ^{57}Fe at room temperature.

Two distinct octahedral sites were identified for trivalent iron at room temperature.

The proportion between these two sites is approximately 50/50 in both cases. These two distributions can be distinguished by the value of their isomer shifts (DIS1: $\delta = 0.39 \text{ mm.s}^{-1}$ and DIS2: $\delta = 0.29 \text{ mm.s}^{-1}$). These two sites are probably associated to two different cationic distributions around the iron ions.

The distribution **DIS1** corresponds to a site less covalent than the one associated to the distribution **DIS2**, *i.e.* the average Fe-O distances in site 1 are longer than the ones in site 2. Due to the presence of different cations (Ni^{II} , Co^{III} , Fe^{III} and Mn^{IV}) in the materials with different ionic radii and valence states, we would expect difference in Fe local environments. Another possibility is local LiFeO_2 -formation in the compounds. The LiFeO_2 ground-state structure is not layered, but a structure with symmetry $I4_1/amd$ as shown in Figure 4-8. Different from the layered O3 structure, the LiFeO_2 structure forms a tetragonal supercell of the rocksalt structure. Notice that DIS2 could not be associated to Fe present in a tetrahedral site since the literature value for the isomer shift for Fe in tetrahedral site is close to 0.21mm/s.

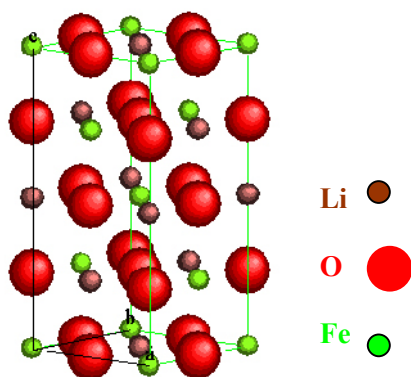


Figure 4-8 Crystal structure of ground state LiFeO_2 , with space group $I4_1/amd$

In order to further understand the compounds by examining their magnetic behavior, Mössbauer data was also collected at 4.2 K, shown in Figure 4-9 and Table 4-V. The resolution of these spectra is not good despite a long counting time. The main reason is the presence of two types of contributions: one (DIS3) is characterised by a superparamagnetism behaviour that is observed in materials characterised by domains very small in size, with no interactions between them; the others (DIS1 and

DIS2) are magnetically ordered at 4.2K. This result shows again that these materials are not homogeneous, consistent with the results found by room temperature

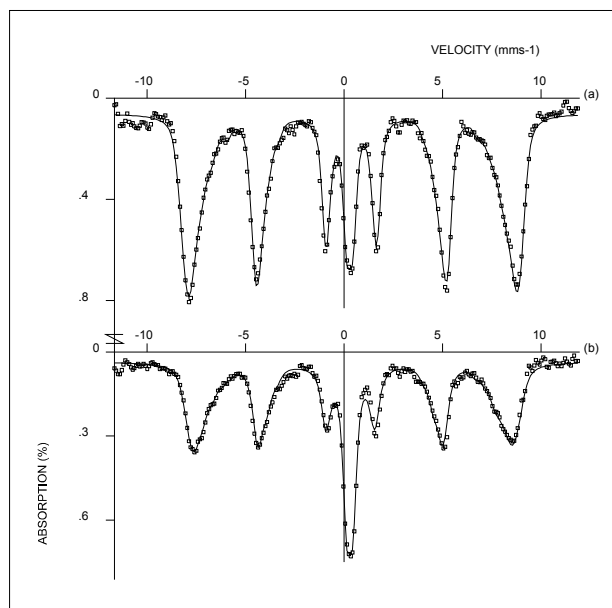


Figure 4-9 Experimental and calculated Mössbauer spectra obtained at 4.2 K for $\text{LiNi}_{1/3}\text{Fe}_x\text{Co}_{1/3-x}\text{Mn}_{1/3}\text{O}_2$ with (a) $x = 1/6$ and (b) $x = 1/9$.

The existence of these two types of contributions indicates that the ordering temperature is perhaps close to 4.2K. The study at 4.2K is in good agreement with the results obtained at $T = 293$ K with the existence of two octahedral sites for the trivalent iron ions. Their Mössbauer parameters remain close but with rather different values for isomer shift δ shows probably that a tendency to segregation exists in these materials with two cationic environments for the Fe ions.

Table 4-V Mössbauer parameters obtained at 4.2 K

x = 1/6	DIS	δ (mm.s ⁻¹)	Γ (mm.s ⁻¹)	ε (mm.s ⁻¹)	Δ (mm.s ⁻¹)*	H (T)	%*	site
	1	0.51	0.35	0.05	-	50.2	42	Fe ³⁺
	2	0.34	0.35	0.001	-	50.0	47	Fe ³⁺
	3	0.34	0.35	-	0.31	-	11	Fe ³⁺
x = 1/9	DIS	δ (mm.s ⁻¹)	Γ (mm.s ⁻¹)	ε (mm.s ⁻¹)	Δ (mm.s ⁻¹)*	H (T)	%*	site
	1	0.51	0.50	0.15	-	48.8	34	Fe ³⁺
	2	0.34	0.50	-0.01	-	48.4	43	Fe ³⁺
	3	0.34	0.40	-	0.31	-	23	Fe ³⁺

(*) refined parameters

H : hyperfine field, internal magnetic field *ε* : quantifies the perturbations brought by the electrostatic interactions to the magnetic interactions.

4.3. Electrochemical Properties

LiNi_{1/3}Fe_zCo_{1/3-z}Mn_{1/3}O₂ electrodes were fabricated by mixing 85:1.5:3.5:10 (w/w) ratio of active material, SS carbon black, KS-6 carbon and polyvinylidene fluoride (PVDF), respectively, in N-methyl-pyrrolidinone (NMP). The resulting slurry was cast onto an aluminum current collector and dried under vacuum oven overnight. The electrode foils were cut into disks of 8mm diameter and cold pressed. Electrochemical measurements were made using coin-type cells comprising a Li metal counter electrode with a 1M solution of LiPF₆ in EC/DMC (1:1 v/v, Merck LP30) as the electrolyte. The cells were assembled in an argon filled glove box where the moisture level is less than 1ppm. The cells were charge-discharged cycled using a Maccor battery tester at C/10 (or C/20) over a potential range between 3.0V to 4.5V/4.8V.

Electrodes of LiNi_{1/3}Fe_{1/6}Co_{1/6}Mn_{1/3}O₂ synthesized at 750 °C, 800 °C and 850 °C were cycled at a rate of C/10 (based on 281mAh/g total capacity) between 3.0V and 4.5V. The first charge and discharge curves for each sample are shown in Figure 4-

10. Qualitatively, the potential curves are very similar, exhibiting a relatively flat potential on charging in the range of 3.7 to 3.9 V, and then a relatively steeply sloping curve on discharge. The compound synthesized at 750 °C shows smaller polarization which could be related to its smaller grain size. There is a significant amount of irreversible capacity after the first charge for all three samples. As the synthesis temperature increases from 750 °C, 800 °C to 850 °C, the first charge capacity decreases from 220mAh/g, 200mAh/g to 187mAh/g; the first discharge capacity changes from 150mAh/g, 139mAh/g to 134mAh/g.

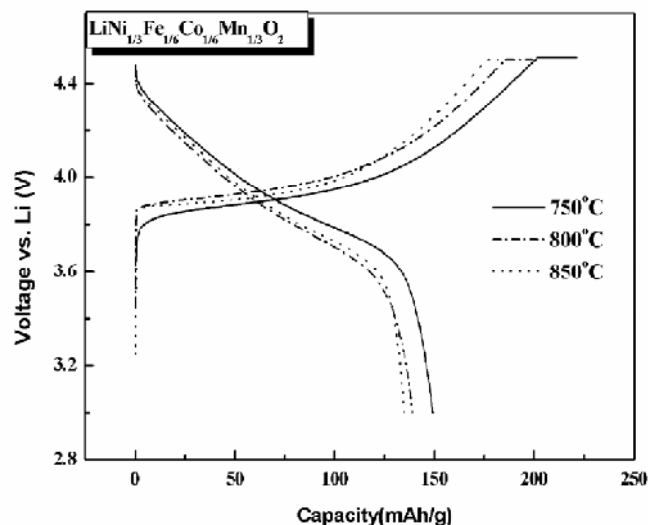


Figure 4-10 Variation of the cell potential on first charging then discharging the cells at C/10 for $\text{LiNi}_{1/3}\text{Fe}_{1/6}\text{Co}_{1/6}\text{Mn}_{1/3}\text{O}_2$ prepared at 750°C, 800°C and 850°C

The delithiation potential of the material synthesized at 750°C is plotted together with the calculated potential curve in Figure 3-5. The potential difference between the calculated and experimental data is suggested to be 0.7~0.8V. [7] The correction of 0.9V in this case was added to the calculated potential to display a result that can be compared directly with the experimental values, as shown in Figure 4-11. The

experimental charge-discharge curve matches the calculated one well in the range of $1/3 \leq x \leq 1$. The practical specific capacity of this material will likely be more than 250mAh/g if the cell is charged to approximately 4.8V, according to the computational prediction.

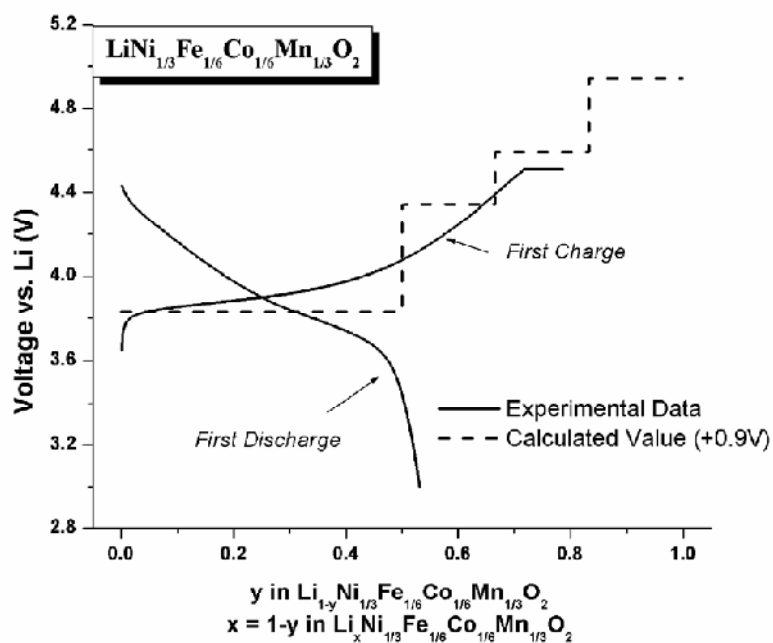


Figure 4-11 Comparison of experimental potential curve (sample synthesized at 750°C) with the predicted potential curve by first principles calculation.

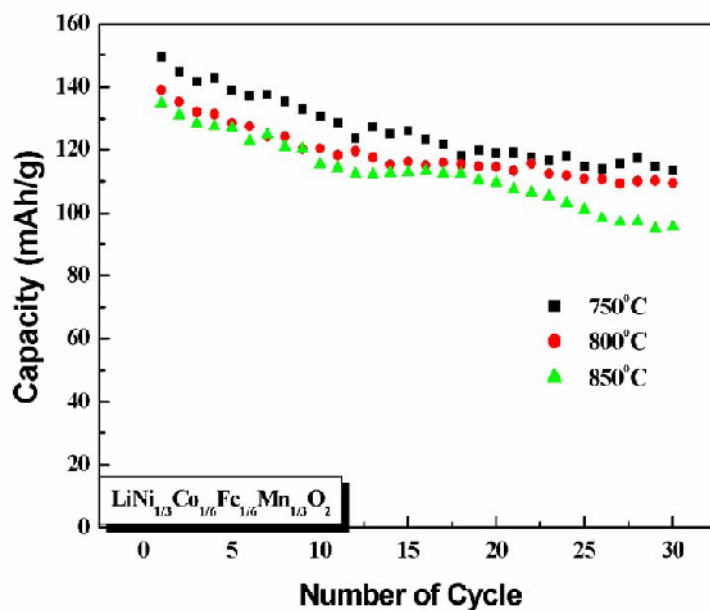


Figure 4-12 Charge and discharge capacity vs. cycle number curves of the $\text{LiNi}_{1/3}\text{Fe}_{1/6}\text{Co}_{1/6}\text{Mn}_{1/3}\text{O}_2$ materials synthesized at 750, 800, and 850°C for 16 h.

The capacity retention up to 30 cycles is reasonably good for all samples, as demonstrated in Figure 4-12. The possible reasons for the large first-cycle irreversible capacity will be discussed later. A preliminary study shows that the first cycle reversible capacity can be increased by 20% with surface treatment of the synthesized powders. This implies the surface degradation of the as-synthesized material might have a significant impact on the reversible capacity, similar to that has been demonstrated in LiCoO_2 system.[8]

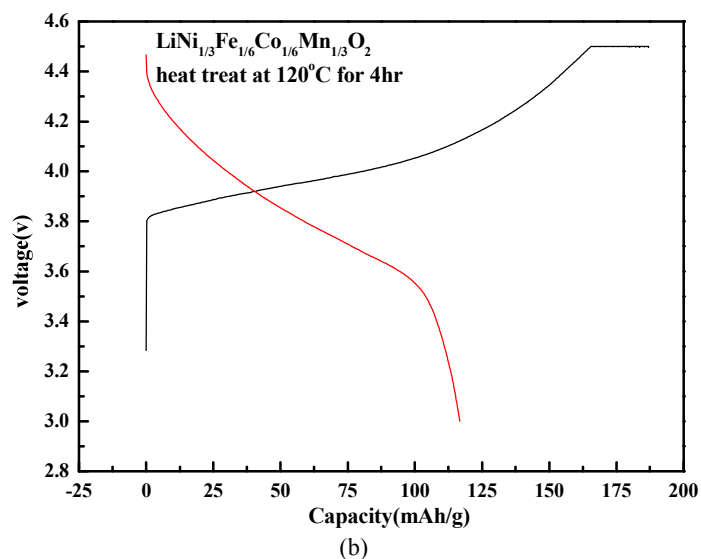
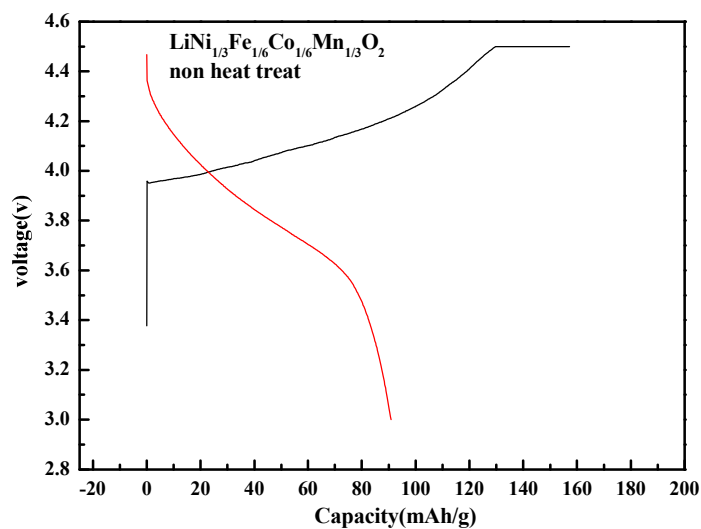


Figure 4-13. Comparison of first cycle potential curve of $\text{LiNi}_{1/3}\text{Fe}_{1/6}\text{Co}_{1/6}\text{Mn}_{1/3}\text{O}_2$ with (a) and without (b) heat treatment of the electrode in the glove box

Electrochemical cycling of $\text{LiNi}_{1/3}\text{Fe}_z\text{Co}_{1/3-z}\text{Mn}_{1/3}\text{O}_2$ compounds for and $z = 1/6$ and $z = 2/9$ synthesized at 800°C were carried out at $C/10$ between 3 - 4.8V. Figure 4-14 shows the comparison of first charge-discharge potential curves for the two compounds. Though more Fe doping ($z = 2/9$) gives lower potential, thus higher charge capacity, the percentage of irreversible capacity is much higher than that of z

= 1/6. In addition, the sample with more Fe doping cycled poorly. This is suspected that Fe migration to the tetrahedral sites could be the reason for reduced discharge capacity, which will be further discussed in the next section.

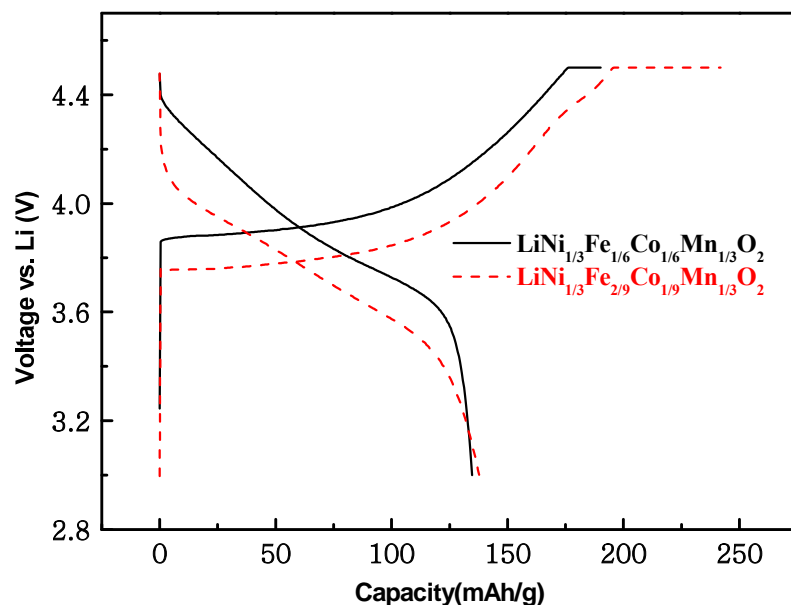


Figure 4-14 First charge discharge curve comparison of $\text{LiNi}_{1/3}\text{Fe}_{1/6}\text{Co}_{1/6}\text{Mn}_{1/3}\text{O}_2$ and $\text{LiNi}_{1/3}\text{Fe}_{2/9}\text{Co}_{1/9}\text{Mn}_{1/3}\text{O}_2$

In summary, among the samples synthesized, $\text{LiNi}_{1/3}\text{Fe}_{1/6}\text{Co}_{1/6}\text{Mn}_{1/3}\text{O}_2$ sintered at 750°C has shown the good electrochemical properties in terms of reversible capacity and capacity retention. Excessive Fe substitution ($z > 2/9$) leads to significant decrease both in initial capacity and capacity retention. The characterization of partially charged materials focuses on $\text{LiNi}_{1/3}\text{Fe}_{1/6}\text{Co}_{1/6}\text{Mn}_{1/3}\text{O}_2$, which is compared with the first principles computation performed on the compound with the same composition.

4.4 Characterization of Partially Charged Materials

4.4.1 XPS and Change in Electronic Structures

X-ray photoelectron spectroscopy (XPS) was applied to corroborate the electronic behavior predicted computationally. Ex-situ X-ray photoelectron spectroscopic study was carried out to study the valence shifts of Ni, Co, Fe and Mn in $\text{LiNi}_{1/3}\text{Fe}_{1/6}\text{Co}_{1/6}\text{Mn}_{1/3}\text{O}_2$ and in partially charged $\text{Li}_x\text{Ni}_{1/3}\text{Co}_{1/6}\text{Fe}_{1/6}\text{Mn}_{1/3}\text{O}_2$ ($x \approx 1/2$). The electrodes were charged to 4.4V. The binding energies of those cations in the as-prepared and partially charged compounds are tabulated in Table VI. Indicated by the binding energy shift of the $2p$ electrons for the transition metal cations from their elemental values [5], XPS confirms that the valence states of Ni, Fe, Co, and Mn in the as-synthesized $\text{LiNi}_{1/3}\text{Fe}_{1/6}\text{Co}_{1/6}\text{Mn}_{1/3}\text{O}_2$ are 2+, 3+, 3+ and 4+ respectively, as mentioned before. Furthermore, as lithium is removed from the compound, both $\text{Ni}^{2+}/\text{Ni}^{3+}/\text{Ni}^{4+}$ and $\text{Fe}^{3+}/\text{Fe}^{4+}$ redox couples are activated, revealed by an obvious shift in the binding energies of Ni $2p$ and Fe $2p$ edges. No obvious shifts in Co and Mn edges were observed. The results are in good agreement with the calculated change of valence states during delithiation.

It is expected based on the XPS study that for the delithiated cathode materials $\text{Li}_x\text{Ni}_{1/3}\text{Fe}_z\text{Co}_{1/3-z}\text{Mn}_{1/3}\text{O}_2$ cycled in the potential window of 3.0 to 4.5V, Ni and Fe redox couples are activated, while Co and Mn remain unchanged in their oxidation states and chemical environment.

Table 4-VI XPS binding energy for as-prepared and partially-charged materials

	Ni	Fe	Co	Mn
	$2p_{3/2}/\text{eV}$	$2p_{3/2}/\text{eV}$	$2p_{3/2}/\text{eV}$	$2p_{3/2}/\text{eV}$
LiNi_{1/3}Fe_{1/6}Co_{1/6}Mn_{1/3}O₂	854.7	710.9	780.4	842.3
	(1.7)	(3.9)	(1.4)	(3.3)
Li_xNi_{1/3}Fe_{1/6}Co_{1/6}Mn_{1/3}O₂	855.5	711.8	780.4	842.1
$x \approx 1/2$	(2.5)	(4.8)	(1.4)	(3.1)

* Number in the parentheses - shift in binding energy

4.4.2 Ex-situ XRD and Lattice Parameter

Ex-situ X-ray diffraction was carried out to characterize partially charged LiNi_{1/3}Fe_{1/6}Co_{1/6}Mn_{1/3}O₂. The first cell was charged to 4.5V and in open circuit relaxation for 12 hours (OCV = 4.1V) and disassembled in an argon-filled glove box. The second cell was charged to 4.5V and discharged to 3.0V, followed by open circuit relaxation for 12 hours (OCV = 3.8 V). The XRD spectra were depicted in Figure 4-15 a) and b) for the two samples respectively. No major second phase was observed in both samples.

As shown in Table 4-VII, the calculated lattice parameters predicted correctly the trend of change in *a* and *c* lattice parameters with various lithium concentrations. The first principles calculated *a* lattice parameter decreases in the range of $1/3 \leq x \leq 1$ by approximately 2.2%. The calculated lattice parameter *c* increases by about 4.2% in the range of $1/3 \leq x \leq 1$. However, in experiment the increase is much more subtle. It is commonly believed that the oxygen-oxygen columbic repulsion force

and the electrostatic attraction of Li^+ and O^{2-} contribute to the change in c upon lithium removal. As x decreases (delithiation), there are less Li^+ ions attracting O^{2-} across the layers, resulting in increase of c . At the end of delithiation, when there is possibly charge transfer occur on oxygen, making oxygen ion less negative and O-O repulsion becomes weaker, which leads to decrease in c -axis. To explain why experimentally the change in c axis is less obvious than calculated change, one possibility is that due to the presence of transition metal ion in the lithium layer, the highly positively charged transition metal ions moderate the change in electrostatics caused by Li removal. A recent study by Van der Ven and Ceder on $\text{LiNi}_{1/2}\text{Mn}_{1/2}\text{O}_2$ demonstrated such possibility in more details[9].

Table 4-VII, Comparison of experimental and calculated lattice parameters at various lithium concentrations

	Voltage (V)	a_{exp} (Å)	c_{exp} (Å)	a_{cal} (Å)	c_{cal} (Å)
$x=1$	3.0V	2.8859	14.3222	2.9138	14.3690
$x=0.36$	4.1V	2.8448	14.3466	2.8490 ($x=1/3$)	14.9709
$x=0.77$	3.8V	2.8691	14.3298	2.8922 ($x=5/6$)	14.4359

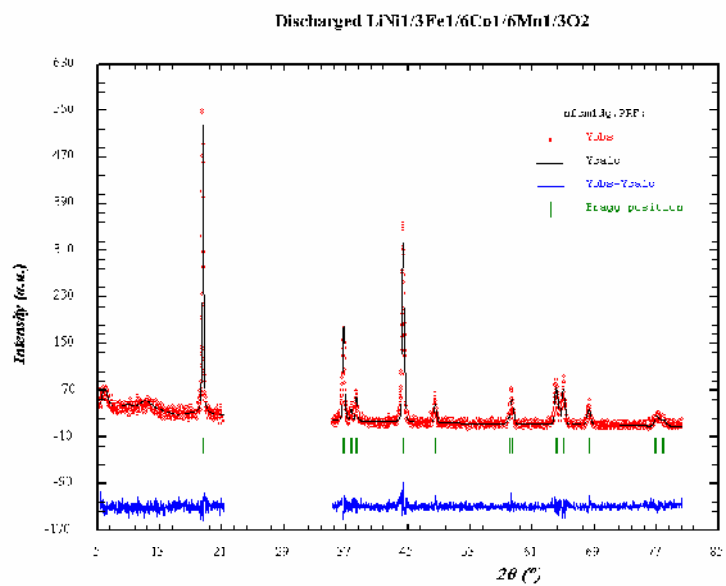
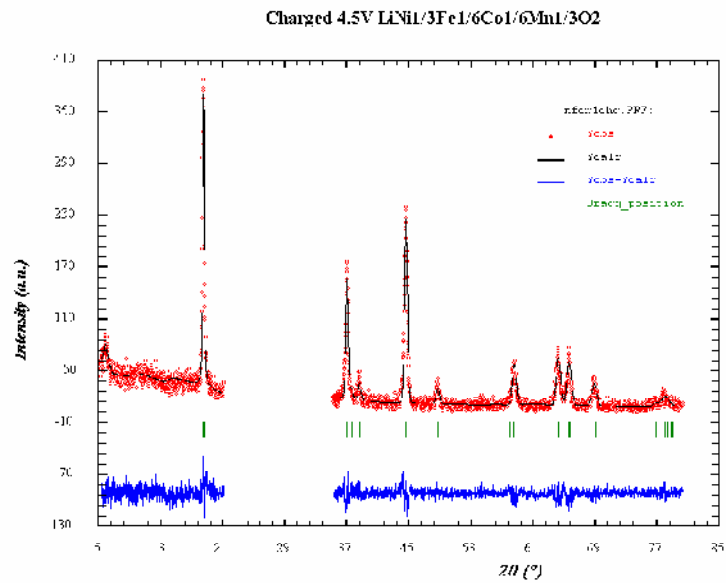


Figure 4-15 Powder XRD spectra of charged $\text{LiNi}_{1/3}\text{Fe}_{1/6}\text{Co}_{1/6}\text{Mn}_{1/3}\text{O}_2$ (a) $x = 0.36$ and (b) $x = 0.77$

4.4.3 XAS and TM-O Bond Lengths

X-ray absorption spectroscopy (XAS) experiments were carried out in transmission mode at beam line BL-17C at the National Synchrotron Radiation Research Center (NSRRC) in Hsinchu, Taiwan. The storage ring was operated with electron energy of 1.5 GeV and a current between 100 and 200mA. A Si(111) double-crystal monochromator was employed for energy selection. High-order harmonic contamination was rejected by mirrors. The intensities of the incident and transmitted beams were measured by gas ionization chambers. Energy scans of the sample were performed at Ni, Co, Fe and Mn K-edges.

X-ray Absorption Spectroscopy is the modulation of the x-ray absorption coefficient $\mu(E)$ at energies near and above an x-ray absorption edge. It utilizes high intensity, collimated x-ray sources at synchrotron radiation facilities. ($0.03 \text{ \AA} \leq \lambda \leq 12 \text{ \AA}$ or energy $1\text{keV} \leq E \leq 500\text{keV}$)

The amplitude of the back-scattered photo-electron at the absorbing atom will oscillate with energy, causing oscillation in $\mu(E)$. Such oscillations are an interference effect due to the presence of the neighboring atoms. As the photo-electron

1. leaves the absorbing atom
2. scatters from the neighbor atoms
3. returns to the absorbing atom

a simple model (Figure 4-16) can be built with spherical wave for the photo-electron:

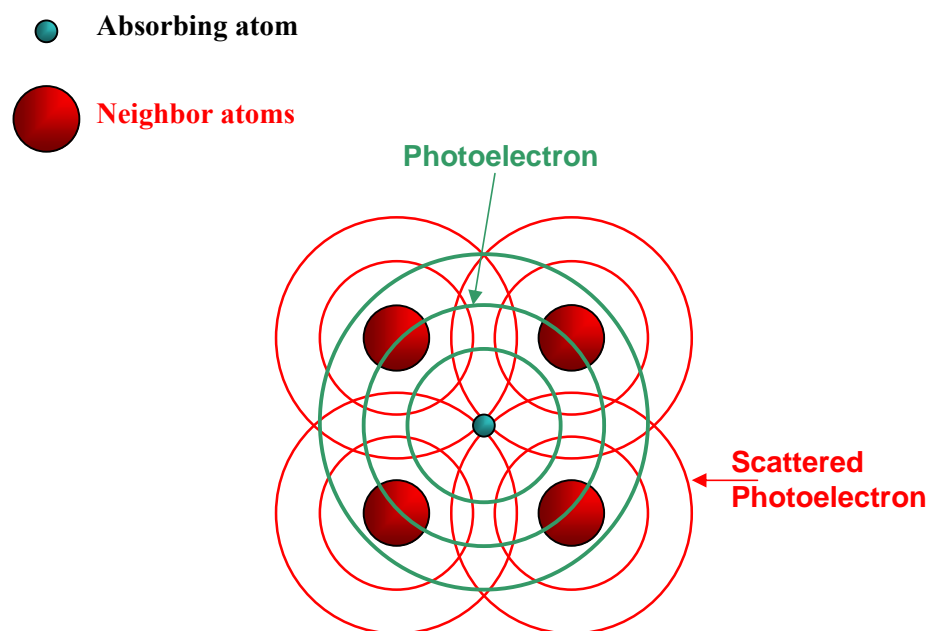


Figure 4-16 Schematic representation of back-scattered photo-electron at the absorbing atom

It is divided into two regimes:

X-ray Absorption Near-Edge Spectroscopy (**XANES**), this technique is able to determine

- Electronic structures
- Symmetry
- Chemical / Oxidation state

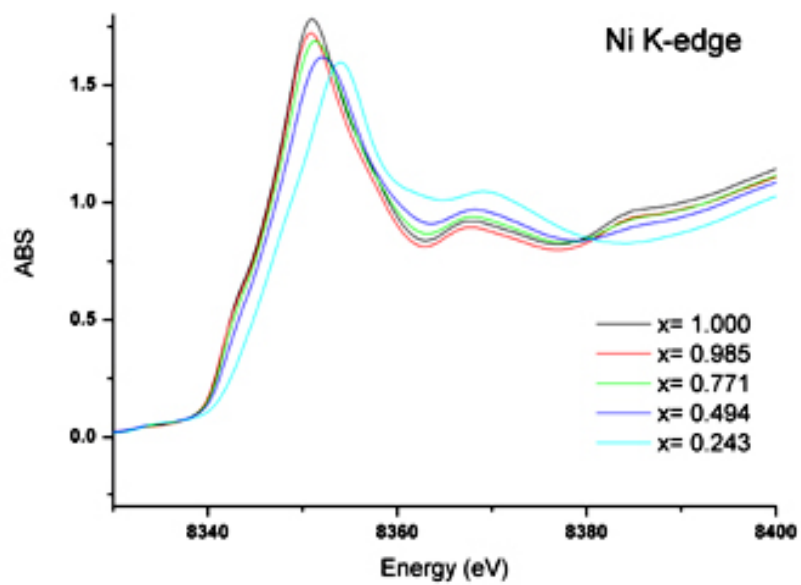
Extended X-ray Absorption Fine-Structure (**EXAFS**), which contains information about an element's local coordination and chemical state.

- Coordination number
- Radius
- Debye-Waller factor

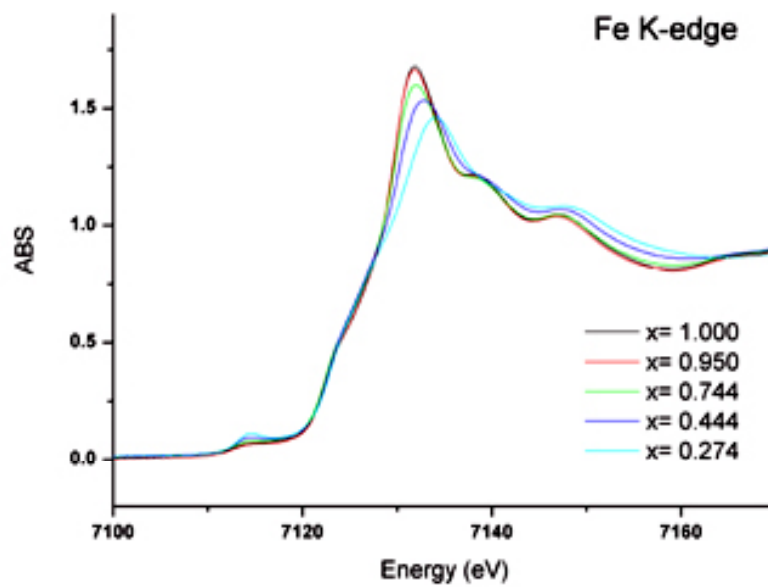
The photo electron mean free path is typically 5 – 10 Å (< 25 Å) for much of the EXAFS range. EXAFS is a local atomic probe.

4.4.3.1 XANES

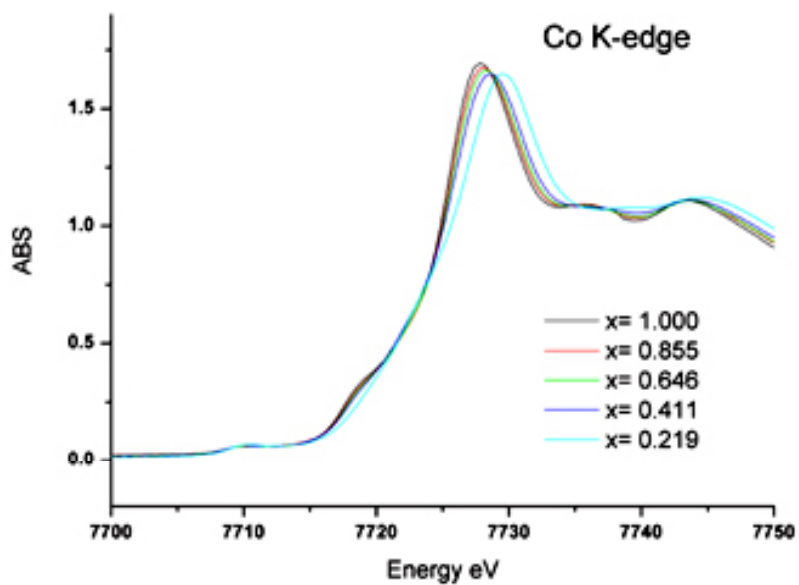
X-ray absorption near-edge structure (XANES) provides information about the valence state of the absorbing atom. The XANES results obtained for the $\text{Li}_x\text{Ni}_{1/3}\text{Fe}_{1/6}\text{Co}_{1/6}\text{Mn}_{1/3}\text{O}_2$ material are shown in this work. Parts (a), (b), (c) and (d) of Figure 4-17 show the Ni, Co, Fe and Mn K-edges XANES spectra of this material, respectively. As observed easily in Figure 4-17(a) and b), the Ni edges of $\text{Li}_x\text{Ni}_{1/3}\text{Fe}_{1/6}\text{Co}_{1/6}\text{Mn}_{1/3}\text{O}_2$ at $x = 1.0, 0.985, 0.771, 0.494$ and 0.243 shifts to higher energy upon charging. This indicates that the valence state of Ni in $\text{Ni}_{1/3}\text{Fe}_{1/6}\text{Co}_{1/6}\text{Mn}_{1/3}\text{O}_2$ changes from $2+$ to $3+$ or $4+$. A similar phenomenon is also observed in the Fe K-edge XANES spectra. No significant energy shift can be observed in the Co and Mn XANES spectra as shown in Figure 4-17 (c) and (d), which is consistent with all previous experimental and computation data. Mn ions do not appear to actively participate in the charge compensation process, and Co ions are not activated completely during the charging process at cutoff voltage 4.5V.



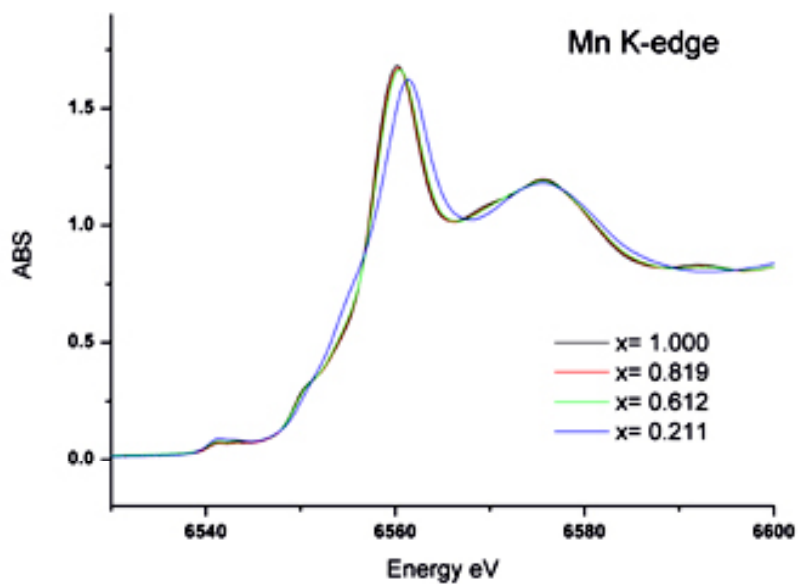
(a)



(b)



(c)

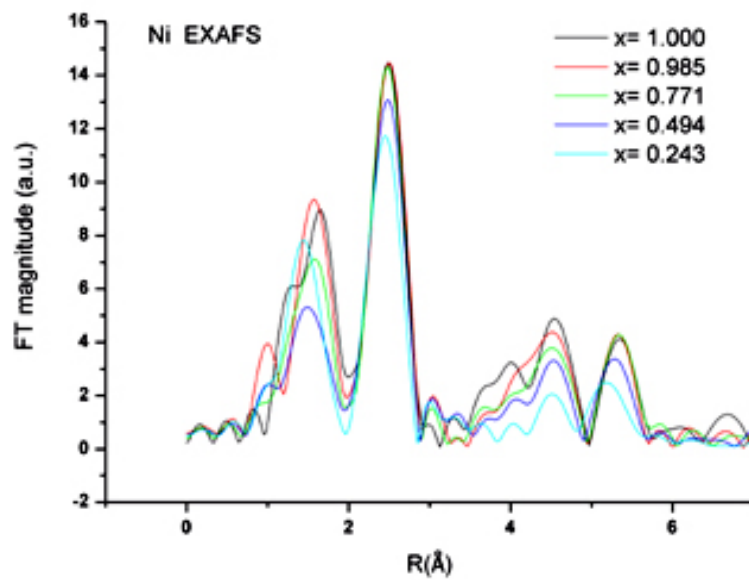


(d)

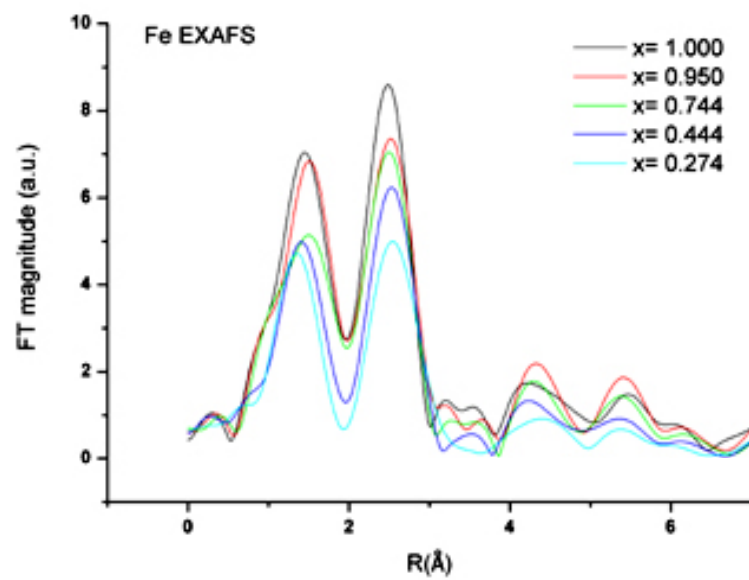
Figure 4-17 XANES spectra of a) Ni edge b) Fe edge c) Co edge and d) Mn edge of $\text{LiNi}_{1/3}\text{Fe}_{1/6}\text{Co}_{1/6}\text{Mn}_{1/3}\text{O}_2$

4.4.3.2 EXAFS

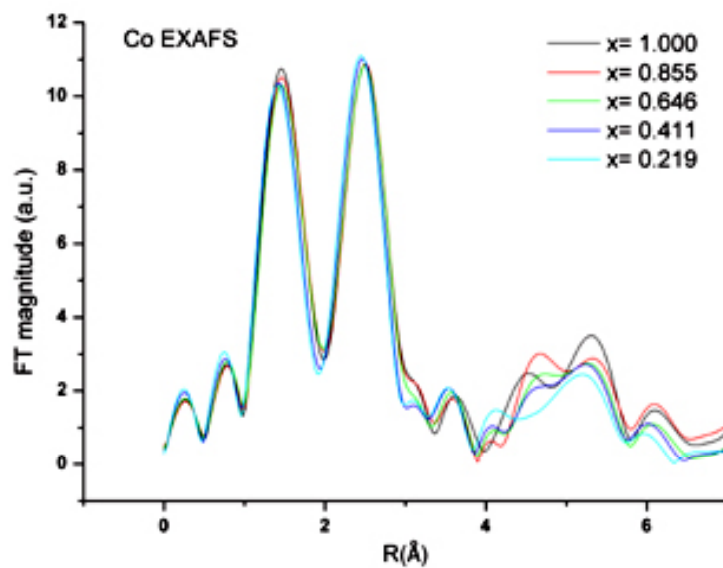
Figure 4-18 a)-d) shows the Fourier transform magnitudes of the Ni, Fe, Co and Mn K-edge EXAFS spectra during charge. The first coordination shell consists of oxygen, while the peak feature of the second coordination shell is dominated by transition metal cations. The most significant change during the charge is observed in the first coordination shell around Ni atoms. The dramatic changes of the first coordination peaks positions indicate that the charge compensation does mainly occur at the Ni sites and results in a large decrease in the average Ni-O bond length. There is also a considerable amount of shift of the first coordination peaks for Fe atoms, indicating that the charge compensation also happens at the Fe sites. Another obvious change is that the relative intensity ratio of the first coordination peak to the second coordination peak reverses for Fe atoms upon lithium removal. As this indicates a local environment change around the Fe sites, speculation of Fe migration to the Li sites in the Li layer rises. When Fe migrates to the Li layer, Fe will be surrounded by Li atom, which has a much weaker scattering power than the transition metal atoms; thus the peak intensity of the second coordination shell is reduced. This is highly possible since Fe^{3+} has 3d⁵ electronic structure, therefore no ligand field stabilization energy exists. In addition, a preliminary study on the susceptibility of Fe migration by first principles computations show that the migration barrier is small enough, comparable to that of Mn^{3+} . In consistency with the XANES spectra, no significant changes are observed in the first and second coordination shells around Co and Mn atoms, as illustrated in Figure 4-18 c) and d). The trend in TM-O bond length changes during charging agrees very well with the first principles computed ones, as shown in Figure 8 in the previous chapter.



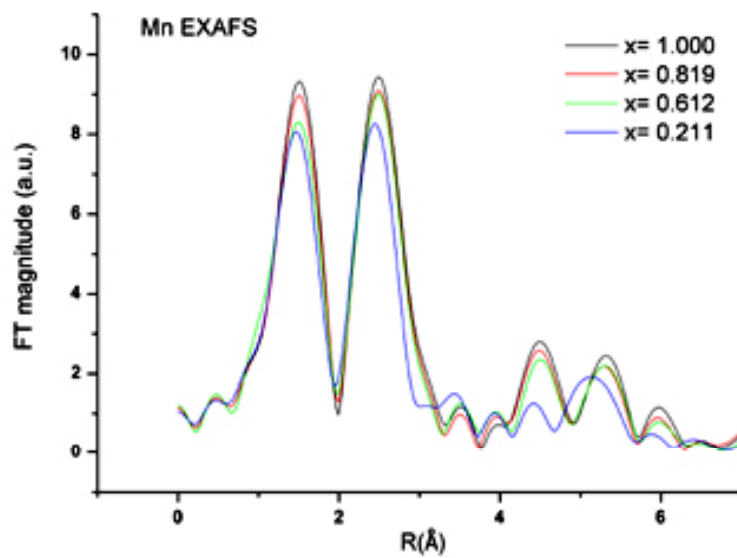
(a)



(b)



(c)



(d)

Figure 4-18 EXAFS spectra of a) Ni edge b) Fe edge c) Co edge and d) Mn edge of $\text{LiNi}_{1/3}\text{Fe}_{1/6}\text{Co}_{1/6}\text{Mn}_{1/3}\text{O}_2$

4.5 First Principles Analysis of Fe Stability in Layered Oxides

To better understand the in-situ EXAFS data, an evaluation of the Fe stability in the layered structure was carried out with first principles computation. We adopted the mechanism proposed by Reed and Ceder [10], and calculated the energy barrier for the migration of Fe ions from octahedral site to tetrahedral site when the material is partially delithiated. The lowest energy path starts with a hop from a transition metal layer octahedron to an adjacent lithium plane tetrahedron through the triangular face shared by the two sites. To get a qualitative understanding, we calculated three states 1) layered structure (free of defect) 2) Fe defect in the shared face between transition metal layer octahedron and Li layer tetrahedron (transition state) and 3) Fe defect in Li layer tetrahedron

Two virtual compositions $\text{Li}_{1/2}\text{Zr}_{1/2}\text{Fe}_{1/2}\text{O}_2$ and Li_0FeO_2 were used for investigating the migration barrier of Fe^{3+} and Fe^{4+} respectively. As it can be seen clearly in Figure 4-19, in $\text{Li}_{1/2}\text{Zr}_{1/2}\text{Fe}_{1/2}\text{O}_2$ when a Li layer tetrahedron is surrounded by Li vacancies, the activation barrier for a neighboring Fe to move into that tetrahedron through the triangular oxygen face is 0.5eV. The energy of the structure with one Fe^{III} tetrahedron defect lies beneath that of un-defect structure, which indicates the Fe^{3+} prefers the tetrahedron coordination. In Li_0FeO_2 , the energy of the structure with one Fe^{IV} tetrahedron defect is 0.37eV higher than that of un-defect structure. Furthermore, the activation barrier for a Fe^{IV} to move into the tetrahedron through the triangular oxygen face is calculated to be as high as 4.9eV. This indicates that in the fully delithiated structure, Fe^{4+} refers the octahedron coordination. In summary, octahedral Fe^{3+} is susceptible to migration to tetrahedral site when Li is partially removed from the layered structure, according to the first principles computation.

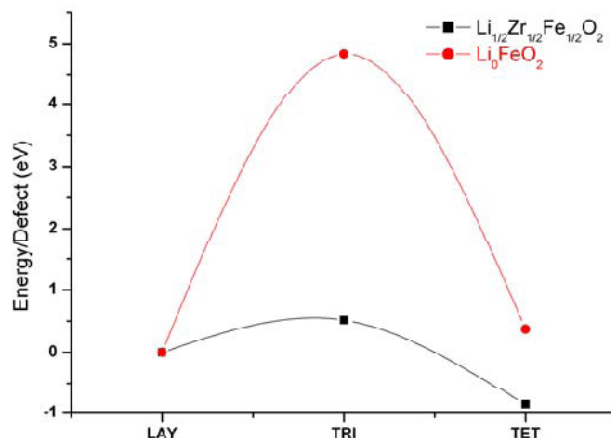


Figure 4-19 Energies of LAY: layered undefected structure; TRI: Fe defect in shared face between transition metal layer octahedron and Li layer tetrahedron; TET: Fe defect in Li layer tetrahedron

The speculation of Fe migration to tetrahedron in the Li layer from the in-situ EXAFS data requires further in-depth investigation.

4.6 Conclusions

Motivated by a series of first principles calculations on $\text{LiNi}_{1/3}\text{TM}_{1/3}\text{TM}_{2/3}\text{O}_2$, $\text{LiNi}_{1/3}\text{Fe}_z\text{Co}_{1/3-z}\text{Mn}_{1/3}\text{O}_2$ ($0 \leq z \leq 1/3$) cathode materials were synthesized by the sol-gel method. Excessive Fe substitution ($z > 2/9$) leads to evolution of non-layered impurity phase, which can be clearly seen by powder XRD and SEM experiments. Preliminary X-ray Photoelectron Spectroscopy XPS (Al source) results for $\text{LiNi}_{1/3}\text{Fe}_z\text{Co}_{1/3-z}\text{Mn}_{1/3}\text{O}_2$ cathode materials revealed that the oxidation state of Ni, Mn, Fe are 2+, 4+ and 3+, respectively, which is consistent with the first-principle computation results. We predicted and confirmed that Fe substitution would lead to a lower potential at the end of charge. The $\text{LiNi}_{1/3}\text{Fe}_{1/6}\text{Co}_{1/6}\text{Mn}_{1/3}\text{O}_2$ compound synthesized at 750°C shows reversible capacity of 150mAh/g with reasonably good

capacity retention. This material may be considered as potential cathode material in lithium ion battery. First principles electronic structure computations indicate that Ni and Fe are simultaneously oxidized in this material. Computations further indicate that Co will only be oxidized at the very end of charge. Both XPS and XAS study on delithiated $\text{Li}_x\text{Ni}_{1/3}\text{Fe}_{1/6}\text{Co}_{1/6}\text{Mn}_{1/3}\text{O}_2$ reveals that in the potential window of 3.0 to 4.5V, Ni and Fe redox couples are activated, while Co and Mn remain unchanged in their oxidation states and chemical environment.

In this work, we have demonstrated that an integrated approach of computation and experiment has produced a new electrode material with very few iteration steps in the material design cycle. We believe that such direct integration of ab-initio methods with experimental research holds promise for significantly shortening the development cycle of materials.

References:

1. C. Delmas, et al., *An overview of the Li(Ni,M)O₂ systems : syntheses, structures and properties*. *Electrochimica Acta*, 1999. **45**: p. 243-253.
2. C. Delmas, et al., *Effect of iron on the electrochemical behaviour of lithium nickelate : from LiNiO₂ to 2D-LiFeO₂*. *Solid State Ionics*, 2000. **135**: p. 71.
3. E.J. Wu, P.D. Tepesch, and G. Ceder, *Size and charge effects on the structural stability of LiMO₂ (M = transition metal) compounds*. *Philosophical Magazine B*, 1998. **77**(4): p. 1039-1047.
4. B.J. Hwang, et al., *A combined computational/experimental study on LiNi_{1/3}Co_{1/3}Mn_{1/3}O₂*. *Chemistry of Materials*, 2003. **15**(19): p. 3676-3682.
5. www.srdata.nist.gov/xps/.
6. J. Hesse and A. Rubartsch, *J. Phys. E. Sci. Instrum.*, 1974. **7**: p. 526.
7. M.K. Aydinol, et al., *Ab initio study of lithium intercalation in metal oxides and metal dichalcogenides*. *Physical Review B*, 1997. **56**(3): p. 1354-1365.
8. Z.H. Chen and J.R. Dahn, *Methods to obtain excellent capacity retention in LiCoO₂ cycled to 4.5 V*. *Electrochimica Acta*, 2004. **49**(7): p. 1079-1090.
9. A. Van der Ven and G. Ceder, *Ordering in Li_x(Ni_{0.5}Mn_{0.5})O₂ and its relation to charge capacity and electrochemical behavior in rechargeable lithium batteries*. *Electrochemistry Communications*, 2004. **6**: p. 1045-1050.
10. J. Reed, G. Ceder, and A. Van Der Ven, *Layered-to-spinel phase transition in Li_xMnO₂*. *Electrochemical and Solid-State Letters*, 2001. **4**(6): p. A78.